Theory and Applications of the Lattice Boltzmann Method

Alexander Wagner
Christ Church
Theoretical Physics

University of Oxford

Thesis submitted for the degree of Doctor of Philosophy
in the University of Oxford

Michelmas Term, 1997

Contents

-0.8cm

Acknowledgements

It is a pleasure to thank my supervisor, Julia Yeomans, for suggesting this exciting field of research for my D.Phil subject. I am also very grateful for her help and support in preparing two publications [63] and [64].

It was with great pleasure that I accepted the invitations of Professor Dominique d'Humiéres to visite him in Paris three times and I enjoyed the stimulating discussions with him. I am also greatfull to Professor Bruce Boghosian whom I visited after the Lattice Boltzmann conference he hosted in Boston in the Summer of 96.

I would especially like to remember the support from my office mates who have been very helpful during the last three years. Roderich helped me to keep up my German, and knows everything about birds (and went to regular expeditions to the local dealer to provide us with stuff); Jean-Sébastien taught us many words that will help us to find our way round Québec (also the bz master of the office); Andrew and Christian involved us in the famous rocket-building project which triumphed with the development of the revolutionary "Prophet" model.

Thanks also to the Christ Church crowd, Andrew (a different one), who provides us with British style; James, who baffles us again and again with outrageously personal comments; Jane, now at Hampton Court; Richard, who surprised me with views that gave the word "conservative" a new meaning; Tom, the fear-

less lawyer and ex-compatriate; and my love, Heather, who helped me to remain (somewhat) sane when things got difficult.

I especially want to thank everyone who has taken the time to read all or parts of this thesis. Thanks to Julia for reading the whole thesis and improving my style of writing; Ditmar, who kindly helped me to derive the pressure tensor; Jean-Sébastien, who stood by me in moments of algebraic need; Colin, who was the only one to understand my H-theorem; Roderich, who made me improve my introduction; and last, but not least, Heather Ummel who proof-read large parts of this thesis. Everything that is wrong, of course, I did all by myself.

Chapter 1

Introduction

The aim of this thesis is to study problems in multi-phase flow and phase separation of binary fluids using a lattice Boltzmann approach.

For a long time the study of multi-phase flow has attracted much attention. Starting from early experiments [62] of drop break-up under shear flow, aimed at an understanding of the processes leading to emulsification, there has been a constant interest in this fascinating and complicated field. With the rise of computational fluid dynamics (CFD) ways to simulate two-phase flow were developed [45]. The difficulty of combining the flow of bulk fluids and the deformation of an interface, however, led to complicated numerical schemes that rely on tracking a moving mesh through a grid on which the fluid-flow equations are simulated by a finite difference-method.

Interfaces appear in a much more natural way as self-organized structures in models that were introduced in the study of phase transitions. The interfaces between different phases occur as a natural consequence of the minimization of a free energy. These systems, including the well-known Ising model, do not include hydrodynamics. They can be studied numerically using Monte Carlo simulations. These simulations lead to a proper equilibrium state, but the Monte Carlo method generates an artificial dynamics which cannot be interpreted as the real time evolution of the system.

The dynamics of such systems can be described by Thermodynamic mean field theories like the Ginzburg-Landau free energy approach. It can be used to define order parameter diffusion equations which give the time evolution of a phase ordering process. These models have found many applications in the study of critical phenomena [18].

Hydrodynamic systems can be studied by the lattice-gas method suggested in the seminal paper by Frisch, Hasslacher and Pomeau [13]. Subsequently, phase-separating lattice-gas automata have been developed [50] for immiscible fluids. In this approach, however, the introduction of phase separation is purely empirical.

As an alternative to the lattice-gas approach the lattice Boltzmann method was developed by statistically averaging the dynamics by analogy with the derivation of the Boltzmann equation in kinetic theory[36]. Early lattice Boltzmann methods suffered from the exclusion principle (i.e., there can be at most one particle at a given site), leading to an anomalous pre-factor in the Navier Stokes equation that breaks Galilean invariance [14]. Also, in both lattice Boltzmann and lattice-gas models, the viscosity is determined by the choice of collision rules for the lattice gas. This constraint was removed in the linearized lattice Boltzmann model first introduced by Higuera and co-workers [24, 25, 26], where it was observed that the collision operator can be linearized around a local equilibrium, and need not correspond to the detailed choice of collision rules of the lattice gas automata, provided it conserves mass and momentum. A further simplification was introduced by Qian, d'Humières and Lallemand [44] who proposed using the Bhatnagar-Gross-Krook (BGK) approximation for the collision term in the lattice Boltzmann method. This approximation writes the collision operator as a function of the difference between the value of the distribution function and the equilibrium distribution function. A first model for miscible binary flow using the BGK approach was proposed by Flekkøy [12].

Since then the subject has grown in many directions. A pedagogical introduction is given in the book by Rothman [52]. A recent review article by Chen and Doolen [7] describes new developments of the lattice Boltzmann method.

Swift, *et al.* [57, 58] combined the BGK lattice Boltzmann method for an ideal gas with the thermodynamic theory for a non-ideal gas, giving a thermodynamically consistent scheme that includes hydrodynamics. Since all the thermodynamic quantities entering the scheme are derived from a free energy, the method is often referred to as the free energy approach to lattice Boltzmann simulations. We use this terminology throughout the thesis.

The original scheme was introduced for a one-component Van der Waals gas [57]. Orlandini *et al.* [41] extended this scheme for binary fluids. We will review the free energy lattice Boltzmann scheme for binary mixtures in the next chapter.

In this thesis we use the free energy lattice Boltzmann scheme to study the physics of two-dimensional binary fluids. One problem that has received a lot of attention recently is the scaling behaviour of the domain coarsening of two-dimensional binary mixtures that undergo spinodal decomposition [35, 42, 67]. In the study of critical phenomena it has been discovered that many different systems have similar properties. Hohenberg and Halperin [27] distinguished a number of different universality classes, including a universality class for systems with conserved order parameter (model B) and systems that have and additional hydrodynamic degree of freedom (model H). It was suggested that the dynamics of phase ordering would be a scale invariant process that are universal for each class. But we find, in contradiction to all previous publications [35, 42], that the popular scaling hypothesis for spinodal decomposition of binary mixtures with hydrodynamics does not hold for two-dimensional systems. These results are discussed in Chapters 3 and 4.

In Chapter 5 we show for the first time how Lees-Edwards' boundary conditions [33] for shear flow can be implemented for lattice Boltzmann methods. The introduction of these boundary conditions requires major changes in the definition of the algorithm. We also introduce new measures for the orientation and its defining two orthogonal length scales for the decomposition patterns in a sheared system. We point out the differences between sheared spinodal decomposition in systems with and without internal hydrodynamics. We also describe and explain an instability of the striped patterns which often form in sheared systems undergoing spinodal decomposition.

It is well known that binary mixtures can be homogenized if a strong shear is applied. In Chapter 6 we describe the fate of a single drop in shear flow and show that both break-up and dissolving can be simulated with the free energy lattice Boltzmann method for binary mixtures. We describe a new mechanism for the dissolving of drops that we call tip-streaming. A similar phenomenon has been observed experimentally [56, and references therein] but it was interpreted as a surfactant-induced phenomenon. Here we provide the first evidence for tip-streaming in a two-component system.

The last chapter addresses some of the theoretical foundations of the lattice Boltzmann method. Ever since the lattice Boltzmann method was developed there has been speculation about the existence of an H-theorem analogous to that for the Boltzmann equation. The proof of the H-theorem for the Boltzmann equation, however, relies on detailed balance, which is absent in the lattice Boltzmann method. We have been able to prove under which circumstances a BGK lattice Boltzmann method does obey an H-Theorem and show that conventional lattice Boltzmann approaches do not obey these conditions.

Chapter 2

The free energy approach for the lattice Boltzmann method

The free energy approach for the Lattice Boltzmann method was introduced in 1995 by Swift, *et al.* [57, 58] for non-ideal one component systems and extended for binary mixtures by Orlandini, *et al.* [41] in the same year. We review the justification of the method described in these papers and add some new insights to the results presented there.

2.1 Bhatnagar-Gross-Krook lattice Boltzmann

The starting point for lattice Boltzmann simulations is the evolution equation, discrete in space and time, for a set of distribution functions f_i associated with a velocity vector $\mathbf{v}_i$. For the sake of simplicity we consider a single relaxation time, the so-called BGK approximation [2, 44]. The evolution equation for the $\{f_i\}$ is

$$f_i(\mathbf{x}+\mathbf{v}_i\Delta t, t+\Delta t) - f_i(\mathbf{x}, t) = \frac{\Delta t}{\tau_1}(f_i^0 - f_i), \tag{2.1}$$

where $\mathbf{x}$ is a lattice point, Δt is the time step, and $\mathbf{v_i}\Delta t$ is normally constrained to be a lattice vector. The single relaxation time is τ_1 and f_i^0 is the equilibrium distribution. For a two-component system a second, equivalent equation is also needed:

$$g_i(\mathbf{x}+\mathbf{v}_i\Delta t, t+\Delta t) - g_i(\mathbf{x}, t) = \frac{\Delta t}{\tau_2}(g_i^0 - g_i). \tag{2.2}$$

Physical quantities are defined as moments of the distribution functions. For our isothermal model for flow of a binary mixture of components A and B we choose

$$\begin{aligned} \sum_i f_i &= n, & (2.3)\\ \sum_i f_i \mathbf{v}_i &= n\mathbf{u}, & (2.4)\\ \sum_i g_i &= \varphi, & (2.5) \end{aligned}$$

where n is the total density field, $\mathbf{u}$ is the velocity field and φ is the field corresponding to the difference in the density of A and B components. The physics inherent in the simulation depends on the choice of the equilibrium distributions $\{f_i^0\}$ and $\{g_i^0\}$. Usually the equilibrium distributions at a lattice point will depend through the local macroscopic quantities n,$\mathbf{u}$ and φ and their derivatives in a non linear way on the f_i and g_i at this lattice point and its neighbours. Therefore equations (2.1) and (2.2) are highly non-linear.

We want to impose mass conservation for both components and momentum conservation for the bulk. This is equivalent to the following constraints on the equilibrium distributions

$$\sum_i (f_i^0 - f_i) = 0 \quad \Rightarrow \quad \sum_i f_i^0 = n, \tag{2.6}$$

$$\sum_i (g_i^0 - g_i) = 0 \quad \Rightarrow \quad \sum_i g_i^0 = \varphi, \tag{2.7}$$

$$\sum_i (f_i^0 - f_i)\mathbf{v}_i = 0 \quad \Rightarrow \quad \sum_i f_i^0 \mathbf{v}_i = n\mathbf{u}. \tag{2.8}$$

The Navier-Stokes equations usually used for examining fluid flow are an approximation to second-order in the derivatives [31]. Higher order approximations (e.g., the Burnett equations) do not obviously add to the description. The continuous partial differential equations that govern the evolution of the lattice Boltzmann fluid are obtained by a Taylor expansion of the evolution equations. Guided by the example of the Navier-Stokes equation we will perform this expansion to second order in the derivatives.

Assuming that a continuum version of the fields $f_i(\mathbf{x})$ and $g_i(\mathbf{x})$ can be expressed as a Taylor series we expand equation (2.1) as

$$\sum_{k=1}^{\infty} \frac{(\Delta t)^k}{k!} (\partial_t + v_{i\alpha}\partial_\alpha)^k f_i = \frac{\Delta t}{\tau_1}(f_i^0 - f_i) \tag{2.9}$$

where Greek indices are spatial coordinates and the summation convention over repeated Greek indices is implied. Retaining only terms up to second order in the derivatives gives

$$(\Delta t)(\partial_t + v_{i\alpha}\partial_\alpha) f_i + \frac{(\Delta t)^2}{2}(\partial_t + v_{i\alpha}\partial_\alpha)^2 f_i + O(\partial^3) = \frac{\Delta t}{\tau_1}(f_i^0 - f_i). \tag{2.10}$$

We want to express this equation in terms of the equilibrium distribution f_i^0. Since we are only interested in terms up to second order in the derivatives we need to expand f_i to first order in the derivatives of the equilibrium distribution. Using equation (2.10) to express f_i in terms of f_i^0 and its derivatives and iterating once gives

$$f_i = f_i^0 - \tau_1(\partial_t + v_{i\alpha}\partial_\alpha)f_i^0 + O(\partial^2). \tag{2.11}$$

Substituting this result into equation (2.10) gives a second order differential equation for the equilibrium distribution:

$$\frac{1}{\tau}(f_i^0 - f_i) = (\partial_t + v_{i\alpha}\partial_\alpha)f_i^0 - \omega_1(\partial_t + v_{i\alpha}\partial_\alpha)^2 f_i^0 + O(\partial^3) \tag{2.12}$$

and equivalently for the g_i

$$\frac{1}{\tau}(g_i^0 - g_i) = (\partial_t + v_{i\alpha}\partial_\alpha)g_i^0 - \omega_2(\partial_t + v_{i\alpha}\partial_\alpha)^2 g_i^0 + O(\partial^3), \tag{2.13}$$

where

$$\omega_{1,2} = \tau_{1,2} - \frac{\Delta t}{2}. \tag{2.14}$$

To obtain the partial differential equations governing the evolution of the macroscopic quantities we sum over the conserved moments defined in equations (2.6), (2.7) and (2.8). We again neglect terms with higher than second order derivatives. First summing equation (2.12) and using equation (2.6) for conservation of the total mass we obtain

$$0 = \partial_t n + \partial_\alpha n u_\alpha - \omega_1\left(\partial_t(\partial_t n + \partial_\alpha n u_\alpha) + \partial_\beta(\partial_t n u_\beta + \partial_\alpha \sum_i f_i^0 v_{i\alpha} v_{i\beta})\right) + O(\partial^3). \tag{2.15}$$

We see that the term $\partial_t n + \partial_\alpha n u_\alpha$ is of second order in the derivatives. Its derivatives can therefore be ignored and the equation simplifies to

$$0 = \partial_t n + \partial_\alpha n u_\alpha - \omega_1 \partial_\beta(\partial_t n u_\beta + \partial_\alpha \sum_i f_i^0 v_{i\alpha} v_{i\beta}) + O(\partial^3). \tag{2.16}$$

Now summing equation (2.12) times an extra factor of $\mathbf{v}_i$ and using the equation of momentum conservation (2.8) we obtain, using similar arguments,

$$0 = \partial_t n u_\alpha + \partial_\beta \sum_i f_i^0 v_{i\alpha} v_{i\beta} - \omega_1 \partial_\gamma (\partial_t \sum_i f_i^0 v_{i\alpha} v_{i\gamma} + \partial_\beta \sum_i f_i^0 v_{i\alpha} v_{i\beta} v_{i\gamma}) + O(\partial^3). \tag{2.17}$$

Equation (2.17) shows that the second term in equation (2.16) is of third order in the derivatives. Hence, equation (2.16) gives the continuity equation to second order in the derivatives

$$0 = \partial_t n + \partial_\alpha n u_\alpha + O(\partial^3). \tag{2.18}$$

Summing over equation (2.13) and using (2.7) we obtain similarly

$$0 = \partial_t \varphi + \partial_\alpha \sum_i g_i^0 v_{i\alpha} - \omega_2 \partial_\beta (\partial_t \sum_i g_i v_{i\beta} + \partial_\alpha \sum_i g_i^0 v_{i\alpha} v_{i\beta}) + O(\partial^3). \tag{2.19}$$

These are general equations for any two-component lattice Boltzmann scheme with mass and momentum conservation. In order to proceed further we need to define higher-order moments of the equilibrium densities. The choice within the free energy lattice Boltzmann scheme for these moments is

$$\sum_i f_i^0 v_{i\alpha} v_{i\beta} = P_{\alpha\beta} + n u_\alpha u_\beta, \tag{2.20}$$

$$\sum_i g_i^0 v_{i\alpha} = \varphi u_\alpha, \tag{2.21}$$

$$\sum_i g_i^0 v_{i\alpha} v_{i\beta} = \Gamma \mu \delta_{\alpha\beta} + \varphi u_\alpha u_\beta, \tag{2.22}$$

where $P_{\alpha\beta}$ is the pressure tensor, Γ a mobility parameter, μ is the chemical potential for the density difference and δ is the Kronecker delta. The physical motivation of these constraints arises from a consideration of the thermodynamics of a binary mixture and is discussed in more detail in the next section.

Using (2.20) to (2.22) we can now evaluate the macroscopic equations further. For equation (2.19)

$$\begin{aligned} 0 &= \partial_t\varphi + \partial_\alpha(\varphi u_\alpha) - \omega_2\partial_\beta(\partial_t(\varphi u_\beta) + \partial_\alpha(\Gamma\mu\delta_{\alpha\beta} + \varphi u_\alpha u_\beta)) + O(\partial^3) \\ &= \partial_t\varphi + \partial_\alpha(\varphi u_\alpha) - \omega_2(\Gamma\nabla^2\mu + \partial_\beta((\partial_t\varphi + \partial_\alpha(\varphi u_\alpha))u_\beta) \\ &\quad +\varphi(\partial_t u_\alpha + u_\alpha\partial_\alpha u_\beta)) + O(\partial^3). \end{aligned} \tag{2.23}$$

The term $\partial_t\varphi + \partial_\alpha(\varphi u_\alpha)$ is second order in the derivatives and can be dropped where its derivative is taken. The term $\partial_t u_\alpha + u_\alpha\partial_\alpha u_\beta$ can be rewritten with the help of equation (2.17):

$$\begin{aligned} O(\partial^2) &= \partial_t(nu_\alpha) + \partial_\beta\sum_i f_i^0 v_{i\alpha}v_{i\beta} \\ &= (\partial_t n)u_\alpha + n\partial_t u_\alpha + \partial_\beta P_{\alpha\beta} + \partial_\beta(nu_\beta)u_\alpha + nu_\beta\partial_\beta u_\alpha. \end{aligned} \tag{2.24}$$

Using the continuity equation (2.18) gives

$$\partial_t u_\alpha + u_\beta\partial_\beta u_\alpha = -\frac{1}{n}\partial_\beta P_{\alpha\beta} + O(\partial^2). \tag{2.25}$$

Substituting this result into (2.23) we arrive at the convection diffusion equation governing the evolution of the density difference

$$\partial_t\varphi + \partial_\alpha(\varphi u_\alpha) = \omega_2\left(\Gamma\nabla^2\mu - \partial_\beta\left(\frac{\varphi}{n}\partial_\alpha P_{\alpha\beta}\right)\right). \tag{2.26}$$

This is a drift-diffusion equation with a diffusion constant $\Gamma\omega_2$. There is an additional term in the derivatives of the pressure tensor. A similar[1] term has been used in a phenomenological model to describe flow-induced diffusion [10].

---

[1] The term used was $\partial_\beta\xi\partial_\alpha P_{\alpha\beta}$. In this approach ξ was treated as a constant [10].

The momentum conservation equation (2.17) can be written as

$$0 = \partial_t n u_\alpha + \partial_\beta (P_{\alpha\beta} + n u_\alpha u_\beta) - \omega_1 \partial_\gamma (\partial_t \sum_i f_i^0 v_{i\alpha} v_{i\gamma} + \partial_\beta \sum_i f_i^0 v_{i\alpha} v_{i\beta} v_{i\gamma}) + O(\partial^3). \tag{2.27}$$

Using the same analysis that led to equation (2.25) gives

$$n\partial_t u_\alpha + n u_\beta \partial_\beta u_\alpha = -\partial_\beta P_{\alpha\beta} + \omega_1 \partial_\gamma (\partial_t \sum_i f_i^0 v_{i\alpha} v_{i\gamma} + \partial_\beta \sum_i f_i^0 v_{i\alpha} v_{i\beta} v_{i\gamma}) + O(\partial^3). \tag{2.28}$$

The three-velocity moment cannot be evaluated without further knowledge of the equilibrium distribution. In order to derive the compressible Navier Stokes equation we would like to impose

$$\sum_i f_i^0 v_{i\alpha} v_{i\beta} v_{i\gamma} = P_{\alpha\beta} u_\gamma + P_{\alpha\gamma} u_\beta + P_{\beta\gamma} u_\alpha + n u_\alpha u_\beta u_\gamma, \tag{2.29}$$

but this is not possible for a nine-velocity model that we are using. The recovery of the compressible Navier-Stokes equation which is achieved by (2.29) is described in Appendix A. For the nine-velocity model (see Figure 2.4) the best possible choice is

$$\sum_i f_i^0 v_{i\alpha} v_{i\beta} v_{i\gamma} = \frac{n}{3}(u_\alpha \delta_{\beta\gamma} + u_\beta \delta_{\alpha\gamma} + u_\gamma \delta_{\alpha\beta}). \tag{2.30}$$

We will now show how the viscosity terms can be calculated in analogy to the derivation of terms for the fully compressible Navier-Stokes equation presented in Appendix A. We present this calculation in detail because it differs from the calculations in [58]. Terms that vanish in the calculation for the compressible case are underlined and contracted to give the correction terms. With equation

(2.30) we get for the viscosity terms

$$\begin{aligned}
& \partial_t \sum_i f_i^0 v_{i\alpha} v_{i\beta} + \partial_\gamma \sum f_i^0 v_{i\alpha} v_{i\beta} v_{i\gamma} \\
= \; & \partial_t (P_{\alpha\beta} + n u_\alpha u_\beta) + \partial_\gamma (\frac{n}{3}\delta_{\alpha\beta} u_\gamma + \frac{n}{3}\delta_{\alpha\gamma} u_\beta + \frac{n}{3}\delta_{\beta\gamma} u_\alpha) + O(\partial^2) \\
= \; & \partial_n P_{\alpha\beta} \partial_t n + \partial_t (n u_\alpha) u_\beta + n u_\alpha \partial_t u_\beta \\
& + \left(\partial_\gamma \frac{n}{3}\delta_{\alpha\beta}\right) u_\gamma + \frac{n}{3}\delta_{\alpha\beta}\partial_\gamma u_\gamma + \left(\partial_\gamma \frac{n}{3}\delta_{\alpha\gamma}\right) u_\beta + \frac{n}{3}\delta_{\alpha\gamma}\partial_\gamma u_\beta + \left(\partial_\gamma \frac{n}{3}\delta_{\beta\gamma}\right) u_\alpha + \frac{n}{3}\delta_{\beta\gamma}\partial_\gamma u_\alpha \\
& + O(\partial^2) \\
= \; & -\partial_n P_{\alpha\beta} \partial_\gamma (n u_\gamma) - \partial_\gamma (P_{\alpha\gamma} + n u_\alpha u_\gamma) u_\beta \underline{- n u_\alpha \frac{1}{n} \partial_\gamma P_{\beta\gamma}} - n u_\alpha u_\beta \partial_\gamma u_\gamma \\
& + \left(\partial_n \frac{n}{3}\delta_{\alpha\beta}\right) (\partial_\gamma n) u_\gamma + \frac{n}{3}\delta_{\alpha\beta}\partial_\gamma u_\gamma + \left(\partial_\gamma \frac{n}{3}\delta_{\alpha\gamma}\right) u_\beta + \frac{n}{3}\delta_{\alpha\gamma}\partial_\gamma u_\beta \underline{+ \left(\partial_\gamma \frac{n}{3}\delta_{\beta\gamma}\right) u_\alpha} \\
& + \frac{n}{3}\delta_{\beta\gamma}\partial_\gamma u_\alpha + O(\partial^2) \\
= \; & -\partial_n P_{\alpha\beta} \partial_\gamma (n u_\gamma) \underline{- \partial_\gamma P_{\alpha\gamma} u_\beta} - \underline{\partial_\gamma (n u_\alpha u_\gamma) u_\beta} - \underline{n u_\alpha u_\beta \partial_\gamma u_\gamma} \\
& + \left(\partial_n \frac{n}{3}\delta_{\alpha\beta}\right) \partial_\gamma u_\gamma + \frac{n}{3}\delta_{\alpha\beta}\partial_\gamma u_\gamma \underline{+ \left(\partial_\gamma \frac{n}{3}\delta_{\alpha\gamma}\right) u_\beta} + \frac{n}{3}\delta_{\alpha\gamma}\partial_\gamma u_\beta + \\
& \frac{n}{3}\delta_{\beta\gamma}\partial_\gamma u_\alpha + \partial_\gamma \left(\frac{n}{3}\delta_{\beta\gamma} - P_{\beta\gamma}\right) u_\alpha + O(\partial^2) \\
= \; & \underline{-\partial_n P_{\alpha\beta} (\partial_\gamma n) u_\gamma} - \partial_n P_{\alpha\beta} n \partial_\gamma u_\gamma + \underline{\partial_n \frac{n}{3}\delta_{\alpha\beta} (\partial_\gamma n) u_\gamma} \\
& + \frac{n}{3}\delta_{\alpha\beta}\partial_\gamma u_\gamma + \frac{n}{3}\delta_{\alpha\gamma}\partial_\gamma u_\beta + \frac{n}{3}\delta_{\beta\gamma}\partial_\gamma u_\alpha + \partial_\gamma \left(\frac{n}{3}\delta_{\beta\gamma} - P_{\beta\gamma}\right) u_\alpha + \partial_\gamma \left(\frac{n}{3}\delta_{\alpha\gamma} - P_{\alpha\gamma}\right) u_\beta \\
& - \partial_\gamma (n u_\alpha u_\beta u_\gamma) + O(\partial^2) \\
= \; & \left(\frac{n}{3}\delta_{\alpha\beta} - n \partial_n P_{\alpha\beta}\right) \partial_\gamma u_\gamma + \frac{n}{3}\delta_{\alpha\gamma}\partial_\gamma u_\beta + \frac{n}{3}\delta_{\beta\gamma}\partial_\gamma u_\alpha \\
& + \partial_\gamma \left(\frac{n}{3}\delta_{\beta\gamma} - P_{\beta\gamma}\right) u_\alpha + \partial_\gamma \left(\frac{n}{3}\delta_{\alpha\gamma} - P_{\alpha\gamma}\right) u_\beta + \partial_n \left(\frac{n}{3}\delta_{\alpha\beta} - P_{\alpha\beta}\right) u_\gamma \partial_\gamma n \\
& - \partial_\gamma (n u_\alpha u_\beta u_\gamma) + O(\partial^2).
\end{aligned} \tag{2.31}$$

We see that, except for the $\partial_\gamma (n u_\alpha u_\beta u \gamma)$ term, we recover the compressible Navier

Stokes equations if we choose $P_{\alpha\beta} = \frac{n}{3}\delta_{\alpha\beta}$ (i.e., if the equation of state for the bulk fluid is that for an ideal gas at temperature $T = 1/3$). In the incompressible limit with constant density and pressure we recover the incompressible Navier Stokes equations for a non-ideal system

$$n\partial_t u_\alpha + n u_\beta \partial_\beta u_\alpha = -\partial_\beta P_{\alpha\beta} + \frac{n\omega_1 D}{3}\partial_\beta \left(\frac{\delta_{\alpha\beta} - 3\partial_n P_{\alpha\beta}}{D} \partial_\gamma u_\gamma + \partial_\alpha u_\beta + \partial_\beta u_\alpha \right) + O(\partial^3) \tag{2.32}$$

where the viscosity is given by $\nu = n\omega_1 D/3$ where D is the number of spatial dimensions.

This is, so far, a general framework for the two-component free energy lattice Boltzmann method. The properties of the two components and the miscibility are determined by two quantities: the pressure tensor $P_{\alpha\beta}$ and the chemical potential μ. In the next section we describe how these two quantities can be derived from a free energy functional.

2.2 Thermodynamics of a binary mixture

The free energy approach to lattice Boltzmann models simulates non-equilibrium systems and relies on the assumption that the system can still locally be described by equilibrium thermodynamic fields. The thermodynamic fields entering the simulation are the pressure tensor and the chemical potential. They can be derived from the free energy of a system. This makes the method a rather general tool to study the dynamics of systems with a given free energy. The approach has been used for a Van der Waals gas [57, 58] and a binary mixture [41]. The binary mixture model has been extended to include negative surface tension and, hence, simulate lamellar phases. It would be interesting to consider other systems like polymers by using a Flory-Huggins free energy.

We consider the free energy for a simple binary fluid comprising two components A and B, where each of the components is an ideal gas. A–A and B–B interactions are zero, but there is an A–B repulsion $\lambda n_A n_B$ where n_A and n_B are the number densities of A- and B-particles, respectively. This system can be described by the Landau free energy functional

$$\Psi = \int d\mathbf{r}(\psi(\varphi, n, T) + \frac{\kappa}{2}(\nabla\varphi)^2) \tag{2.33}$$

where T is the temperature, $n = n_A + n_B$, $\varphi = n_A - n_B$ (as defined in the previous section) and κ is a measure for the interface free energy (surface tension). The free energy density of the homogeneous system is [47]

$$\begin{aligned} \psi(\varphi, n, T) &= \frac{\lambda n}{4}\left(1 - \frac{\varphi^2}{n^2}\right) - Tn \\ &+ \frac{T}{2}(n+\varphi)\ln\left(\frac{n+\varphi}{2}\right) + \frac{T}{2}(n-\varphi)\ln\left(\frac{n-\varphi}{2}\right). \end{aligned} \tag{2.34}$$

From the free energy (2.33) we derive the local chemical potential μ as the functional derivative of the total free energy Ψ with respect to the concentration difference field $\varphi(\mathbf{x})$

$$\begin{aligned} \mu(\mathbf{x}) &= \frac{\delta\Psi}{\delta\varphi(\mathbf{x})} \\ &= -\frac{\lambda}{2}\frac{\varphi}{n} + \frac{T}{2}\ln\left(\frac{n+\varphi}{n-\varphi}\right) - \kappa\nabla^2\varphi. \end{aligned} \tag{2.35}$$

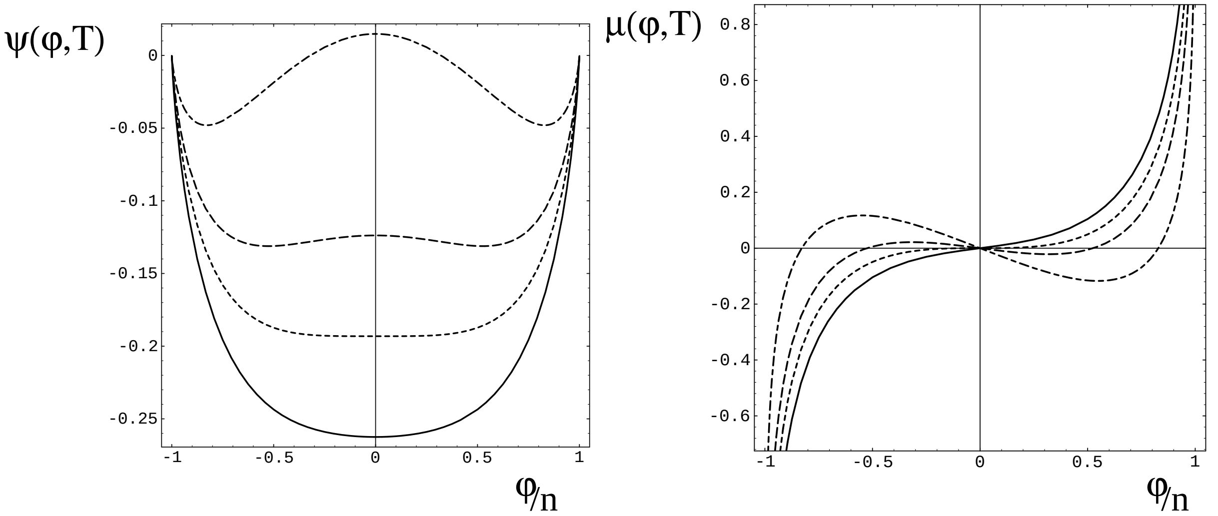

Figure 2.1: Free energy $\psi(\varphi, T)$ and chemical potential $\mu(\varphi, T)$ for temperatures $T = 1.1T_c$ (————), $T = T_c$ (– – – – – –), $T = 0.9T_c$ (— — — —), and $T = 0.7T_c$ (— – — – —). Above the critical temperature T_c the free energy ψ has a local maximum for $\varphi = 0$ and two minima which are the equilibrium values for the order parameter φ.

The derivation of the pressure tensor is slightly more involved and is discussed in Appendix B. We obtain

$$\begin{aligned} P_{\alpha\beta} &= (n\partial_n\psi + \varphi\partial_\varphi\psi - \psi)\delta_{\alpha\beta} + \kappa(\partial_\alpha\varphi\partial_\beta\varphi - \frac{1}{2}\partial_\gamma\varphi\partial_\gamma\varphi\delta_{\alpha\beta} - \varphi\partial_\gamma\partial_\gamma\varphi) \\ &= (nT + \varphi\mu^0(x))\delta_{\alpha\beta} + \kappa(\partial_\alpha\varphi\partial_\beta\varphi - \frac{1}{2}\partial_\gamma\varphi\partial_\gamma\varphi\delta_{\alpha\beta} - \varphi\partial_\gamma\partial_\gamma\varphi) \\ &= (nT + \varphi\mu(x))\delta_{\alpha\beta} + \kappa(\partial_\alpha\varphi\partial_\beta\varphi - \frac{1}{2}\partial_\gamma\varphi\partial_\gamma\varphi\delta_{\alpha\beta}) \qquad (2.36) \end{aligned}$$

where the first term is the ideal gas pressure, the second term is the osmotic pressure with $\mu^0 = \partial_\phi\psi$ and the third term is related to the surface tension as discussed below. The osmotic pressure was omitted in the original definition of the model [41, 58].

The bulk free energy of equation (2.34) is shown in Figure 2.1. For different temperatures the free energy has a transition from a form with only one minimum at $\varphi = 0$ to a form with two minima. At the transition temperature, which is the critical temperature T_c for this system, the second derivative of the free energy vanishes. For the second derivative

$$0 = \partial_\varphi^2 \psi|_{\varphi=0, T=T_c} = -\frac{\lambda}{2n} + \left.\frac{nT}{(n-\varphi)(n+\varphi)}\right|_{\varphi=0, T=T_c}. \tag{2.37}$$

Hence, the critical temperature is given by

$$T_c = \frac{\lambda}{2}. \tag{2.38}$$

Let us consider the stability of a homogeneous mixture at different temperatures (initially neglecting the derivative terms in the free energy). Figure 2.1b shows the bulk chemical potential μ^0 for different temperatures. For $T > T_c$ the chemical potential is a monotonic function. The evolution of the density difference is given by the drift diffusion equation 2.26. Without flow we have

$$\partial_t \varphi = \Gamma \omega_2 \partial_\alpha \partial_\alpha, \mu(\varphi) \tag{2.39}$$

which is a diffusion equation that homogenizes any fluctuations in an initial density configuration. To examine the stability of a homogeneous mixture we can linearize this equation around the homogeneous density difference $\varphi = \hat{\varphi}$

$$\partial_t \varphi = D(\hat{\varphi}) \partial_\alpha \partial_\alpha \varphi \tag{2.40}$$

with $D(\hat{\varphi}) = \Gamma \omega_2 \partial_\varphi \mu(\hat{\varphi})$. But for $T < T_c$ a region around $\hat{\varphi} = 0$ exists where $D(\hat{\varphi}) < 0$ inverts the diffusive process and fluctuations grow, leading to phase ordering.

The phase ordering process separates the phases until a stationary state is reached where the order parameter in the domains takes on its two equilibrium values φ_1 and φ_2. This equilibrium value is determined by two conditions. First, because of the symmetry of the free energy with respect to $\varphi \to -\varphi$ we have $\varphi_1 = -\varphi_2$. Also, the chemical potential has to be constant

$$\mu(\varphi_1) = \mu(\varphi_2). \tag{2.41}$$

These conditions can only be fulfilled for $\mu = 0$. The equilibrium values for the order parameter at coexistence are therefore given by the negative and positive solutions of the equation

$$0 = \mu(\varphi, T). \tag{2.42}$$

The coexistence curve that plots the coexistence order parameter against the temperature is shown in Figure 2.2.

The system is unstable against all fluctuations in the region where $D(\varphi)$ is negative. Outside this region, but inside the coexistence curve, a homogeneous system is meta-stable and a finite fluctuation is needed to nucleate a phase ordering domain. The border of this region is given by $\partial_\varphi \mu(\varphi) = 0$. It is called the spinodal line and is indicated by a dashed line in Figure 2.2.

The phase ordering process by which a homogeneous system phase separates inside the spinodal line is called spinodal decomposition. The properties of this process depend strongly on the average value of the order parameter φ. Some examples of spinodal decomposition for $T = 0.9T_c$ for different order parameter are shown in Figure 2.2. We see that there is an important difference between

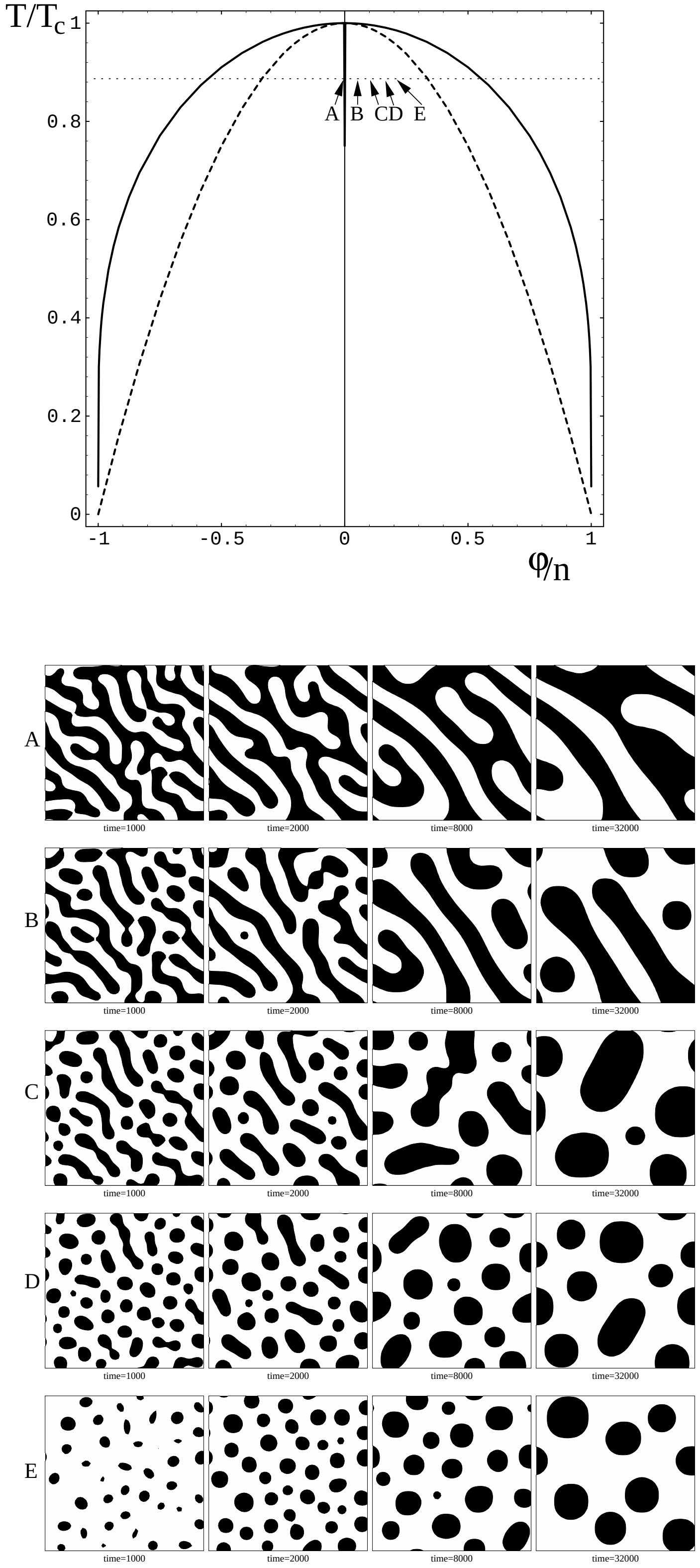

Figure 2.2: The top figure is the coexistence curve for the free energy of equation 2.34 for binary system. The dashed line indicates the spinodal line. Inside the area enclosed by the spinodal line a homogeneous system is unstable. Outside this region a finite perturbation is needed to seed a nucleation. The dotted line is at the temperature at which all simulations in this thesis were performed. The arrows indicate the positions in the phase diagram at which the spinodal decompositions in the bottom figure were performed. (See text for more detail.)

critical $\varphi_{av} = 0$ and off-critical $\varphi_{av} \neq 0$ spinodal decomposition. For off-critical spinodal decomposition a phase of droplets of the minority phase forms. For the critical spinodal decomposition both phases are equivalent[2] and neither will preferably form a droplet phase. Critical spinodal decomposition is discussed in detail in Chapter 3 where we also discuss the effects of the hydrodynamic degree of freedom.

Up to now we have neglected the surface free energy term. The surface free energy term prevents sharp interfaces and introduces surface tension. The theoretical interface profile is determined by the condition that the chemical potential is zero

$$0 = \mu(\mathbf{x}) = -\frac{\lambda}{2n}\varphi + \frac{T}{2}\ln\left(\frac{n+\varphi}{n-\varphi}\right) - \frac{\kappa}{2}\partial_\alpha\partial_\alpha\varphi. \tag{2.43}$$

In Figure 2.3 a) the numerical solution of this expression is compared to the simulation results for two different values of the surface free energy parameter kappa.

The surface tension for an interface orthogonal to the z-direction is [53, 4]

$$\sigma = \kappa\int_{-\infty}^{\infty}\left(\frac{\partial\varphi}{\partial z}\right)^2 dz. \tag{2.44}$$

We can rewrite equation (2.43) as

$$0 = -2\frac{T_c}{T}\bar{\varphi} + \ln\left(\frac{1+\bar{\varphi}}{1-\bar{\varphi}}\right) - \partial_{\alpha'}\partial_{\alpha'}\bar{\varphi} \tag{2.45}$$

---

[2] This is no longer true, if the two phases have different physical properties. Recent simulations show that if say the A-rich phase has a higher viscosity the B-rich phase will form a droplets surrounded by the higher viscosity A-rich phase.

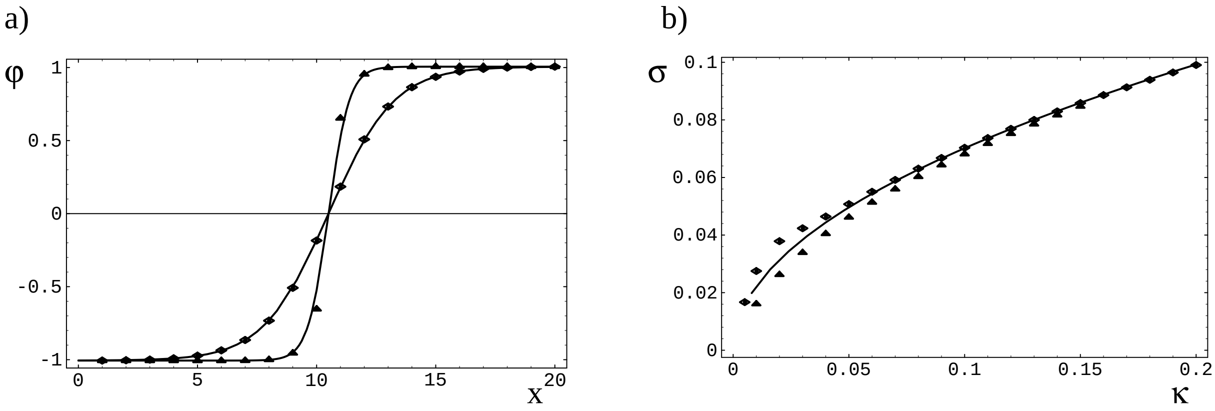

Figure 2.3: Graph a) shows the theoretical interface profile (—)and the simulation results for a flat interface for $\kappa = 0.2$ (◇) and $\kappa = 0.02$ (△). Graph b) shows the theoretical values for the surface tension (—), the value for the summation of the squares of the discrete derivatives (◇) and the value calculated from Laplace's law (△).(See text for more detail.)

where $\bar{\varphi} = \varphi/n$ and $z' = \sqrt{(\kappa n)/T}$. We then calculate

$$\sigma_0\left(\frac{\lambda}{T}\right) = \kappa \int_{-\infty}^{\infty} \left(\frac{\partial \bar{\varphi}}{\partial z'}\right)^2 dz' \tag{2.46}$$

and get for the surface tension

$$\sigma(\kappa, n, T, \lambda) = \sigma_0\left(\frac{\lambda}{T}\right)\sqrt{\frac{\kappa T}{n}}. \tag{2.47}$$

The surface tension can also be determined in simulations from Laplace's law. Laplace's law states that the surface tension is given by the radius of a drop R and the pressure difference ΔP between the inside and the outside of the drop as

$$\sigma = R\Delta P. \tag{2.48}$$

We performed simulations with a drop of radius 20 for different values of κ. The results are shown in Figure 2.3 b). We see that there is a good agreement for wide interfaces that stretch over many lattice points, but some accuracy is lost for thin interfaces.

2.3 Summary of the model

We will now collect all the ingredients for the free energy lattice Boltzmann method for a binary mixture and define an explicit scheme. The evolution equations for the two-component lattice Boltzmann scheme are

$$\begin{aligned} f_i(\mathbf{x}+\mathbf{v}_i\Delta t, t+\Delta t) - f_i(\mathbf{x},t) &= \frac{\Delta t}{\tau_1}(f_i^0 - f_i), & (2.49)\\ g_i(\mathbf{x}+\mathbf{v}_i\Delta t, t+\Delta t) - g_i(\mathbf{x},t) &= \frac{\Delta t}{\tau_2}(g_i^0 - g_i). & (2.50)\end{aligned}$$

The moments of the equilibrium distributions obey the equations

$$\begin{aligned} &\sum_i f_i^0 = n, \quad \sum_i f_i^0 \mathbf{v}_i = n\mathbf{u}, \quad \sum_i f_i^0 v_{i\alpha} v_{i\beta} = P_{\alpha\beta} + n u_\alpha u_\beta, \\ &\sum_i f_i^0 v_{i\alpha} v_{i\beta} v_{i\gamma} = \frac{n}{3}(u_\alpha \delta_{\beta\gamma} + u_\beta \delta_{\alpha\gamma} + u_\gamma \delta_{\alpha\beta}), \\ &\sum_i g_i^0 = \varphi, \quad \sum_i g_i^0 v_{i\alpha} = \varphi u_\alpha, \quad \sum_i g_i^0 v_{i\alpha} v_{i\beta} = \Gamma\mu\delta_{\alpha\beta} + \varphi u_\alpha u_\beta \qquad (2.51)\end{aligned}$$

where n is the total density, $\mathbf{u}$ is the fluid velocity, $\varphi = n_A - n_B$ is the density difference of the two components of the binary mixture and Γ is a mobility. The chemical potential μ and the thermodynamic pressure tensor $P_{\alpha\beta}$ are given by

$$\mu(\mathbf{x}) = -\frac{\lambda}{2}\frac{\varphi}{n} + \frac{T}{2}\ln\left(\frac{n+\varphi}{n-\varphi}\right) - \kappa\nabla^2\varphi, \qquad (2.52)$$

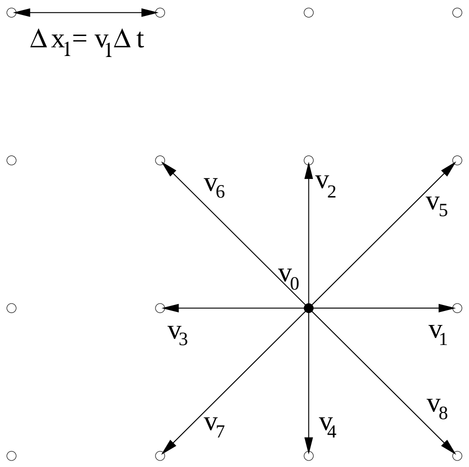

Figure 2.4: Our numbering of the velocity vectors in a nine-velocity model.

$$P_{\alpha\beta} = (nT + \varphi\mu^0(x))\delta_{\alpha\beta} + \kappa(\partial_\alpha\varphi\partial_\beta\varphi - \frac{1}{2}\partial_\gamma\varphi\partial_\gamma\varphi\delta_{\alpha\beta} - \varphi\partial_\gamma\partial_\gamma\varphi\delta_{\alpha\beta}). \quad (2.53)$$

In this thesis, as in the original model, we neglect the osmotic pressure term $\varphi\mu^0(x)$.

In the original model that satisfies these equations [41, 58] the equilibrium distributions are given as an expansion in the velocities. We use a nine-velocity model where the velocities $\mathbf{v}_{\{0,\cdots,9\}}$ are defined in Figure 2.4. For this model we define [40]

$$f_i^0 = A_\sigma + B_\sigma u_\alpha v_{i\alpha} + C_\sigma \mathbf{u}^2 + D_\sigma u_\alpha u_\beta v_{i\alpha} v_{i\beta} + G_{\sigma\,\alpha\beta} v_{i\alpha} v_{i\beta}, \quad (2.54)$$

$$f_i^0 = H_\sigma + K_\sigma u_\alpha v_{i\alpha} + J_\sigma \mathbf{u}^2 + Q_\sigma u_\alpha u_\beta v_{i\alpha} v_{i\beta}, \quad (2.55)$$

where $\sigma = \mathbf{v}_i^2 \in \{0, 1, 2\}$ is an index to distinguish the coefficients for the densities for different absolute values of the velocities.

A choice of these coefficients that ensures that the equilibrium distribution satisfies the constraints (2.53)

$$
\begin{aligned}
A_2 &= \frac{1}{8}p_0(n,\varphi,\nabla^2\varphi), \quad A_1 = 2A_2, \quad A_0 = n - 12A_2, && (2.56)\\
B_2 &= \frac{n}{12}, \quad B_1 = 4B_2, && (2.57)\\
C_2 &= -\frac{n}{16}, \quad C_1 = 2C_2, \quad C_0 = -\frac{3n}{4}, && (2.58)\\
D_2 &= \frac{n}{8}, \quad D_1 = 4D_2, && (2.59)\\
G_{2xx} &= \frac{\kappa}{16}((\partial_x\varphi)^2 - (\partial_y\varphi)^2), \quad G_{2xy} = G_{2yx} = \frac{\kappa}{8}\partial_x\varphi\partial_y\varphi, \quad G_{2yy} = -G_{2xx}, && (2.60)\\
G_{1xx} &= 4G_{2xx}, \quad G_{1xy} = G_{1yx} = 4G_{2xy}, \quad G_{1yy} = 4G_{2yy}, && (2.61)\\
H_2 &= \frac{\Gamma}{8}\mu(n,\varphi,\nabla^2\varphi), \quad H_1 = 2H_2, \quad H_0 = \varphi - 12H_2, && (2.62)\\
K_2 &= \frac{\varphi}{n}B_2, \quad K_1 = \frac{\varphi}{n}B_1, && (2.63)\\
J_2 &= \frac{\varphi}{n}C_2, \quad J_1 = \frac{\varphi}{n}C_1, \quad J_0 = \frac{\varphi}{n}C_0, && (2.64)\\
Q_2 &= \frac{\varphi}{n}D_2, \quad Q_1 = \frac{\varphi}{n}D_1. && (2.65)
\end{aligned}
$$

To implement Lees-Edwards boundary conditions for the free energy lattice Boltzmann scheme we shall introduce a different equilibrium distribution in Chapter 5.

The differential equations simulated by the lattice Boltzmann method are to second order in the derivatives and assuming incompressibility or $T = 1/3$, the continuity equation

$$0 = \partial_t n + \partial_\alpha n u_\alpha, \tag{2.66}$$

the Navier Stokes equations

$$n\partial_t u_\alpha + n u_\beta \partial_\beta u_\alpha = -\partial_\beta P_{\alpha\beta} + \frac{n\omega_1 D}{3}\left(\partial_\beta((\delta_{\alpha\beta} - 3\partial_n P_{\alpha\beta})\partial_\gamma u_\gamma + \partial_\alpha u_\beta + \partial_\beta u_\alpha\right) \tag{2.67}$$

and the drift diffusion equation for the density difference

$$\partial_t\varphi + \partial_\alpha(\varphi u_\alpha) = \omega_2\left(\Gamma\nabla^2\mu - \partial_\beta\left(\frac{\varphi}{n}\partial_\alpha P_{\alpha\beta}\right)\right), \tag{2.68}$$

where

$$\omega_{1,2} = \tau_{1,2} - \frac{\Delta t}{2}. \tag{2.69}$$

This now completely defines the numerical scheme used for the simulations in the following chapters.

This algorithm can be easily encoded into a numeric scheme. A sketch of a Lattice Boltzmann program for a two-dimensional nine velocity model in **C** is presented in Appendix C.

Chapter 3

Scaling of domain coarsening after spinodal decomposition

3.1 Introduction

The theory of phase-ordering kinetics or “domain coarsening” following a temperature quench from a homogeneous phase into a two-phase region has a history going back more than three decades to the pioneering work of Lifshitz and Slyozov [34] and Wagner [65]. Since that time, many excellent reviews have appeared, including those by Gunton *et al.* [18], Binder [3], and Bray [4]. In this work it has been established that for many different phase separating systems the domain patterns look statistically similar to those at earlier times, apart from a global change of scale. An example of this are binary mixtures without hydrodynamics and Figure 3.5 shows an example of such a scale invariant domain coarsening process. The assumption that a system obeys this scale invariance is called the "dynamic scaling hypothesis" which will be formalized below.

Among the systems for which dynamic scaling hypothesis has been made are two-dimensional binary mixtures with hydrodynamic interactions. There was some experimental [20], theoretical [4] and numerical [8, 42, 35] evidence that this was indeed the case. Previous numerical and theoretical papers have predicted different scaling regimes. For early times and high viscosities a scaling regime with $L \sim t^{\frac{1}{3}}$ has been observed [42], whereas for late times or lower viscosities most numerical work agrees on seeing a $L \sim t^{\frac{2}{3}}$ scaling law [16, 42, 35]. They use R_1[41], the similar first zero of the correlation function [35], and both R° and R_1 [16] as measures of the scaling length of the system.

All of the methods used by the authors above rely on structure functions, correlation functions or dimensional analysis, but no direct observation of real space structures. In this chapter we show that direct observation of the coarsening of the domain structure for two-dimensional binary mixtures with hydrodynamics suggests that the dynamic scaling hypothesis does not hold for this system. We develop a measure that is able to capture the perceived breakdown of scaling and give a descriptive explanation of why the coarsening mechanism is not scale invariant. We also describe a new coarsening mechanism where the effect of hydrodynamic coarsening is limited by capillary waves.

3.2 Methods for testing scaling behaviour

We commence by summarizing the ideas of dynamic scaling. Then we introduce a number of different length scales and test their scaling behaviour for two simple test cases. In a case of trivial scaling all the length scales display the scaling. In the more usual case where there are constant length scales like the interface width some of these length scales will not show scaling. In some special cases (see 3.2.2) the dependence of these length scales on the static length can be analysed and a length scale that displays the scaling law can be derived. For binary mixtures, as for most other systems, the interface width is constant during the evolution. We find that scaling does not always hold in hydrodynamic spinodal decomposition of binary mixtures in two dimensions. We explain why dynamic scaling does not exist in these systems.

The dynamic scaling hypothesis states that a phase ordering system obeys dynamic scaling if it evolves through statistically equivalent states except for a change in length scale $R(t)$. Furthermore, the growth law is often a power-law

$$R(t) \sim (t - t_0)^{\alpha} \tag{3.1}$$

where α is the growth exponent and t_0 is a zero time that does not have to coincide with the start of the simulation or experiment and can be used as a fitting parameter. In practice we demand that the simulation time interval is much larger than t_0 to ensure that fitting results are meaningful. In systems which show power-law scaling α and time-independent shape functions like Φ are universal features of the growth kinetics.

A length scale is a quantity which has the dimensions of a length and which is independent of the size of the system. In a system which obeys dynamic scaling all length scales should obey the same scaling law. Often in experimental and numerical work [42] just one length scale is measured to extract a value for the exponent α and the scaling hypothesis is assumed. More careful analysis [35] checks the scaling properties of the structure function or the correlation function. If, however, any two length scales do not obey the same growth law, the system is not strictly scaling invariant.

During the domain growth process the interface width is constant. Therefore, all measures that involve this length scale will show a different scaling than would be expected from dimensional analysis and care must be taken to appreciate this point when interpreting the data. We will see, however, that even dynamic length have a different growth law for hydrodynamic spinodal decomposition in two dimensions.

3.2.1 Definition of length scales

We will now define some widely used and some less obvious length scales and demonstrate the points made above. Perhaps the most commonly measured length scale is derived from the first moment [55, 49] of the radially averaged structure function. Length scales which give more information about the fine structure of the domains can also be derived from higher-order moments.

These are based on an analysis with Fourier transforms. But in computer simulations and in some directly observed systems the real space variables are available. Therefore, it makes sense to also use more direct measures of the length scales. One direct space measure that has been used [16, 37] is related to the length of the interface. A second possibility can be derived from the total number of domains in the system. This, as far as we are aware, has not been used before because of the technical difficulty of obtaining this non-local variable.

We will now give detailed definitions of the measures of length which will be calculated in the simulations.

1. **Moments of the radially averaged structure factor.**

   The structure factor corresponding to the order parameter φ is [49]

$$s(\mathbf{k},t) = \left\langle \frac{1}{N} \left| \sum_{\mathbf{x}} e^{i\mathbf{kx}} \varphi(\mathbf{x},t) \right| \right\rangle , \tag{3.2}$$

   where in two dimensions $\mathbf{k} = 2\pi(x/L_x \hat{\imath}_x + y/L_y \hat{\imath}_y)$ for a lattice with dimensions L_x and L_y and $\hat{\imath}_x$ and $\hat{\imath}_y$ unit vectors in x and y directions. The circularly-averaged structure factor is

$$S(k,t) = \frac{\sum_{\hat{\mathbf{k}}} s(\mathbf{k},t)}{\sum_{\hat{\mathbf{k}}} 1}, \tag{3.3}$$

   with $k = 2\pi n/L_{min}$, $n \in \{0,\ldots,L_{min}\}$ and L_{min} is the minimum of L_x, L_y. The sum $\sum_{\hat{\mathbf{k}}}$ is over an annulus defined by $n - 1/2 \leq |\mathbf{k}| L_{min}/(2\pi) < n + 1/2$. Length scales can easily be defined from the moments of the structure factor

$$[k_p(t)]^p = \frac{\sum_k k^p S(k,t)}{\sum_k S(k,t)}. \tag{3.4}$$

We consider all possible combinations of the first three moments that give a length scale:

$$\begin{aligned} R^1 &\sim 2\pi/k_1 \quad R^2 \sim 2\pi/k_2^{\frac{1}{2}} \quad R^3 \sim 2\pi k_1/k_2 \quad R^4 \sim 2\pi/k_3^{\frac{1}{3}} \\ R^5 &\sim 2\pi(k_1/k_3)^{\frac{1}{2}} \quad R^6 \sim 2\pi k_1^2/k_3 \quad R^7 \sim 2\pi k_2/k_3. \end{aligned} \tag{3.5}$$

2. **A real space expression for R^5**

For the measure R_5 a special mathematical simplification applies. If R_5 is defined with the proper periodicity of the discrete Fourier transform, one can show that

$$\begin{aligned} {R_5}^2 \sim R^* &= \frac{\sum_{\mathbf{k}} s(\mathbf{k})}{\sum_{\mathbf{k},\alpha} \sin(k_\alpha) sin(k_\alpha) s(\mathbf{k})} \\ &= \frac{\sum_{\mathbf{x},\alpha} \varphi^2(\mathbf{x},t)}{\sum_{\mathbf{x}} \partial_\alpha^D \varphi(\mathbf{x},t) \partial_\alpha^D \varphi(\mathbf{x},t)} \end{aligned} \tag{3.6}$$

where ∂^D denotes the symmetric discrete partial derivative in direction alpha. It is easy to see equation (3.6) using

$$\begin{aligned} & \sum_{\mathbf{x}} \partial_\alpha^D \varphi(x) \partial_\beta^D \varphi(x) \\ = \;& \frac{1}{4} \sum_x (\varphi(\mathbf{x}+\hat{\imath}_\alpha) - \varphi(\mathbf{x}-\hat{\imath}_\alpha))(\varphi(\mathbf{x}+\hat{\imath}_\beta) - \varphi(\mathbf{x}-\hat{\imath}_\beta)) \\ = \;& \frac{1}{4} \sum_{\mathbf{x}} \sum_{\mathbf{k}} \left(e^{i\mathbf{k}(\mathbf{x}+\hat{\imath}_\alpha)} - e^{i\mathbf{k}(\mathbf{x}-\hat{\imath}_\alpha)} \right) \phi(\mathbf{k}) \sum_{\mathbf{k}'} \left(e^{i\mathbf{k}'(\mathbf{x}+\hat{\imath}_\beta)} - e^{i\mathbf{k}'(\mathbf{x}-\hat{\imath}_\beta)} \right) \phi(\mathbf{k}') \\ = \;& \frac{1}{4} \sum_{\mathbf{k}} \sum_{\mathbf{k}'} \left(e^{k_\alpha} - e^{-k_\alpha} \right) \left(e^{k'_\beta} - e^{-k'_\beta} \right) \phi(\mathbf{k}) \phi(\mathbf{k}') \sum_{\mathbf{x}} e^{i(\mathbf{k}+\mathbf{k}')\mathbf{x}} \\ = \;& -\sum_{\mathbf{k}} \sum_{\mathbf{k}'} \sin(k_\alpha) \sin(k'_\beta) \phi(\mathbf{k}) \phi(\mathbf{k}') \delta(\mathbf{k}+\mathbf{k}') \\ = \;& \sum_{\mathbf{k}} \sin(k_\alpha) \sin(k_\beta) \left| \phi(\mathbf{k}) \right|^2, \end{aligned} \tag{3.7}$$

where $\phi(\mathbf{k})$ is the Fourier transform of $\varphi(\mathbf{x})$. Therefore, R_5 can be evaluated simply by adding real space derivatives. This makes it faster to evaluate and also useful for non-periodic lattices.

3. **Length of interface**

   The length of the interface between the domains L_I provides another length scale:

   $$R^{\circ}(t) = \frac{L_x L_y}{L_I(t)}. \tag{3.8}$$

4. **Number of domains**

   The total number of domains N scales with the system size and, therefore, gives a further measure of length in real space:

   $$R^{\#}(t) = \sqrt{\frac{L_x L_y}{N(t)}}. \tag{3.9}$$

3.2.2 Tests for the length scales

We have a large number of possible measures for length scales. In this section we test their behaviour on two simple series of test patterns. Both series consist of rectangular pattern of $\varphi = 1$ in a surrounding of $\varphi = -1$ connected by a linear interface profile. In the first series the interface is scaled with the rectangular pattern (see Figure 3.1), but it is kept constant in the second pattern (see Figure 3.2). This allows us to estimate how sensitive these measures are to static length. All length scales give the same slope for the pattern without static length scales. This result is shown in Figure 3.1. For the pattern with a static length the results

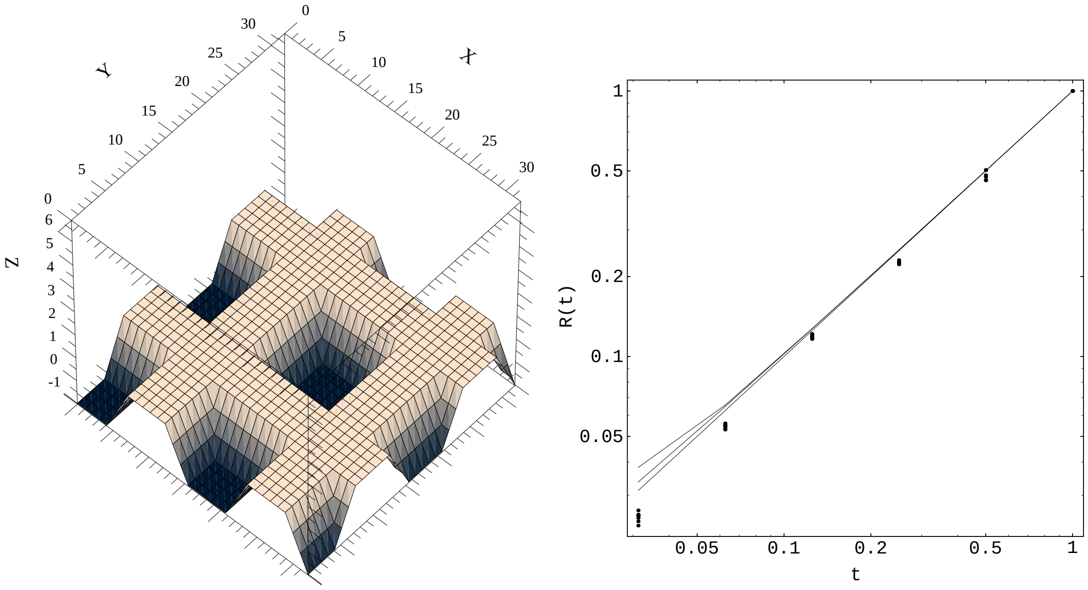

Figure 3.1: Scaling graph for test pattern of $n \times n$ squares where the interface width scales for 256x256 system with $t = 1/n$ for different measures for length. Solid lines represent $\sqrt{R^*}$ (upper line) and $R^\circ, R^\#$ (lower lines).

are shown in Figure 3.2. Only three length scales measure the dynamic length scale correctly. They are R^1, R° and $R^\#$. Even for a very large pattern, when one might expect the interface width to become unimportant, the slope of the different length scales does not converge to the slope corresponding to the relevant length scale.

In order to understand why a static length contributes to length scales derived from the higher moments of the structure factor, even if it is very much smaller than the large length scale we are interested in, we will consider R^5 in detail. The advantage of R^5 lies in the fact that it corresponds to $\sqrt{R^\star}$ which has a real space representation. R^* is defined in equation (3.6) in terms of a sum over the

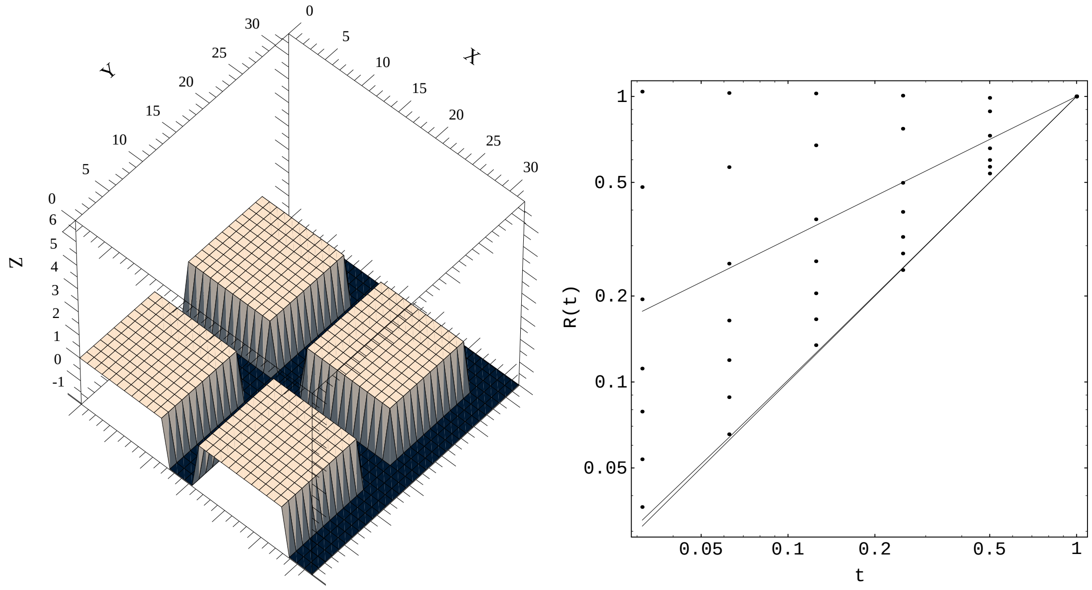

Figure 3.2: Scaling graph for test pattern of $n \times n$ squares with constant interface width of one lattice spacing for 256x256 system with $t = 1/n$ for different measures for length. Solid lines represent $\sqrt{R^*}$ (upper line) and $R^\circ, R^\#$ (lower lines).

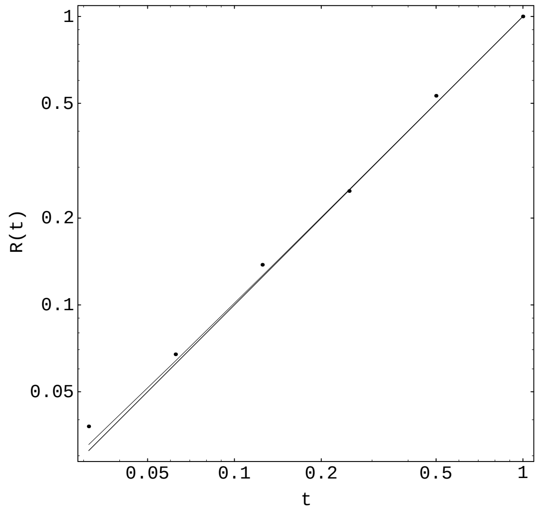

Figure 3.3: Same graph as Figure 3.2 but showing only R°, $R^\#$ and R_1 and also R_5^2 and R^*.

derivatives of the order parameter. Therefore, the only contributions come from the interface. It is clear then that the tensor should scale as the interface length. The second factor to give the dimension of a (length scale)^2 for $R^\star$ has to be the width of the interface. If we plot not R^5 but ${R^5}^2$ we see in Figure 3.3 that the graphs now scale with the dynamic length. If we were to examine the different powers of the interface width contained in the other length scales R_n we could collapse all the scaling graphs of Figure 3.2 onto one line.

It is important to notice that the measures R° and $R^\#$ are by construction insensitive to the behaviour of the interface width. Length scales that we use to measure the dynamic length in our problem are R°,$R^\#$,R_1 and $R^\star$.

3.3 Testing the scaling behaviour

We now examine the growth behaviour of spinodal decomposition for a binary mixture in two dimensions using the free energy lattice Boltzmann approach discussed in the last chapter. We use R_1, R°, and $R^\#$ to measure the dynamic length scale and show real space pictures to illustrate our findings. We show that the numerical data are consistent with a $R \sim t^{\frac{1}{3}}$ scaling law in the limit of an infinite viscosity. Numerical evidence shows, however, that the widely reported scaling law for spinodal decomposition in two dimensions $R \sim t^{\frac{2}{3}}$ is not exact. While the frequently examined measures of the length scale R_1 and also the length scale R° show exactly this scaling law the length scale that is derived from the number of domains $R^\#$ follows a different growth law. This is due to the fact that

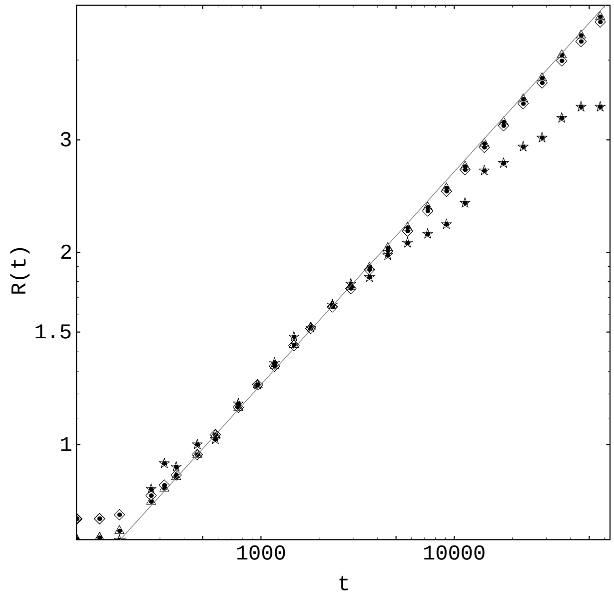

Figure 3.4: Scaling graph for 256x256 system for length scales R_1 ($\diamond$), R° ($\triangle$) and $R^\#$ ($\star$). Parameters are $\Gamma = 2$, $\kappa = 0.002$, $\tau_f = 400$,$\tau_{df} = 1$.

the hydrodynamic effects which lead to an acceleration of the growth of $R^\circ \sim t^{\frac{2}{3}}$ do not affect the merging of domains in the same way. We will also show that within the region where $R^\circ \sim R_1 \sim t^{\frac{2}{3}}$ there exists a transition in the structure of the spinodal pattern for small viscosities where capillary waves are enhanced by the self-induced flow. All simulations are done with initial conditions $\mathbf{u} = 0$, $n = 2$ and $\varphi = 0.02\xi$ where ξ is a uniformly distributed random number in the interval between -1 and 1.

In Figure 3.4 we show the scaling behaviour of a system with extremely high viscosity so that hydrodynamics becomes unimportant. Therefore, the system now resembles a model B system in the language of critical phenomena. The

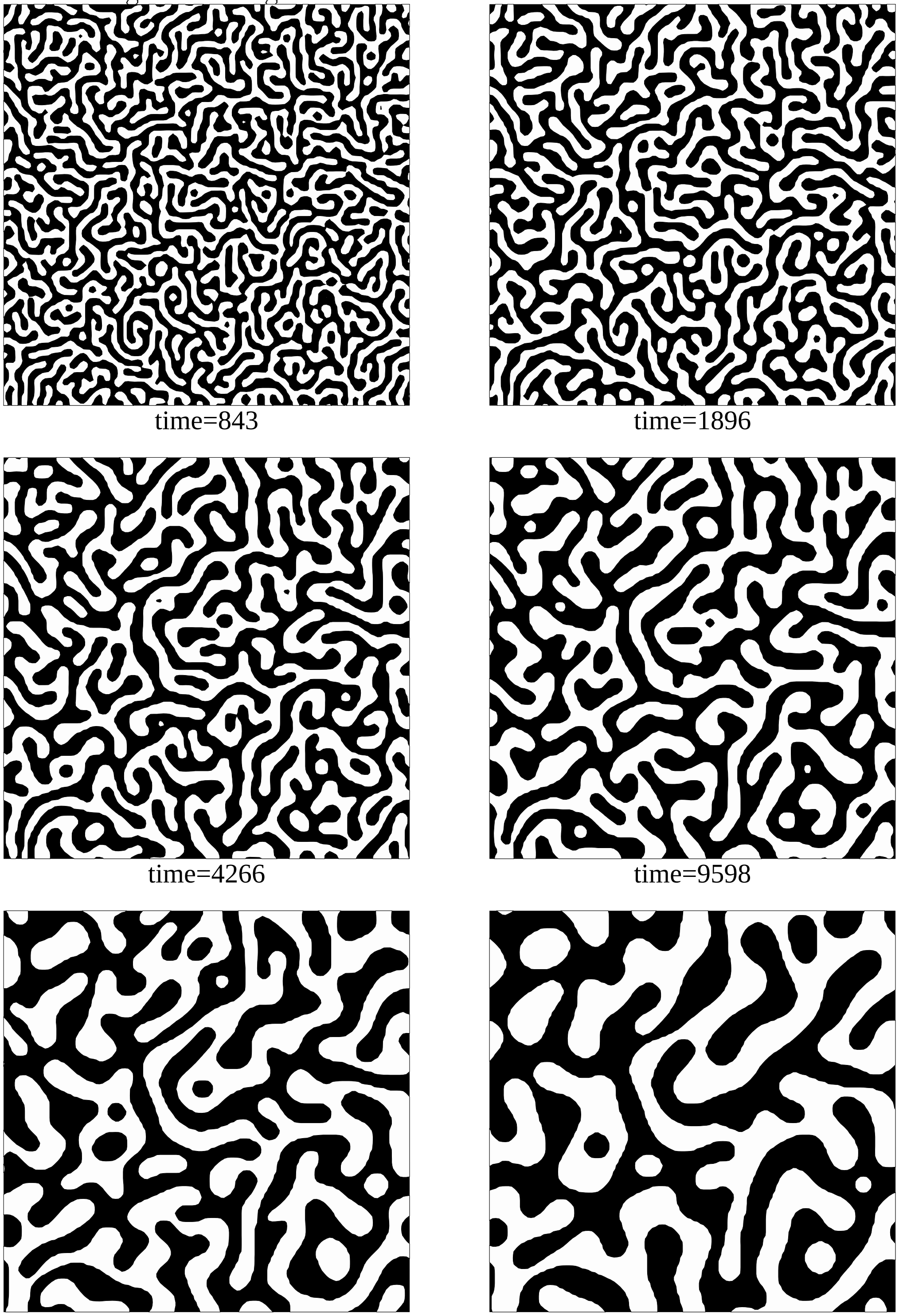

time=843

time=1896

time=4266

time=9598

time=21595

time=48588

Figure 3.5: Real space picture for the evolution of a 256x256 system with parameters $\Gamma = 2$, $\kappa = 0.002$, $\tau_f = 400$ and $\tau_{df} = 1$.

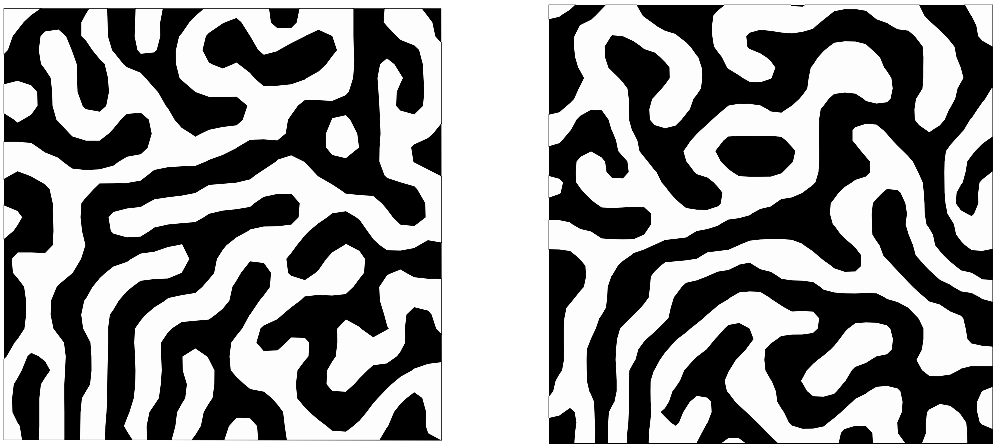

time=843 X66 Y64

time=1896 X86 Y86

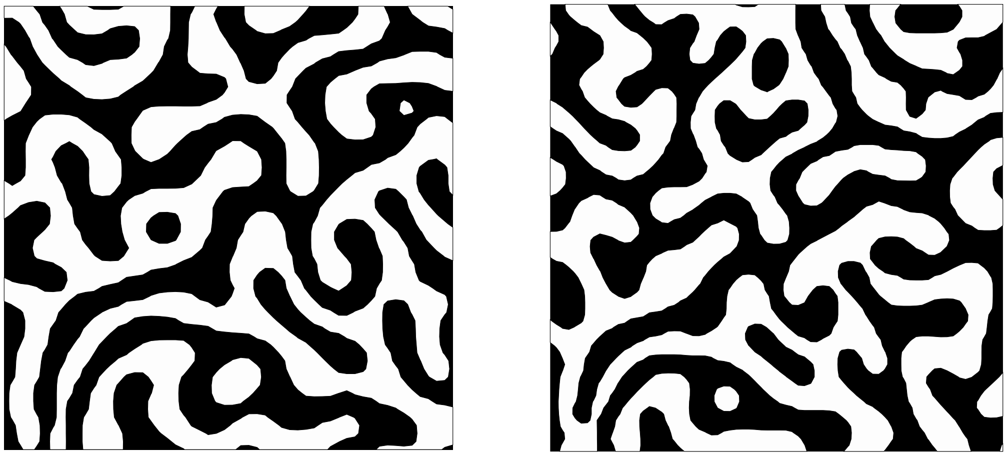

time=4266 X112 Y112

time=9598 X148 Y146

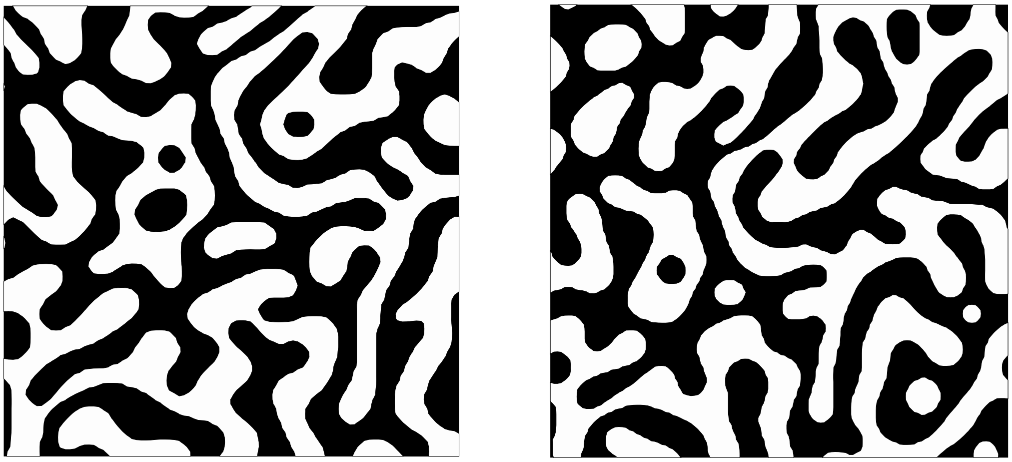

time=21595 X194 Y192

time=48588 X256 Y254

Figure 3.6: Real space picture for the system shown in Figure 3.5 where only a cut-out region with length of the side given by $L = 256(t/t_{\mathrm{end}})^{\frac{1}{3}}$ is shown. We see that the evolution is consistent with scaling.

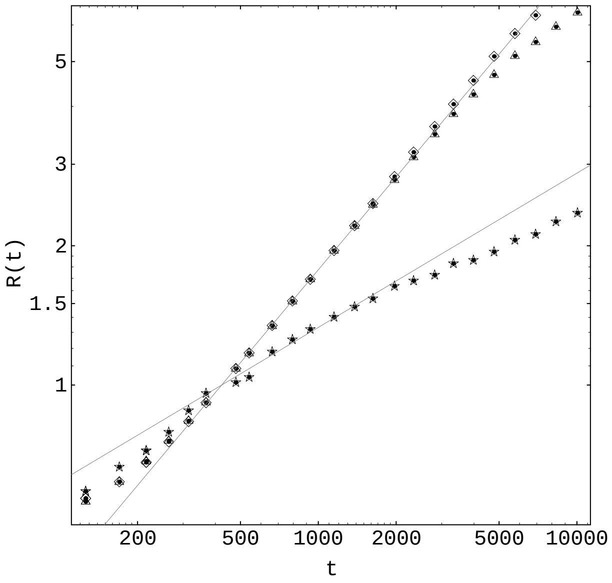

Figure 3.7: Scaling graph for 256x256 system for length scales R_1 ($\diamond$), R° ($\triangle$) and $R^\#$ ($\star$). Parameters are $\Gamma = 2$, $\kappa = 0.002$, $\tau_f = 1$ and $\tau_{df} = 1$.

measures of length R_1 and R° show very clearly a $t^{\frac{1}{3}}$ growth law. The $R^\#$ measure also shows a clear $R^\# \sim t^{\frac{1}{3}}$ behaviour for small times, but for late times the statistic becomes poor with only eight white and four black domains left for t=48588. The picture is thus consistent with the usual scaling hypothesis with $R \sim t^{\frac{1}{3}}$ for a model B system. In Figure 3.5 the real space pattern of this system is shown. The coarsening of domains can clearly be seen. To illustrate the scaling hypothesis we have shown details of the contour plots enlarged by a factor of $(t_{\text{end}}/t)^{\frac{1}{3}}$ in Figure 3.6. The pictures show statistically equivalent patterns, indicating the structure of the universal scaling state.

For intermediate viscosities, which we take to be viscosities that are small

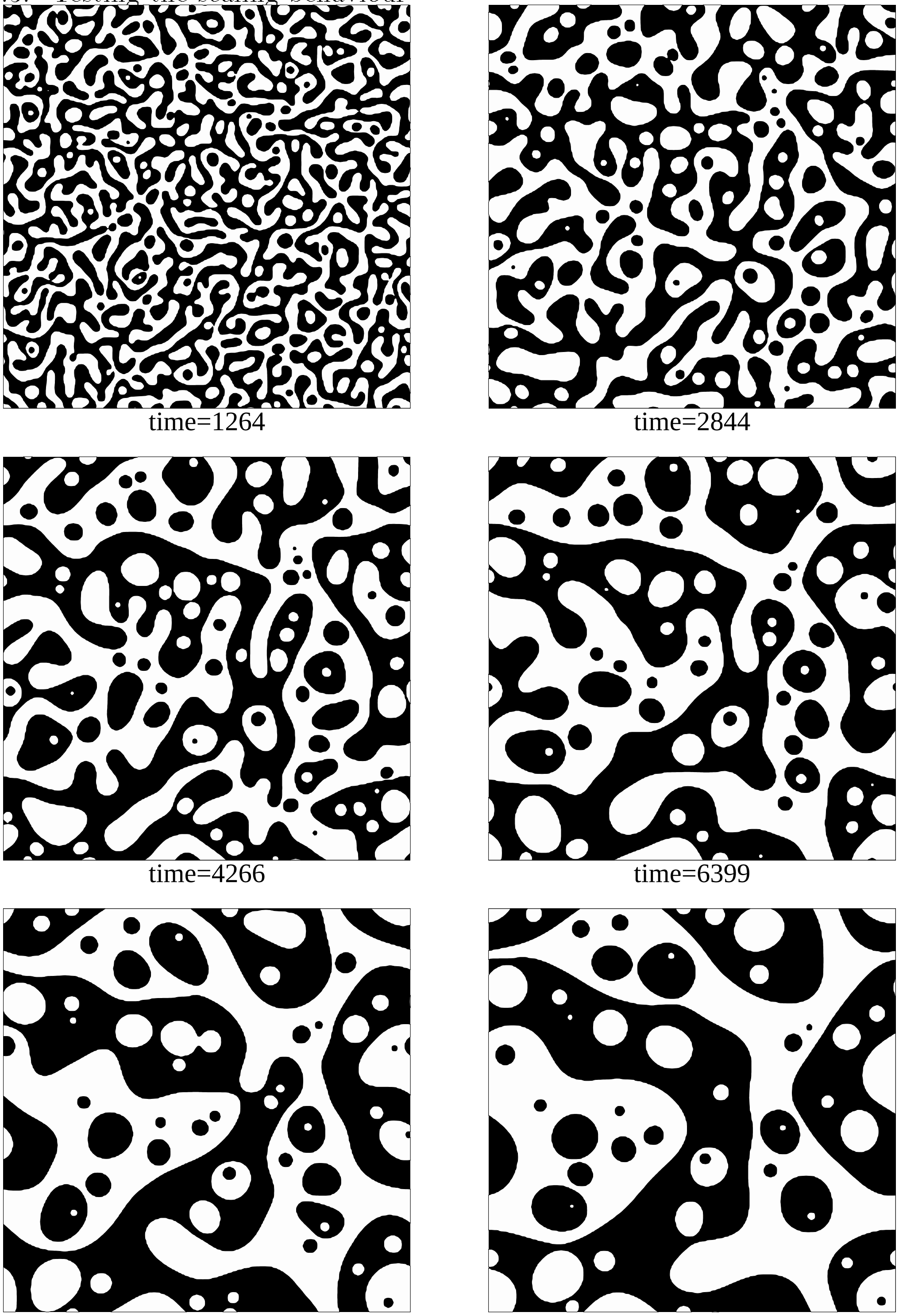

time=1264 time=2844

time=4266 time=6399

time=9598 time=14397

Figure 3.8: Real space picture for the evolution of a 256x256 system with parameters $\Gamma = 2$, $\kappa = 0.002$, $\tau_f = 1$ and $\tau_{df} = 1$.

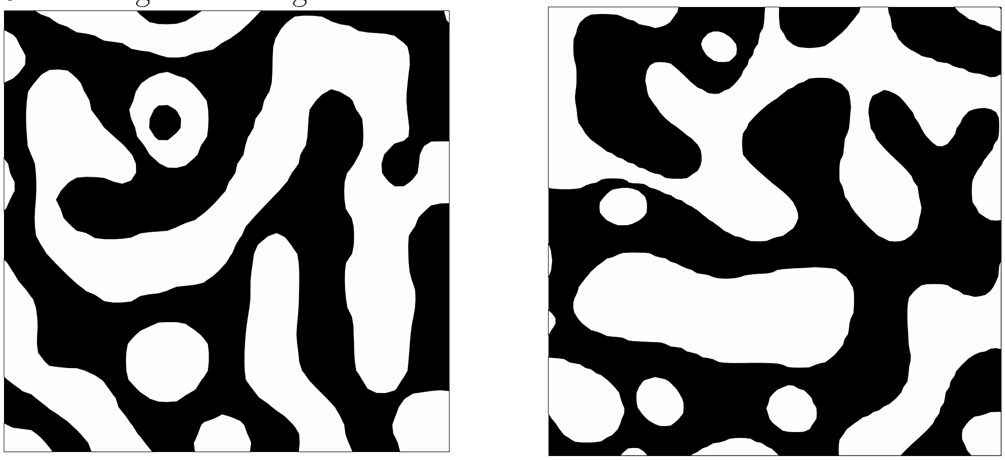

time=1264 X100 Y100

time=2844 X172 Y172

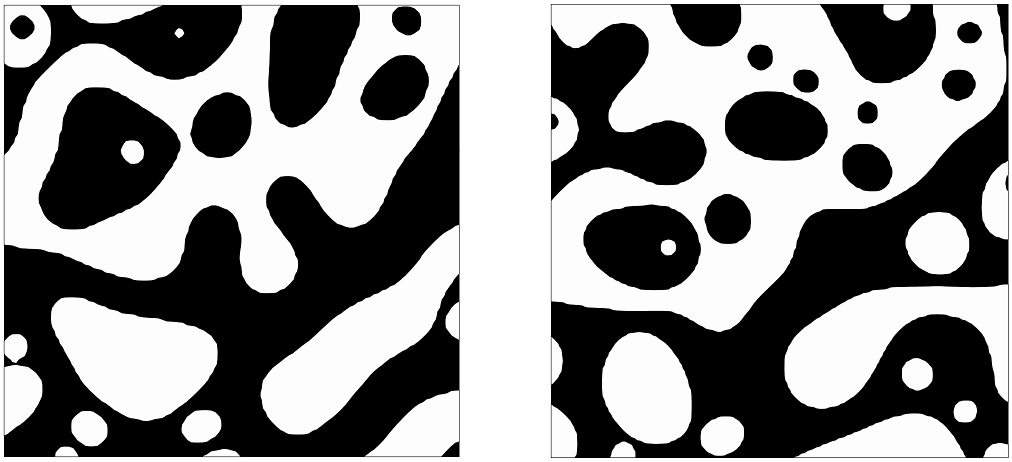

time=4266 X226 Y226

time=6399 X298 Y296

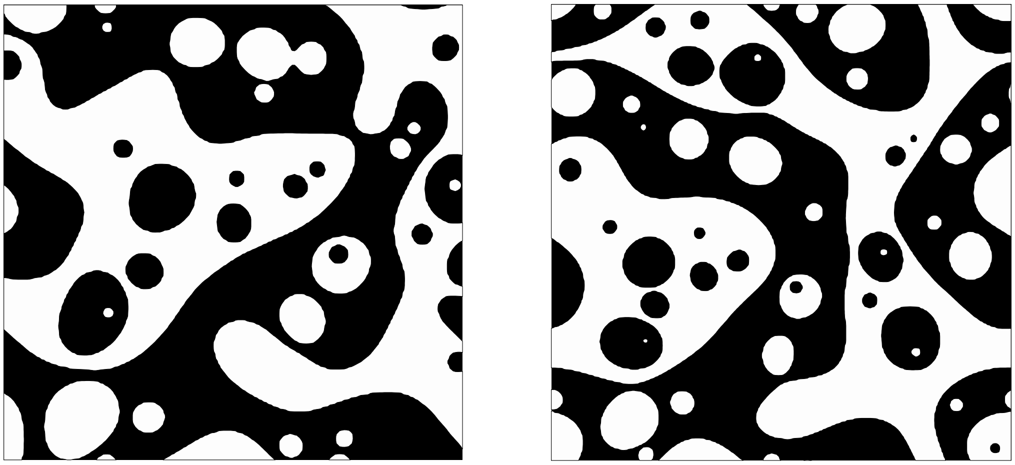

time=9598 X390 Y388

time=14397 X512 Y510

Figure 3.9: Real space picture for the system shown in Figure3.8 where only a cut-out region with length of the side given by $L = 256(t/t_{\text{end}})^{\frac{2}{3}}$ is shown. We see a small increase of the number of domains for late times.

enough to allow for the development of flow, but also large enough to damp out capillary waves, we observe the well-known growth law with exponent $\frac{2}{3}$ for the length scales R_1 and R°. The growth law for $R^\#$, however, crosses over to $R^\# \sim t^{\frac{1}{3}}$. The scaling graphs are shown in Figure 3.7. This means that the number of domains decreases slower than it would if the system was in a scaling state. This is seen in the scaled details shown in Figure 3.9 for the time evolution of a system with medium viscosity. The number of domains increases in time and the structure does not correspond to a scaling state. The physical reason for this lies in the fact that in two dimensions a spinodal decomposition structure cannot be bi-continuous for topological reasons. Therefore, a large number of domains exist that can deform by a surface tension driven flow. We observe that the induced flow does not increase the growth exponent for $R^\#$ and, therefore, the coalescence rate of domains. While the interface curvature of the domains is rapidly decreased with the help of the flow the number of domains increases not much faster than without the flow. This leads to an increasing number of isolated circular domains within larger domains. These isolated circular domains can now only change by diffusion or by coalescence. For both of these mechanisms a growth law of $R \sim t^{\frac{1}{3}}$ has been predicted and observed.

Therefore, we observe a change in the structure of the spinodal decomposition pattern towards a structure that consists of large, deformed domains that give the largest length in the system R_{max} and a growing hierarchy of domains within domains contained therein on smaller length scales. The smaller the domains the more circular they become and the gradients of the flow field that could enhance the coalescence process in this region vanish since the surface tension cannot drive local flow in this region anymore. The vanishing of the circular domains, therefore, has to be a slower process than the creation of circular domains on larger length scales via the hydrodynamic mechanism. As a result, the depth of the hierarchy of circular domains within circular domains has to increase with time as the evolution progresses.

The structural change in the system is not heralded by a change in the growth law for the measures of length scale R_1 and R°. That is probably the reason why this phenomenon has, to the best of my knowledge, not been described before and scaling has been assumed [42]. The reason lies in the fact that R_1 has been constructed only to measure the largest non vanishing contribution to the structure factor in order not to pick up contributions from the constant interface width. So only the largest domain structure that continues to grow via the hydrodynamic mechanism contributes to the growth law for R_1. The measure R° is derived from the interface length. Therefore, in the beginning when the proportion of the interface length of the circular domains is small, compared to the total interface length, R° is not sensitive to the structural change. For large times one can just about see a decrease in the growth of R° in Figure 3.7.

The measure $R^\#$, on the other hand, relies on counting the domains. Therefore, the contributions of many small domains dominate the contribution from the few large ones. The small domains, however, only grow via diffusion and coalescence. This stresses the importance of $R^\#$ as a very good measure of the fine structure of the system that is nevertheless independent of the interface width.

I thank Professor Cardy for pointing out that there exist scaling systems in which the measure based on the number of domains does not scale[1]. A better measure could be derived from the number of domains with a size larger than a certain percentage of the domain size. In our system, however, even such a measure would not scale. If we inspect Figure 3.9 we see that the number of domains larger than say 1/4 of the typical domain width increases with time.

Another way of testing the violation of scaling would be to plot the circularly averaged structure factor in the scaling form $R(t)^{-2}S(k)$ against $kR(t)$, where $R(t)$ is the largest length scale (which could be taken as R_1). Then scaling violations would appear as a breaking away from a universal curve at some kL, providing the break point occurs at some fixed kL, or even a decreasing kL, as time increases. If, however, the break point is pushed to larger kL at later times, the evidence for scaling violations would be weaker.

For even lower viscosities a transition occurs when the damping of capillary waves becomes so small that the energy of the flow, due to the surface tension, causes capillary waves on the interfaces. The oscillations reach the size of the domain thickness leading to a rupturing and colliding of domains that slows the domain growth. The surface tension accelerates the interfaces towards a constant curvature, but the viscosity is so small that the relaxation process of the interface overshoots. This overshooting process makes it difficult for the energy stored in the interface to dissipate. This leads to complicated flow patterns that efficiently

---

[1] An example for this are percolation clusters near the percolation threshold. For this problem the curve in Figure 3.7 would actually be asymptotically flat. Yet no-one would claim that this problem violates scaling.

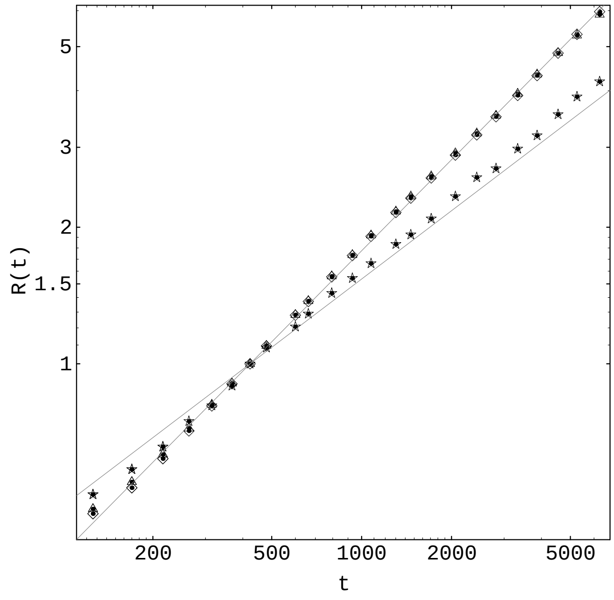

Figure 3.10: Scaling graph for 1024x1024 system for length scales R_1 ($\diamond$), R° ($\triangle$) and $R^\#$ ($\star$). Parameters are $\Gamma = 2$, $\kappa = 0.002$, $\tau_f = 0.56$ and $\tau_{df} = 1$.

enhance the collision of droplets so that the growth law for the length $R^\#$ derived from the number of droplets is changed from $R^\# \sim t^{\frac{1}{3}}$ to $R^\# t^{\frac{1}{2}}$, as shown in Figure 3.10. The growth law for the two other measures is unchanged: $R_1 \sim R^\circ \sim t^{\frac{2}{3}}$, although the multiplying factor is reduced for lower viscosities. The patterns can only grow at a rate at which the kinetic energy is dissipated, allowing larger domains to form.

The real space pictures of the spinodal decomposition patterns in Figure 3.11 do look very different from usual spinodal decomposition pictures. The domains are rugged because of the massive capillary waves on the interfaces. Compared to the medium viscosity pictures the number of isolated circular domains grows

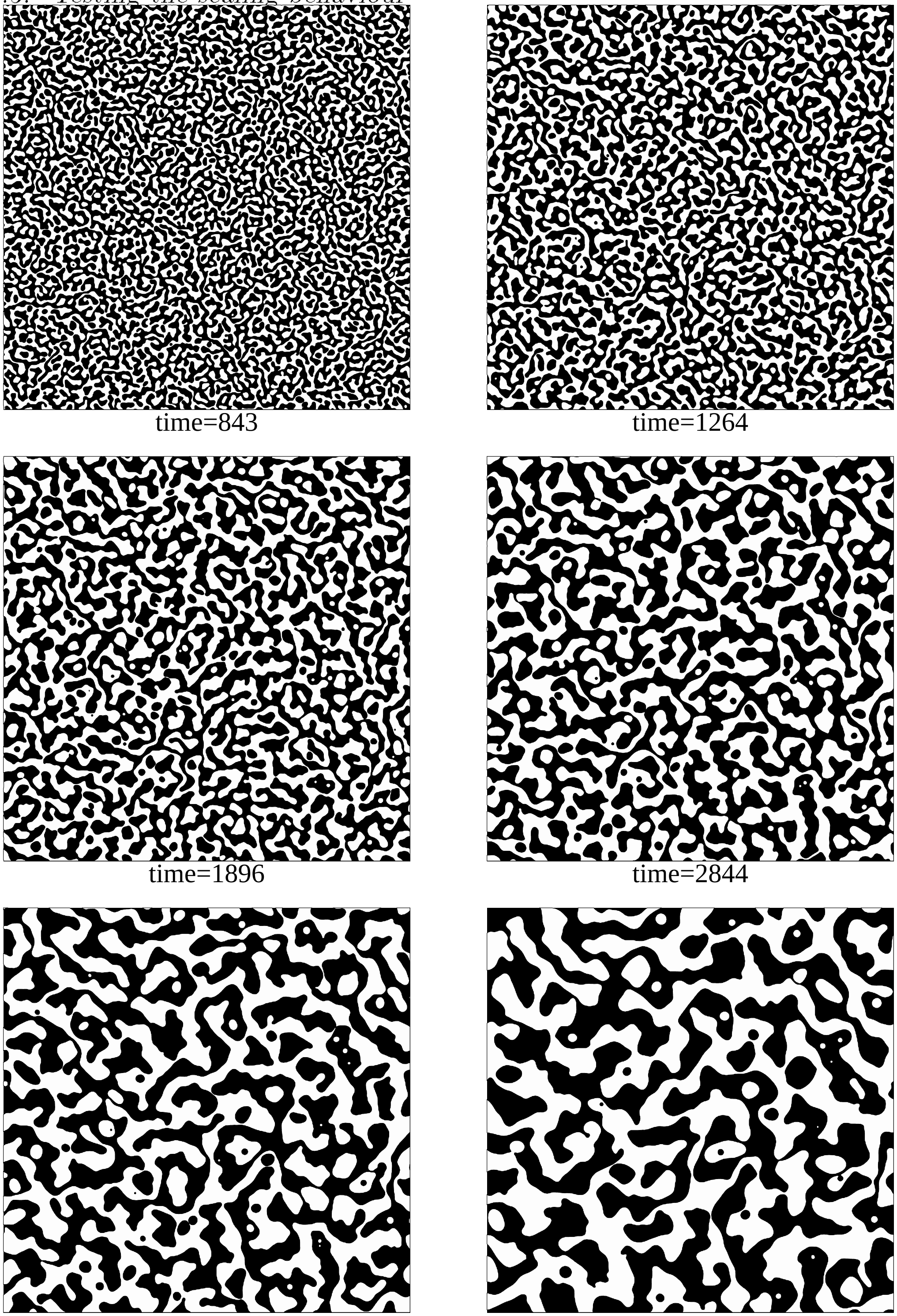

time=843

time=1264

time=1896

time=2844

time=4266

time=6399

Figure 3.11: Real space picture for the evolution of a 1024x1024 system with parameters $\Gamma = 2$, $\kappa = 0.002$, $\tau_f = 0.56$ and $\tau_{df} = 1$.

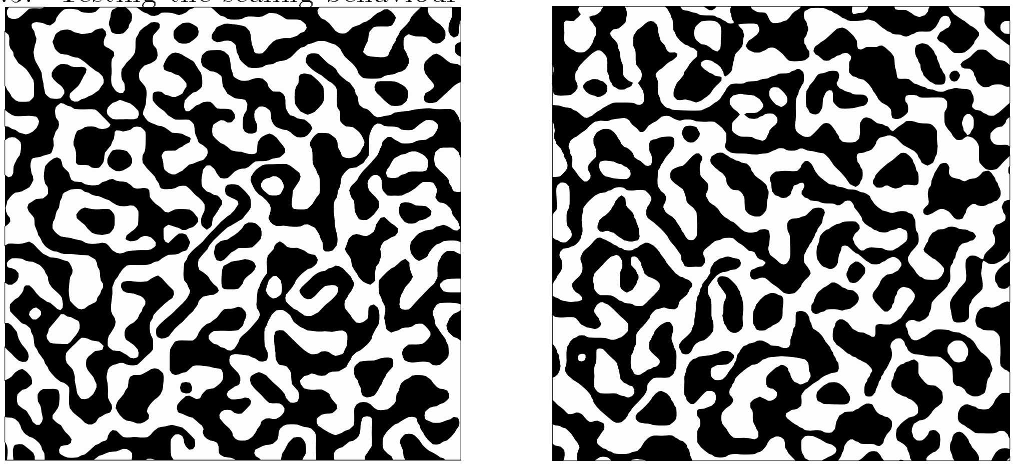

time=843 X264 Y264

time=1264 X346 Y346

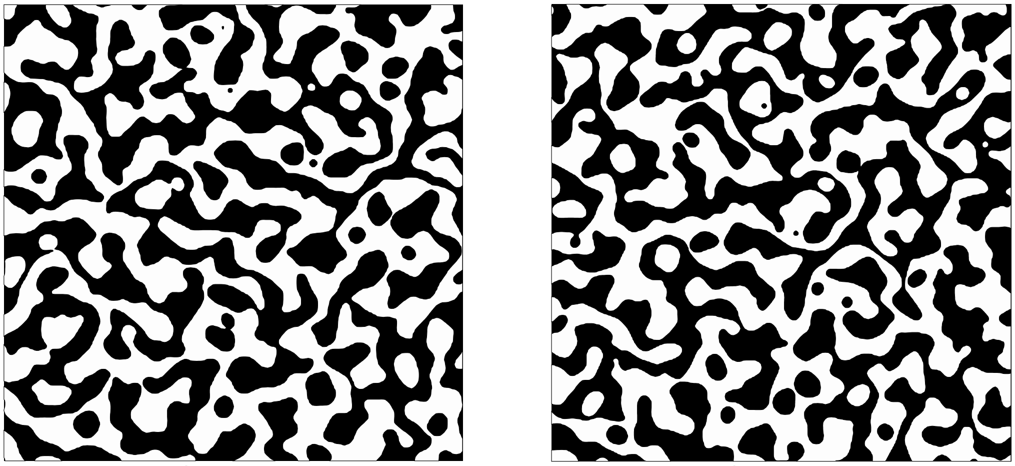

time=1896 X454 Y454

time=2844 X596 Y594

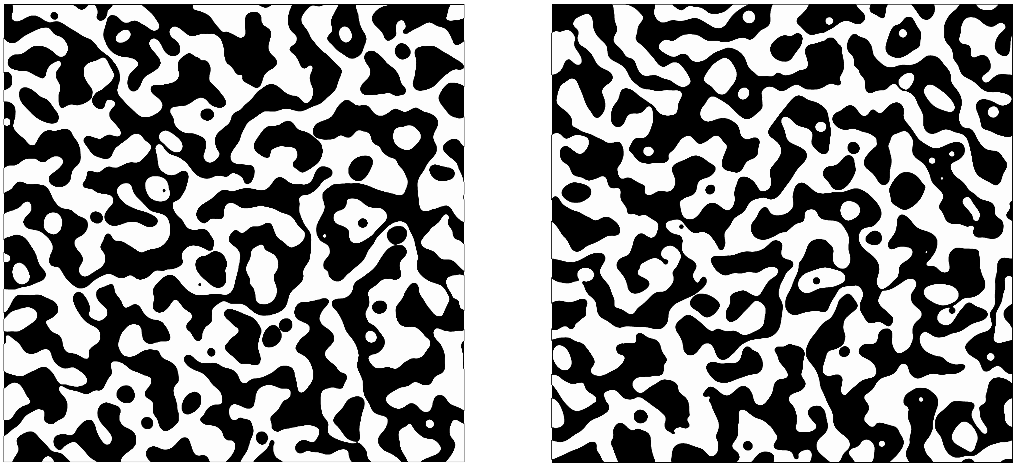

time=4266 X780 Y778

time=6399 X1024 Y1022

Figure 3.12: Real space picture for the system shown in Figure 3.11 where only a cut-out region with length of the side given by $L = 1024(t/t_{\text{end}})^{\frac{2}{3}}$ is shown. We see a small increase of the number of domains for late times.

much less rapidly. An increase of these circular domains, however, is still clearly visible in the scaling picture Figure 3.12 in accordance with the difference of the growth laws of R° and $R^\#$.

An interesting open question is the behaviour of the spinodal decomposition patterns in the limit of a vanishing viscosity or an infinite surface tension. In these cases the hydrodynamic processes cannot lead to domain growth because the energy stored in the flow field will rupture and deform the domains so that only diffusive contributions are possible. It is also possible that in this limit domain growth does not occur at all.

3.4 Summary

Guided by the question how scaling states for dynamic phase ordering phenomena differ for different growth regimes we were led to the conclusion that no scaling states exist for hydrodynamically coarsening binary mixtures in two dimensions. While the ordering phenomena without hydrodynamics lead to a scaling state, the hydrodynamic ordering for intermediate viscosities produces a rich structure of a growing hierarchy of circular drops within the deformed domains on the largest length scale.

For small viscosities the coarsening mechanism excites capillary waves that slow down the growth process. The capillary waves cause dynamic, irregular domains that enhance the collisions of drops within the domains with the domain walls and, therefore, partially cleaning the large domains of their included drops.

We will see a similar process taking place for spinodal decomposition under shear flow (see Figure 5.7 and discussion in text).

We were able to quantify our findings with the help of a new measure for a length scale derived from the number of drops. It has the advantage of being sensitive to small scale structure. Fourier methods that resolve smaller length cannot distinguish between the small scale structure and the interface width, which is a constant length and therefore is not expected to scale.

Chapter 4

Double phase transition

In this short chapter we report a first successful simulation of the phenomenon of double phase separation, first identified by Tanaka [60] in 1994.

Normally in spinodal decomposition, nucleation of the domains is followed by their growth. In experiments, however, a second round of phase nucleation is sometimes observed in the phase-ordering domains. This phenomenon was first described by Tanaka [60] in the quasi two-dimensional geometry of a binary mixture confined in a narrow gap between two plates. In his paper he discusses several possible explanations, including three-dimensional ones such as wall effects, but clearly favours a purely two-dimensional explanation.

This explanation rests on the assumption of an unusually strong hydrodynamic or a very long diffusive time scale. Consider a near symmetric quench of a low-viscosity binary mixture where the hydrodynamic phase ordering process is much faster than the diffusive phase ordering process. Then, in the spinodal decomposition, the hydrodynamic phase ordering can start to act long before the diffusion establishes domains of near-equilibrium concentrations. This happens because the surface tension of the interfaces can induce a flow that orders the domains even before they are fully developed.

This results in large domains with order parameters that are still far from the equilibrium concentrations corresponding to the quench temperature. Indeed, the order parameter in the large domains can be so far from the equilibrium value that a second phase separation, analogous to a nucleation for an off-critical quench at this concentration, occurs. Tanaka called this process an interface quench. It is not surprising that this very slow nucleation process is possible, when one recalls that single circular bubbles are very stable within a domain undergoing hydrodynamic coarsening as shown in the last chapter for spinodal decomposition with an intermediate viscosity.

While this explanation is very plausible no one had been able to reproduce the phenomenon in a simulation. Earlier work of Shinozake and Oono [54] did show that it is possible for a hydrodynamic system not to reach the final equillibrium value for the order parameter before phase ordering started, but a second phase transition was not observed.

The lattice Boltzmann method has the advantage of being able to access a large range of different values for the hydrodynamic and diffusive time scales. In order to observe the interface quench we combine an intermediate viscosity ($\tau_f = 0.65$) with a very low mobility $\Gamma = 0.001$ (i.e., a lower viscosity would lead to capillary waves that would cause many nucleation sites to recombine at the

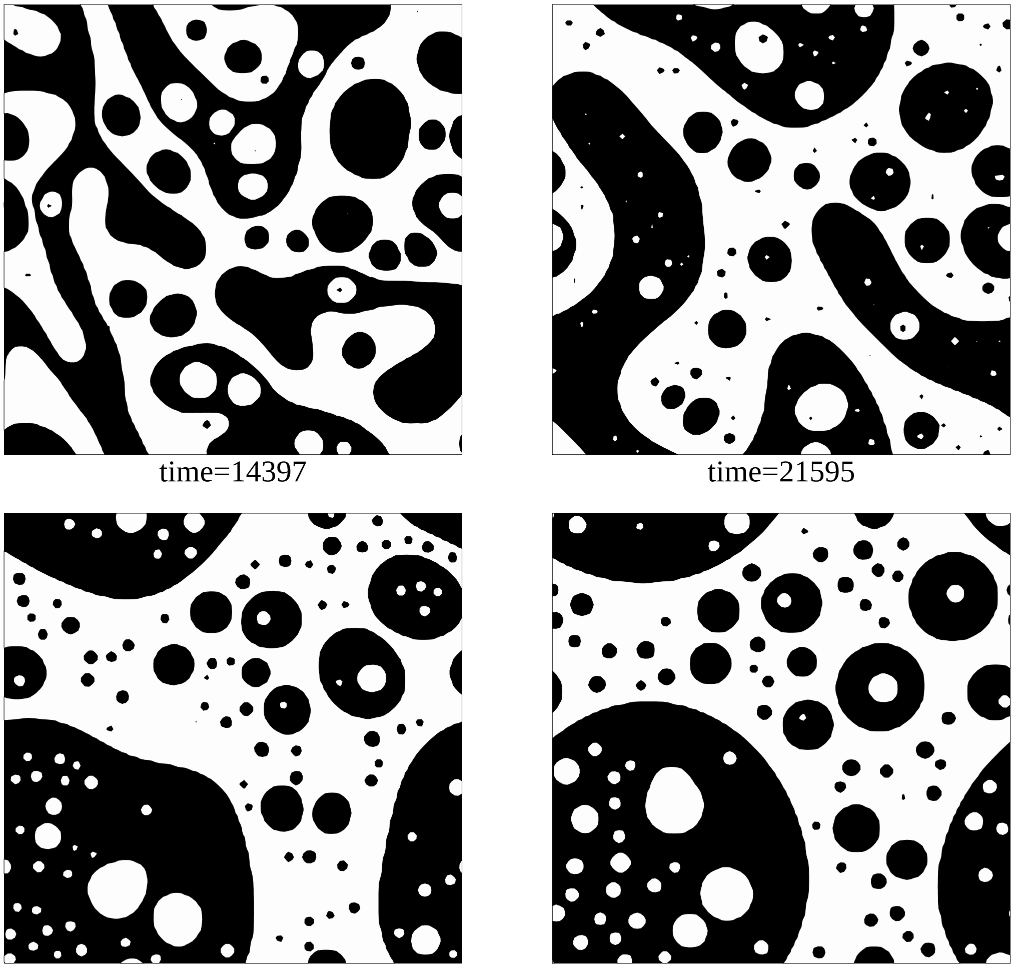

time=14397

time=21595

time=32392

time=48588

Figure 4.1: Double phase separation after spinodal decomposition of a 250x250 system with parameters $\Gamma = 0.001$, $\kappa = 0.002$, $\tau_f = 0.65$ and $\tau_{df} = 1$.

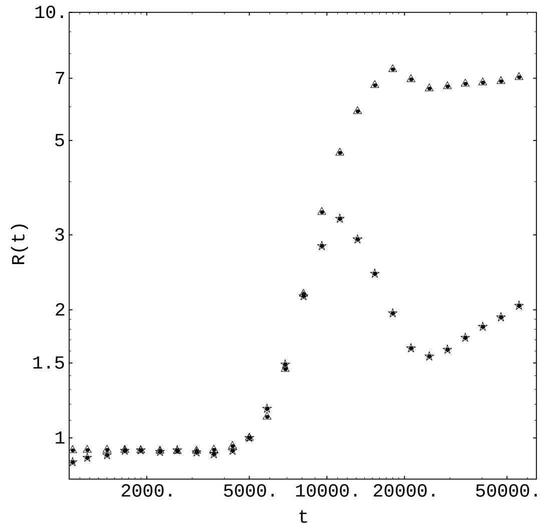

Figure 4.2: Scaling graph of length scales R° ($\triangle$) and $R^{\#}$ ($\star$) for system of Figure 4.1.

interface of the large domains). The other parameters are the same as in the last chapter. The effect of the low mobility is to decrease the diffusion by a factor of 1/200 in comparison to the simulations in the last chapter.

The results of the simulations are shown in Figure 4.1. The double phase separation caused by the interface quench is clearly seen in the snapshots of the decomposition pattern. We first note that the phase separation is much slower because of the low mobility. Until a time earlier than about 9000 the phase separation pattern is similar to a pattern for a spinodal decomposition with a medium viscosity. At time 21595 we see a nucleation of new drops in the large domains. By the time 32392 the nucleation is almost complete, while the phase ordering process has transformed almost all domains into compact shapes. At the latest time the nucleation is over and even the newly nucleated drops have started to coarsen via coalescence and diffusion. This can also be seen in the scaling plot for R° and $R^{\#}$ in Figure 4.2. Especially $R^{\#}$, depending on the number of domains, is a very sensitive measure for the nucleation of new domains.

It may seem surprising that we have been able to observe nucleation in a lattice Boltzmann simulation without noise. This is only possible because the domains, coarsening via the hydrodynamic mode, already contain the fluctuations that are the seeds for the nucleation. These are only growing very slowly via the diffusive mode. Note the strong similarity between our simulation and the pictures of experiments in [60]. We have recently received a preprint by Tanaka and Araki [61] where they perform a finite difference simulation (with noise) of a Langevin formalism of model H. There they succeeded in producing numerical evidence of a second round of nucleation.

In conclusion, we want to emphasize the flexibility of our lattice Boltzmann approach, which allows us to simulate with ease even such extreme situations as Tanaka's interface quench mechanism.

Chapter 5

Spinodal decomposition under shear

In this chapter we examine the effects of an imposed shear flow on a system undergoing spinodal decomposition. Such systems have received much interest in the recent past[38, 30, 17, 32].

In 1988 Chan, Perrot and Beysens [6] performed an experiment in which they examined a high viscosity polymer mixture undergoing spinodal decomposition under shear flow. They found that a very large shear rate can prevent the phase separation process. At a smaller shear rate their system does phase separate and after an initial time the domains deform. The angle of the orientation of the domains with the shear direction decreases from an initial 45° to 0° for large times.

In 1990 Ohta and Nozaki [43] performed a two-dimensional computer simulation of domain growth under shear flow starting from a phase separated configuration. The simulations were performed using the cell dynamic approach, a model that simulates phase separation but does not include hydrodynamics. They observed stretching and breaking of domains followed by colliding and merging of domains.

In the same year Rothman [51] used a lattice gas model to investigate a two-dimensional binary mixture in a V-shaped shear flow. This model has the advantage of combining the phase separation with hydrodynamics. He reports an increase in the overall viscosity for low shear rate (shear thickening) where the interfaces are stretched by the shear flow and a decrease in the overall viscosity at higher shear rates as the domains are breaking earlier (shear thinning). In 1995 Olson and Rothman [38] introduced a three-dimensional version of the model and improved their shear boundaries to implement Lees-Edwards boundary conditions which are explained in detail below.

The shear thickening and shear thinning phenomena were observed in an experiment by Läuger [32], who also reports scaling of the deformation for different shear rates. In the same year Hashimoto *et al.* [23] showed that domains in spinodal decomposition can be elongated into extremely long stripes under strong shear flow. The shear flow stabilizes the string against their intrinsic surface tension instabilities. Many more recent results are summarized in a recent review of Onuki [39] and references therein.

In this chapter we examine the effects of simple shear flow on the spinodal decomposition of a binary mixture. We introduce different ways to implement a simple shear flow in a Lattice Boltzmann scheme. Because shear flow deforms the domains we generalize the measures of length introduced in the last chapter. The new measures give two length scales and the orientation of the non-isotropic pattern. With these measures we examine the effect of internal hydrodynamics on the sheared pattern and find different behaviour for high and intermediate viscosities.

The two-dimensional equivalent of the strings observed by Hashimoto *et al.* [23] are stripes that are stabilized by the shear flow. We examine the effect of shear flow on such stripes and explain oscillations of stripes, observed in simulations. In the conclusions we point out some unexplored problems and suggest further improvements on the algorithm.

5.1 Shear boundary conditions

Possibly the easiest way to introduce shear flow in a Lattice Boltzmann simulation is to include moving walls in a lattice direction. Even for a neutral wall with neutral wetting, however, phase separation is strongly enhanced at the walls and the wall effects easily dominate the phase separation process for all but the largest systems. The effect of walls on the phase separation is an interesting phenomenon in its own right, but it is not the problem we are interested in studying here.

We can overcome the problem caused by walls in a relatively simple and efficient manner by introducing a Klein-bottle symmetry to the lattice. To simulate shear flow the mixture is then forced along one line in the direction of the shear

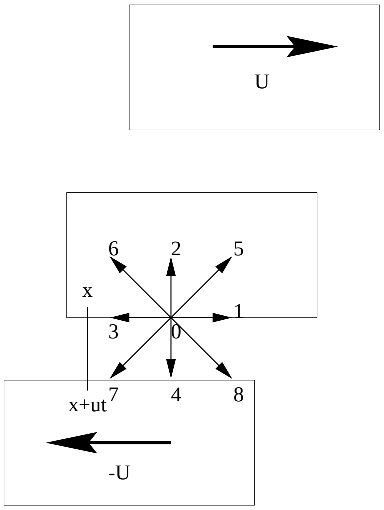

Figure 5.1: Schematic representation of a Lee Edwards boundary condition for a lattice Boltzmann method. The System is periodic in x-direction and is connected by a Galilean transformation in the y-direction. This leads to a time dependent off-lattice periodicity and a need to transform the densities in velocity space.

flow to have a given velocity component in this direction. In a one-component mixture this induces a linear velocity profile. For a two-component mixture, however, there are non-local interactions and the dynamics is influenced by the v-shaped velocity profile at the forcing line. We used this algorithm to produce preliminary results but it has no advantages over the method derived below. Therefore, these results are not presented here.

To produce a more regular shear flow we can build on the ideas of Lee and Edwards to construct the equivalent of Lee-Edwards boundary conditions, widely used in Molecular Dynamics [33], to the lattice Boltzmann simulations. Let us first review the ideas of Lee and Edwards. To simulate shear boundary conditions, for a shear in x-direction, in a simulation box of dimensions (L_x, L_y) they introduce periodic boundary conditions for the walls in y-direction. Particles that leave the box at the lower boundary at position $(x, y = 0)$ reappear at the upper boundary at position $(x + ut(\mathrm{mod}X), y = Y)$ with a velocity that is changed by $v \to v + u$.

To implement this idea for lattice Boltzmann simulations we are faced with two difficulties. Firstly the densities are defined on a lattice and the boundary conditions lead to densities defined between the lattice points. Secondly we need to define a Galilean transformation for the densities which are streamed across the lattice.

The non-fitting of the lattice is relevant for both the streaming and the calculation of derivatives at $y = 0$ and $y = L_y - 1$. We solve this problem by a linear interpolation scheme. For any density we define

$$f[x, y = -1] = (1-R(ut))f[x+I(ut), y = Y-1]+R(ut)f[x+I(ut)+1, y = Y-1] \tag{5.1}$$

where $I(x)$ is the largest integer with $I(x) < x$ and $R(x) = x - I(x)$. If we pass the break in the lattice from the other side we define similarly

$$f[x, y = Y] = (1-R(ut))f[x-I(ut), y = Y]+R(ut)f[x-I(ut)-1, y = Y]. \tag{5.2}$$

These formulae are used both for the streaming of the Galilean-transformed Boltzmann densities f_i and for the calculation of density gradients.

It is rather more difficult to see how a Galilean transformation should be defined. Let us consider the special case of a nine-velocity model where the velocities are numbered as indicated in Figure 5.1. We need to perform a Galilean transformation on the $\{f_5, f_2, f_6\}$ and the $\{f_7, f_4, f_8\}$ velocities. To define the transformation we demand mass conservation, an appropriate change in momentum and a conservation of the local pressure. For the density this implies

$$n = f_5 + f_2 + f_6 = f_5' + f_2' + f_6' \tag{5.3}$$

and for the x-momentum

$$u_x = \frac{f_5 - f_6}{n} = \frac{f_5' - f_6'}{n} - u = u_x' - u. \tag{5.4}$$

where the prime denotes the transformed quantities. For the pressure we require

$$\begin{aligned} P_{xx} &= \sum \frac{f_i}{n^2}(nv_{ix} - nu_x) \\ &= \frac{1}{n^2}(f_5(n - u_x)^2 + f_2(nu_x)^2 + f_6(-n - nu_x)^2 \\ &= \frac{1}{n^2}(f_5'(n - u_x')^2 + f_2'(nu_x')^2 + f_6'(-n - nu_x')^2. \end{aligned} \tag{5.5}$$

This system of equations can be solved to give a unique solution for the Galilean-transformed densities f_i'

$$f_2' = f_2 + 2(f_5 - f_6)u - nu^2 \tag{5.6}$$

$$f_5' = f_5 + (-\frac{3}{2}f_5 - \frac{1}{2}f_2 + \frac{1}{2}f_6)u + \frac{n}{2}u^2 \tag{5.7}$$

$$f_6' = f_6 + (-\frac{1}{2}f_5 + \frac{1}{2}f_2 + \frac{3}{2}f_6)u + \frac{n}{2}u^2. \tag{5.8}$$

In order for this transformation to make sense we need to make sure that equation (5.4) is consistent with the definition of the equilibrium distribution. We will now show that this is indeed not the case for any equilibrium distribution that is defined as a polynomial in second order in u. A generic expansion is

$$f_i^0 = A + B u_\alpha v_{i\alpha} + C u^2 + D u_\alpha u_\beta v_{i\alpha} v_{i\beta} + G_{\alpha\beta} v_{i\alpha} v_{i\beta}. \tag{5.9}$$

Again defining $n = f_5 + f_2 + f_6$ it follows that

$$\frac{f_5 - f_6}{n} = \frac{2B + 4Du_y}{3A + 3Bu_y + 3Cu^2 + 3Du_y^2 + 2Du_x^2 + 3G_{yy} + 2G_{xx}} u_x + \frac{4}{n} G_{xy} \neq u_x + \mathcal{P}, \tag{5.10}$$

where $\mathcal{P}$ is a velocity-independent term. The equilibrium distributions do not transform under the Galilean transformation. In practice this leads to a step in the u_x profile at the boundary.

There is, however, no *a priori* reason to use a second-order expansion in the velocity for the equilibrium distribution. All that is needed for a valid equilibrium distribution are the conservation laws and the symmetry of the lattice. We will demand the usual conservation laws for the densities

$$\sum_i f_i^0 = \sum_i f_i = n, \tag{5.11}$$

$$\sum_i f_i^0 v_i = \sum_i f_i v_i = nu, \tag{5.12}$$

$$\sum_i f_i^0 v_{i\alpha} v_{i\beta} = nT_{\alpha\beta} + n u_\alpha u_\beta, \tag{5.13}$$

plus a set of additional constraints that ensure consistency of the Galilean transformation for the velocity

$$\frac{f_1^0 - f_3^0}{f_1^0 + f_0^0 + f_3^0} = u_x, \tag{5.14}$$

$$\frac{f_2^0 - f_4^0}{f_2^0 + f_0^0 + f_4^0} = u_y \tag{5.15}$$

and the pressure

$$f_5^0 + f_6^0 - (f_5^0 + f_6^0 + f_2^0)(T_{xx} + u_x u_x) = 0, \tag{5.16}$$

$$f_5^0 + f_8^0 - (f_5^0 + f_8^0 + f_1^0)(T_{yy} + u_y u_y) = 0, \tag{5.17}$$

$$f_8^0 + f_7^0 - (f_8^0 + f_7^0 + f_4^0)(T_{xx} + u_x u_x) = 0, \tag{5.18}$$

$$f_6^0 + f_7^0 - (f_6^0 + f_7^0 + f_3^0)(T_{yy} + u_y u_y) = 0. \tag{5.19}$$

(5.11)-(5.19) are a completely determined set of equations with the solution

$$\begin{aligned}
f_0^0 &= n(1 - T_{xx} - u_x^2)(1 - T_{yy} - u_y^2), \\
f_1^0 &= n/2(T_{xx} + u_x + u_x^2)(1 - T_{yy} - u_y^2), \\
f_2^0 &= n/2(T_{yy} + u_y + u_y^2)(1 - T_{xx} - u_x^2), \\
f_3^0 &= n/2(T_{xx} - u_x + u_x^2)(1 - T_{yy} - u_y^2), \\
f_4^0 &= n/2(T_{yy} - u_y + u_y^2)(1 - T_{xx} - u_x^2), \\
f_5^0 &= n/4(T_{xy} + T_{xx}T_{yy} + T_{yy}(u_x + u_x^2) + T_{xx}(u_y + u_y^2) + u_x u_y(1 + u_x + u_y + u_x u_y)), \\
f_6^0 &= n/4(-T_{xy} + T_{xx}T_{yy} + T_{yy}(-u_x + u_x^2) + T_{xx}(u_y + u_y^2) - u_x u_y(1 - u_x + u_y - u_x u_y)), \\
f_7^0 &= n/4(T_{xy} + T_{xx}T_{yy} + T_{yy}(-u_x + u_x^2) + T_{xx}(-u_y + u_y^2) + u_x u_y(1 - u_x - u_y + u_x u_y)), \\
f_8^0 &= n/4(-T_{xy} + T_{xx}T_{yy} + T_{yy}(u_x + u_x^2) + T_{xx}(-u_y + u_y^2) - u_x u_y(1 + u_x - u_y - u_x u_y)).
\end{aligned}$$

For this equilibrium distribution we now get

$$\frac{f_5^0 - f_6^0}{f_5^0 + f_2^0 + f_6^0} = u_x + \frac{T_{xy}}{T_{yy} + u_y + u_y^2}, \tag{5.20}$$

which is consistent with the Galilean transformation. The additional term in the velocity is due to the constraint of local momentum conservation so that the mass and momentum transfer have to be coupled.

For a two-component system we need a similar set of extra conditions for the equilibrium distribution of the density difference. The usual conditions are:

$$\sum_i g_i^0 = \sum_i g_i = \varphi \tag{5.21}$$

$$\sum_i g_i^0 v_{i\alpha} = \sum_i g_i v_{i\alpha} = \varphi u_\alpha \tag{5.22}$$

$$\sum_i g_i^0 v_{i\alpha} v_{i\beta} = G\mu(n, \varphi, \nabla\varphi, \nabla^2\varphi)\delta_{\alpha\beta} + \varphi u_\alpha u_\beta. \tag{5.23}$$

They are of the same structure as the equations (5.11,5.12,5.13) if we replace $nT_{\alpha\beta}$ with $G\mu\delta_{\alpha\beta}$. The important difference is that $nT_{\alpha\beta}$ is linear in n where as $G\mu\delta_{\alpha\beta}$ is not linear in φ and in particular can take a finite value for $\varphi = 0$. This means that the equivalent equations for the g_i^0 are singular as $g \to 0$. For a practical scheme we have to avoid these singularities. We can still impose the additional constraints for the velocity

$$\frac{f_1^0 - f_3^0}{f_1^0 + f_0^0 + f_3^0} = u_x, \tag{5.24}$$

$$\frac{f_2^0 - f_4^0}{f_2^0 + f_0^0 + f_4^0} = u_y \tag{5.25}$$

but we have to use a different last constraint to complete the system of equations. Guided by the Orlandini result I impose

$$g_0 = \varphi - \ell G\mu - \varphi(u_x^2 + u_y^2), \tag{5.26}$$

where ℓ is a free parameter that can be used to improve stability (we choose $\ell = 1$). Solving this set of equations for the g_i we get

$$g_0^0 = \varphi - \ell G\mu() - \varphi(u_x^2 + u_y^2), \tag{5.27}$$

$$\begin{aligned}
g_1^0 &= 1/2((\ell-1-u_x)G\mu()+(1+u_x-u_y^2)\varphi u_x), && (5.28)\\
g_2^0 &= 1/2((\ell-1-u_y)G\mu()+(1+u_y-u_x^2)\varphi u_y), && (5.29)\\
g_3^0 &= 1/2((\ell-1+u_x)G\mu()-(1-u_x-u_y^2)\varphi u_x), && (5.30)\\
g_4^0 &= 1/2((\ell-1+u_y)G\mu()-(1-u_y-u_x^2)\varphi u_y), && (5.31)\\
g_5^0 &= 1/4((2-\ell+u_x+u_y)G\mu()+(1+u_x+u_y)\varphi u_x u_y), && (5.32)\\
g_6^0 &= 1/4((2-\ell-u_x+u_y)G\mu()-(1-u_x+u_y)\varphi u_x u_y), && (5.33)\\
g_7^0 &= 1/4((2-\ell-u_x-u_y)G\mu()+(1-u_x-u_y)\varphi u_x u_y), && (5.34)\\
g_8^0 &= 1/4((2-\ell+u_x-u_y)G\mu()-(1+u_x-u_y)\varphi u_x u_y). && (5.35)
\end{aligned}$$

The macroscopic equations determined by the Chapman-Enskog expansion are unaffected by the choice of the further constraints (5.14) to (5.19) and (5.24) to (5.24) or the detailed structure of the equilibrium distributions. Therefore, these alterations in the model can change the stability and the behaviour of quantities like the spurious velocities, but they leave the evolution of the macroscopic quantities unaffected, at least to second order in the derivatives. We only need to take care with the three-velocity moments. With our choice for the $\{f_i\}$ we get for these moments

$$\begin{aligned}
\sum_i f_i^0 v_{ix}^3 &= n u_x,\\
\sum_i f_i^0 v_{ix}^2 v_{iy} &= u_y(P_{xx}+n u_x^2),\\
\sum_i f_i^0 v_{ix} v_{iy}^2 &= u_x(P_{yy}+n u_y^2),\\
\sum_i f_i^0 v_{iy}^3 &= n u_y, && (5.36)
\end{aligned}$$

which reduces to (2.30) for $P_{xx} = P_{yy} = n$ except for the third order terms in the velocities. They cancel with the term in the third order of the velocities in (2.28), which we had to neglect in Chapter 2. Therefore, we recover the Navier-Stokes equations as well for $P = n$ or, using (2.36), $T = 1$.

5.2 Measures for non-isotropic patterns

To measure the features of phase separation under shear it is necessary to construct measures to characterise the anisotropy of the sheared systems. Let us consider which of the measures introduced in Section 3.2.1 can be generalized to give information about non-isotropic patterns. All measures that are based on Fourier Transforms cannot be easily used for sheared systems because the system is no longer periodic. In the case of a Klein-Bottle topology, the lattice can be duplicated to construct a periodic lattice, but the symmetry of this double system prevents the determination of the orientation of the pattern.

Measures derived from derivatives do not, however, suffer from this problem. Derivatives need to be evaluated for the algorithm and are readily available. We can define a tensor that will allow us to extract two length scales and an angle from the expression (compare (3.7))

$$d_{\alpha\beta} = \frac{\sum_{\mathbf{x}} \partial_\alpha^D \varphi(\mathbf{x},t) \partial_\beta^D \varphi(\mathbf{x},t)}{\sum_{\mathbf{x}} \varphi^2(\mathbf{x},t)}, \tag{5.37}$$

where ∂_α^D is the symmetric discrete derivative in direction α. Because the matrix is symmetric it can be diagonalised to give two eigenvalues λ_1, λ_2 and an angle

$\theta^\star$:

$$\lambda_1 = \frac{d_{xx} + d_{yy}}{2} + \sqrt{\frac{(d_{xx} - d_{yy})^2}{4} + d_{xy}^2} \tag{5.38}$$

$$\lambda_2 = \frac{d_{xx} + d_{yy}}{2} + \sqrt{\frac{(d_{xx} - d_{yy})^2}{4} + d_{xy}^2} \tag{5.39}$$

$$\theta^\star = \tan^{-1}\left(\frac{d_{yy}}{d_{xy} - \lambda_2}\right). \tag{5.40}$$

The two eigenvalues give us two orthogonal length scales

$$R_1^\star(t) = \frac{L_w}{\lambda_1(t)} \tag{5.41}$$

$$R_2^\star(t) = \frac{L_w}{\lambda_2(t)}, \tag{5.42}$$

where L_w is the interface width (see detailed discussion of the effect of the interface width in Section 3.2.1). L_w could in principle be anisotropic. That this is not a strong effect can be seen by comparing these length scales with length scales that are explicitly independent of the interface width. One such measure is introduced in the next paragraph. The comparison (see *e.g.* Figures 5.4 and 5.6) shows very little deviation of the two measures.

We can generalize the measure connected to the length of the interface to a non-isotropic measure. The interface can be represented by a set of contours. These contours consist of small line segments $\vec{l}_i$. So the length of the interface is

$$L_I = \sum_i |\vec{l}_i|. \tag{5.43}$$

In order to extract the preferred direction of the interface we define the vector

$$\vec{D} = R^{-1}\left(\sum_i R(\vec{l}_i)\right) \tag{5.44}$$

where

$$R(\vec{x}) = |\vec{x}| \begin{pmatrix} \cos(2\theta) \\ \sin(2\theta) \end{pmatrix} \tag{5.45}$$

and

$$\theta^\circ = \cos^{-1}\left(\frac{\vec{1}_x.\vec{x}}{|\vec{x}|}\right), \tag{5.46}$$

i.e., the vector is rotated to have twice the angle with the x-axis.

The quantity $\vec{D}$ is a vector that is zero for isotropic objects and points in the averaged direction of their interface for non-symmetric objects. One can define two length scales and an angle from these measures that correspond to the intuitive result for oriented rectangular objects. We define

$$\begin{aligned} R_1^\circ &= \frac{L_x L_y}{L_I + |\vec{D}|} && (5.47) \\ R_2^\circ &= \frac{L_x L_y}{L_I - |\vec{D}|} && (5.48) \\ \theta &= \cos^{-1}\left(\frac{\vec{1}_x.\vec{D}}{|\vec{D}|}\right). && (5.49) \end{aligned}$$

So now we have two independent measures for the structure of non-isotropic patterns that we will use to examine the spinodal decomposition under shear.

5.3 Simulation results

Shear flow applied to a system undergoing spinodal decomposition stretches the original pattern. This effect is only relevant if the deformation caused by the flow is of the same order or larger than the deformation caused by the coarsening

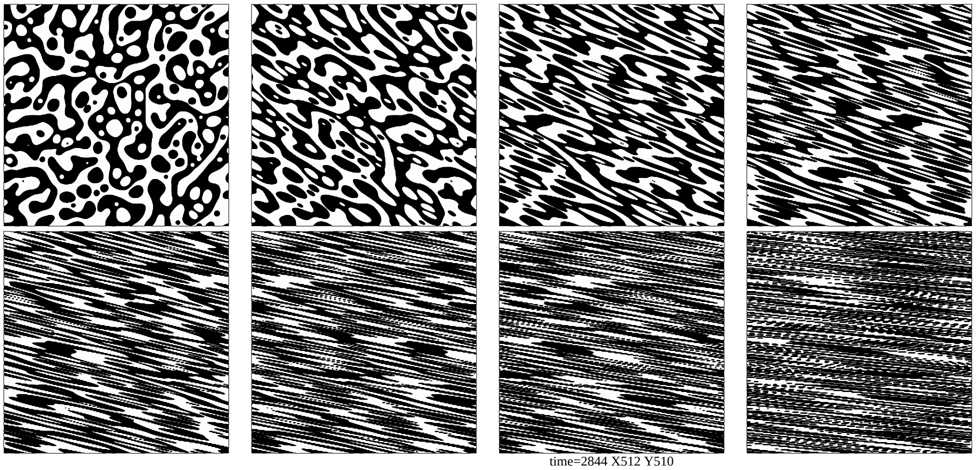

Figure 5.2: Shear without internal dynamics with shear rate $\dot{\gamma} = 1$ for times $t = 0, 1, 2, 3, 4, 5, 6$ and10.

process. This requires

$$\dot{\gamma} t > 1. \tag{5.50}$$

We therefore expect that we can observe the effect of the shear flow for $t > 1/\dot{\gamma}$.

To understand the effect of shear-flow on a phase separating system let us first consider a pattern without any internal dynamic that undergoes a shear transformation. The shear transformation is defined as

$$\begin{pmatrix} x \\ y \end{pmatrix} = \begin{pmatrix} x + \dot{\gamma} t y \\ y \end{pmatrix}, \tag{5.51}$$

and describes the effect of a simple shear flow on a system. The effect of this transformation is illustrated in Figure 5.2 where we start with a spinodal decomposition pattern and show successive iterations of the shear transformation with $\dot{\gamma} = 1$. The structure develops an orientation that slowly aligns with the shear

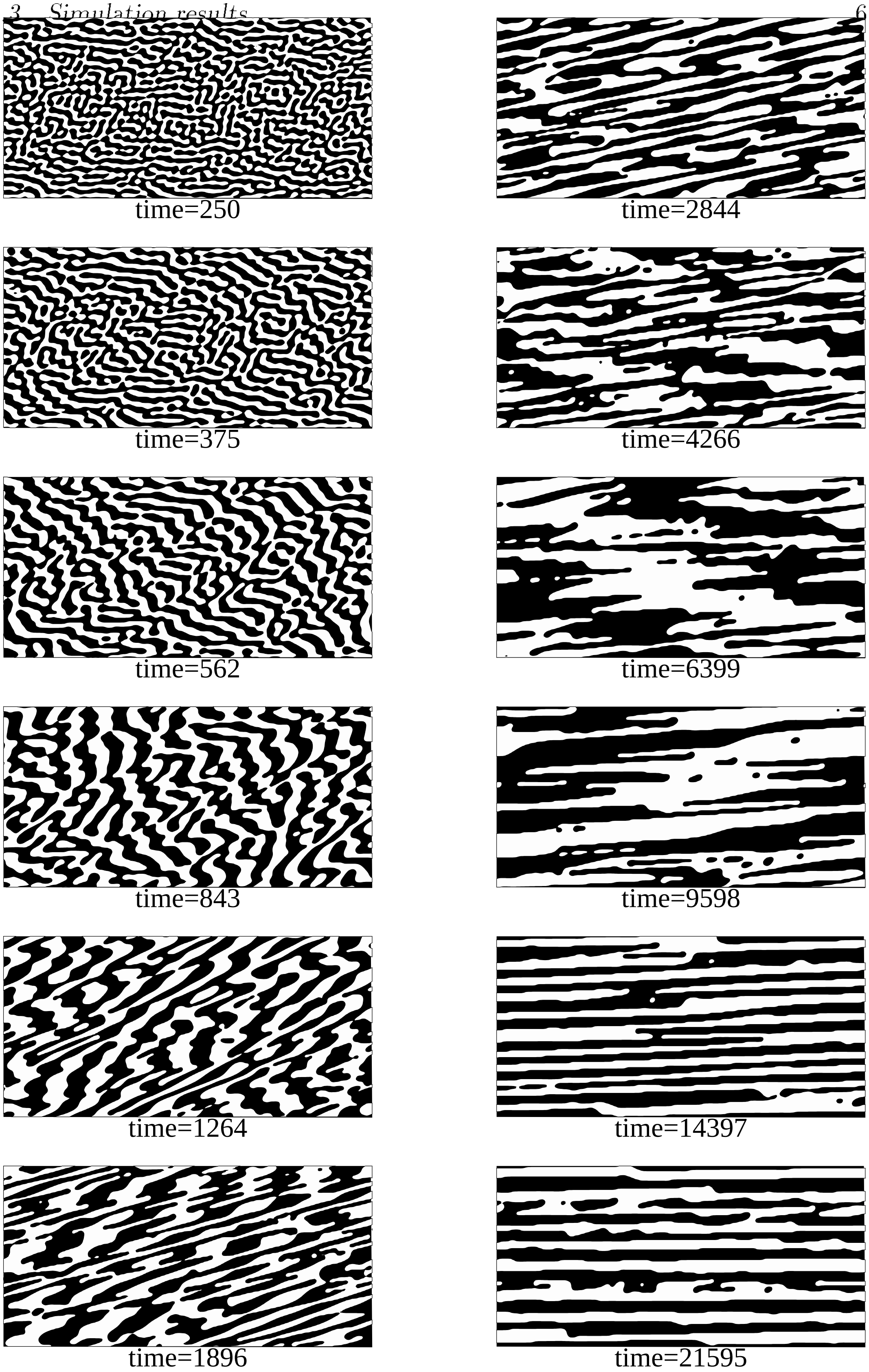

time=250

time=375

time=562

time=843

time=1264

time=1896

time=2844

time=4266

time=6399

time=9598

time=14397

time=21595

Figure 5.3: High viscosity spinodal decomposition pattern in a strongly sheared system ($\dot{\gamma} = 0.004, L_x = 256, L_y = 128, \tau_f = 100$, other parameters as in Figure 3.8).

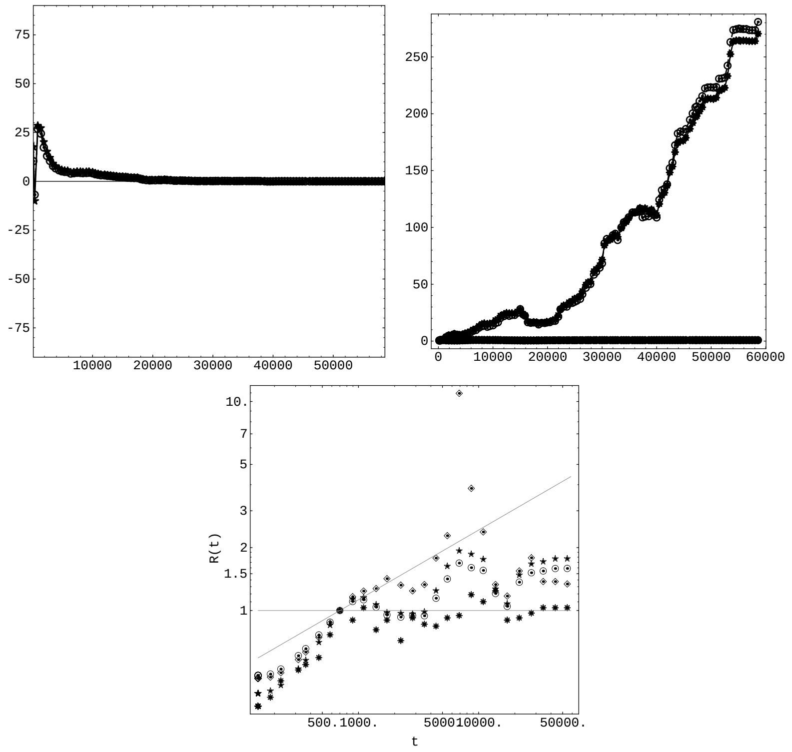

Figure 5.4: Angle θ, length scales $R^{\star}_{1,2}$ ($\star$), $R^{\circ}_{1,2}$ ($\circ$) and the scaling graph of length R° ($\circ$), R^{1} ($\diamond$), $R^{\star}$ ($\star$) and $R^{\#}$ in a strongly sheared system ($\dot{\gamma} = 0.004, L_x = 256, L_y = 128, \tau_f = 100$, other parameters as in Figure 3.8).

direction while the stretching increases the length of the structure and decreases its width. Once the width of the domains is smaller than the original width of the interface the system is effectively a homogeneous mixture.

This effect is known as shear-induced mixing and can be observed in our system if the stretching effect of the shear flow is much faster than the growth of the domains via diffusion. Numerically this can be achieved by choosing a very low mobility Γ. Phase separation is now suppressed because of the mixing properties of the shear flow unless the phase separating structure is aligned with the shear direction. For finite lattices we observe at much later times a nucleation of complete stripes that span the system and are periodic in the shear direction. The time required to form these stripes depends on the system size and it seems reasonable to assume that this phenomenon does not occur in infinite systems. It has been described as a shift in the effective critical temperature $T_c^{eff}(\dot{\gamma})$[39, 11].

We now consider systems with hydrodynamic and diffusive modes. The internal dynamics that lead to domain coarsening can also prevent a complete mixing of the system. Figure 5.3 shows the spinodal decomposition pattern of a high-viscosity binary mixture. The internal hydrodynamic degrees of freedom can be neglected in comparison with the diffusive dynamics. For very short times ($t < 300$) we observe the familiar spinodal decomposition pattern. It is, however, coarsening in a new way via shear flow-induced collisions of the domains. This process enhances domains oriented in the collision direction. Then for $300 < t < 1000$ the flow slowly turns the striped pattern and stretches it. For $t \sim 1000$ the rupturing of domains starts to be important and for $1000 < 15000$ there is a continuous stretching and rupturing that effectively stops the phase ordering process. For $t > 15000$ the system has developed stripes that span the system. Because periodic stripes are unaffected by the shear flow if they are completely aligned the system can now grow via the diffusion mechanism.

This evolution can be followed more quantitatively by measuring the orientation angle θ and the non-isotropic length scales shown in Figure 5.4. The first

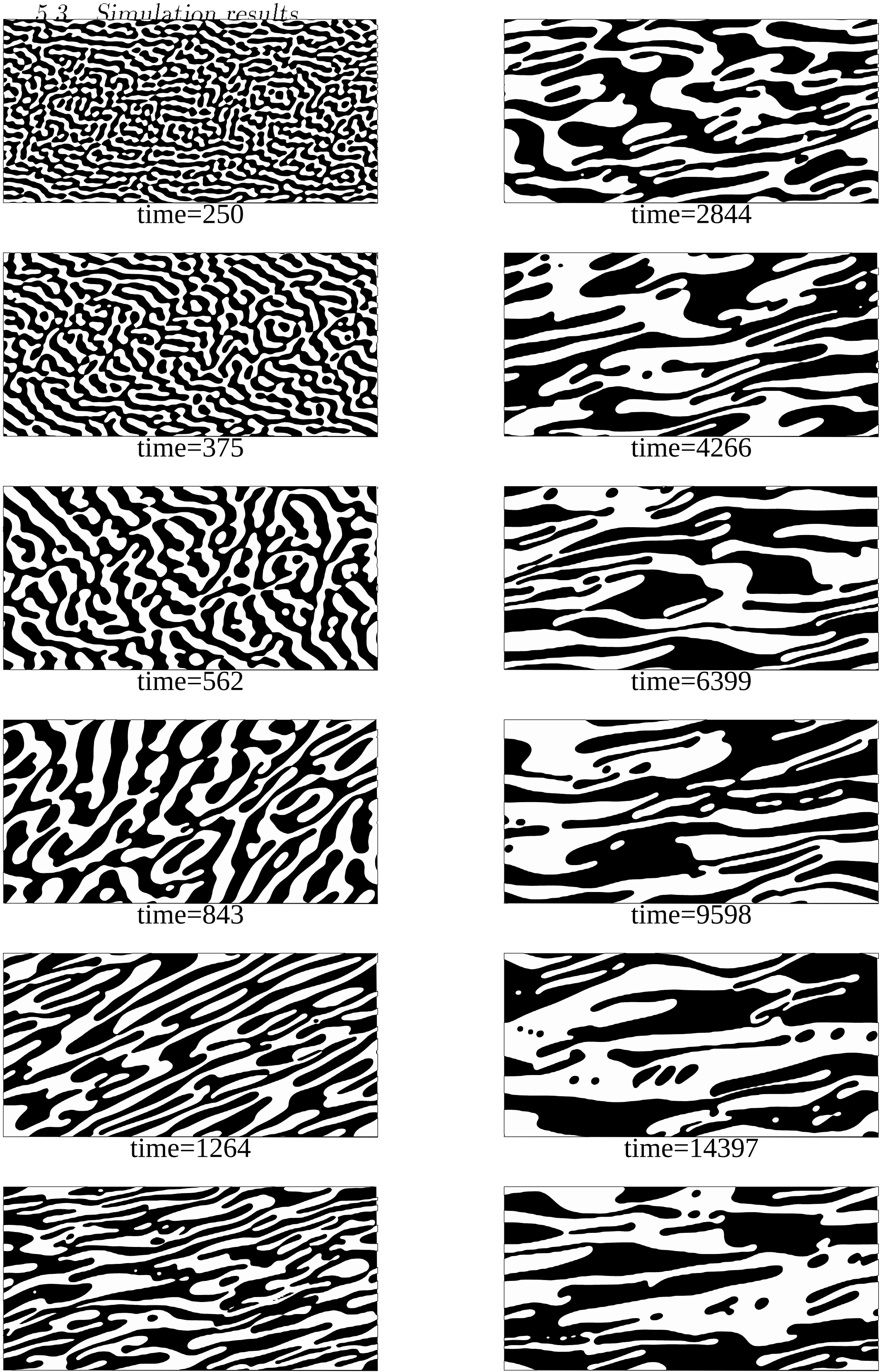

time=250

time=375

time=562

time=843

time=1264

time=1896

time=2844

time=4266

time=6399

time=9598

time=14397

time=21595

Figure 5.5: Intermediate viscosity spinodal decomposition pattern in a strongly sheared system ($\dot{\gamma} = 0.004, L_x = 256, L_y = 128, \tau_f = 1$, other parameters as in Figure 5.3).

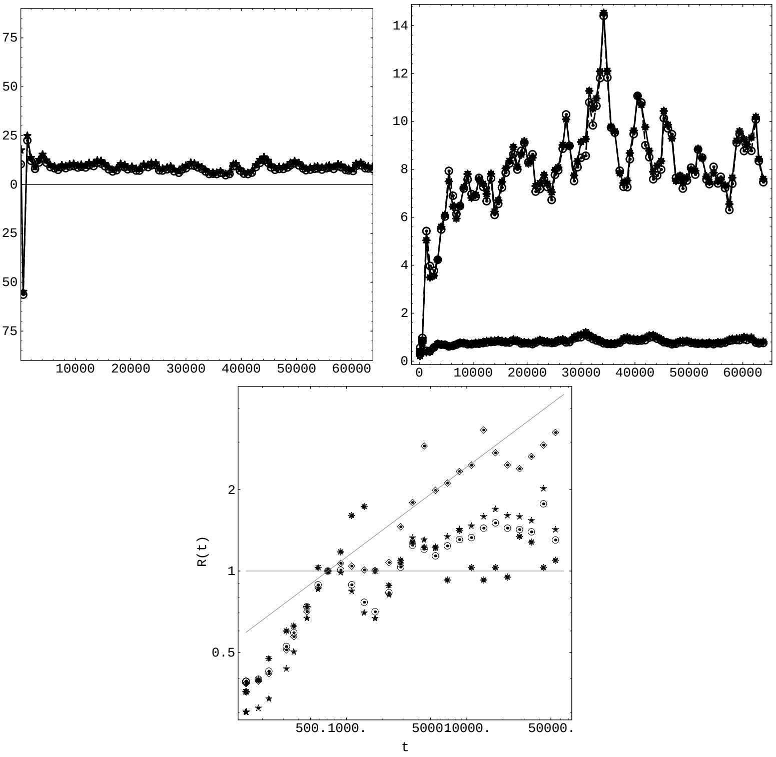

Figure 5.6: Angle, length scales $R^{\star}_{1,2}$ ($\star$), $R^{\circ}_{1,2}$ ($\circ$) and the scaling graph of length R° ($\circ$), R^{1} ($\diamond$), $R^{\star}$ ($\star$),and $R^{\#}$ in a strongly sheared system ($\dot{\gamma} = 0.004, L_x = 256, L_y = 128, \tau_f = 1$, other parameters as in Figure 3.8).

figure shows the angle as measured by $\theta^{\star}$ (eqn. 5.40) and θ° (eqn. 5.49). We see that the two different measures for the orientation agree very well. The angle oscillates at very early times ($t < 2000$) and then slowly aligns with the direction of the shear flow as periodic stripes are created.

The second graph in Figure 5.6 shows the length-scales $R^{\star}_{1,2}$ defined in equations (5.41,5.42) and the length scales $R^{\circ}_{1,2}$ defined in equations (5.47,5.48). We very clearly see a separation of length scales and a good agreement of the two different measures. A minimum of the larger length scale at $t \sim 17000$ indicates the creation of periodic stripes stretching the system. After this time the growth of domains is no longer hindered by the continual breaking of stretched domains.

The third graph shows the scaling of the circularly averaged measures of length that we used to characterise spinodal decomposition patterns in the isotropic case in Chapter 3 (equations (3.5,3.8,3.9)) which can be compared to the results for isotropic phase separation (see Fig. 3.4, 3.7 and 3.10). We see that all the measures indicate a freezing in the domain growth. The measure R^1 is special in that it shows a clear peak at $t \sim 7000$ where there is an ordering of domains orthogonal to the direction of the shear. This feature only occurs in the R^1 measure because the interface, important for measures R° and $R^\star$, is not straight and the number of domains, used to calculate $R^\#$, is unaffected. The behaviour of R° and $R^\star$ is dominated by the small length scale because

$$R^\circ = \frac{2}{\frac{1}{R_1^\circ} + \frac{1}{R_2^\circ}} \qquad (5.52)$$

$$R^\star = \frac{2}{\frac{1}{R_1^\star} + \frac{1}{R_2^\star}}, \qquad (5.53)$$

so that the long-range order of the pattern is not detectable in the scaling plot of the isotropic length scales.

Let us now consider a system with a lower viscosity that allows for a hydrodynamic response of the domains to the shear flow. In Figure 5.5 we see a system with an intermediate viscosity in the sense introduced in Chapter 3. It is immediately obvious that the pattern differs from that in Figure 5.3. The final state

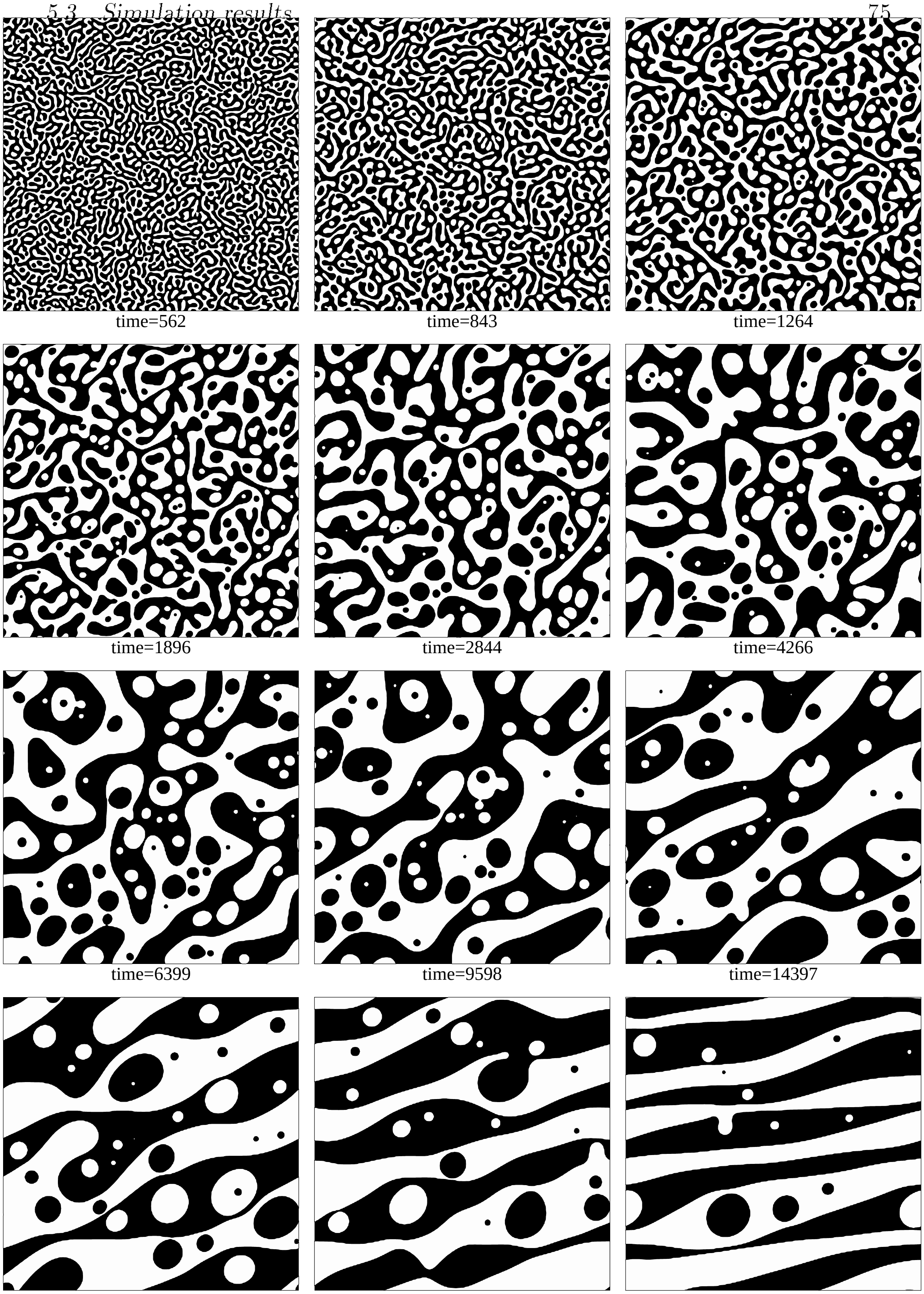

time=562
time=843
time=1264
time=1896
time=2844
time=4266
time=6399
time=9598
time=14397
time=21595
time=32392
time=48588

Figure 5.7: Intermediate viscosity spinodal decomposition pattern in a weakly sheared system ($\dot{\gamma} = 0.0001, L_x = L_y = 512, \tau_f = 0.8$, other parameters as in Figure 3.8) The shear flow is relevant for $t > 1/\dot{\gamma} = 10000$.

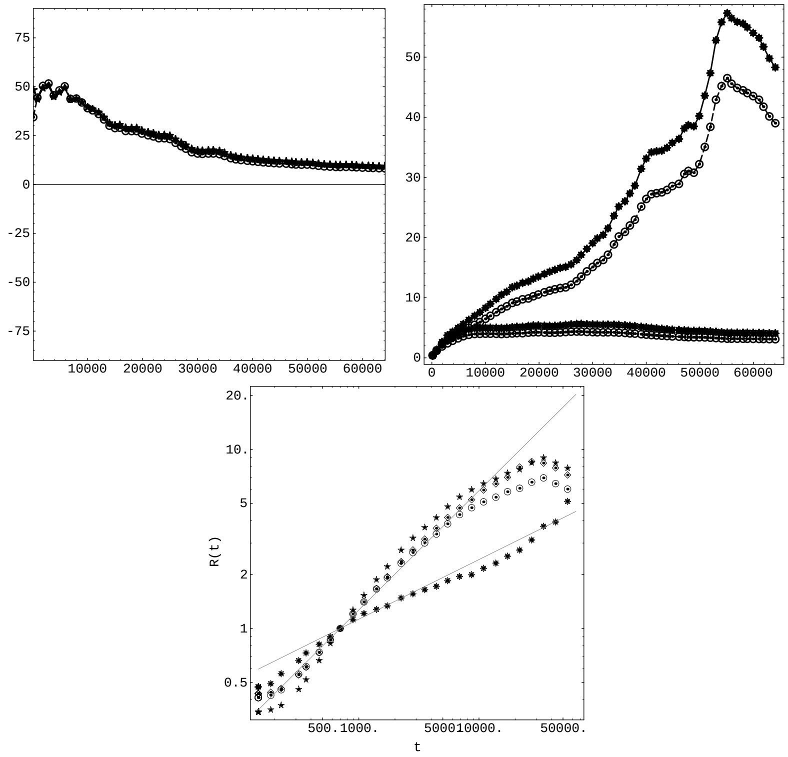

Figure 5.8: Angle, length scales $R^{\star}_{1,2}$ ($\star$), $R^{\circ}_{1,2}$ ($\circ$) and the scaling graph of length R° ($\circ$), R^{1} ($\diamond$), $R^{\star}$ ($\star$),and $R^{\#}$ in a weakly sheared system ($\dot{\gamma} = 0.0001, L_x = L_y = 512, \tau_f =$ 0.8, other parameters as in Figure 3.8).

does not simply consist of periodic stripes, but dynamic structures that are constantly stretched, broken and deformed by the flow so that the phase separation "freezes" in this complex dynamic state.

The quantitative measures in Figure 5.6 show that after the early rotation of the orientation of the system the pattern converges to a slightly fluctuating orientation that is a finite angle to the shear direction. This phenomenon is similar

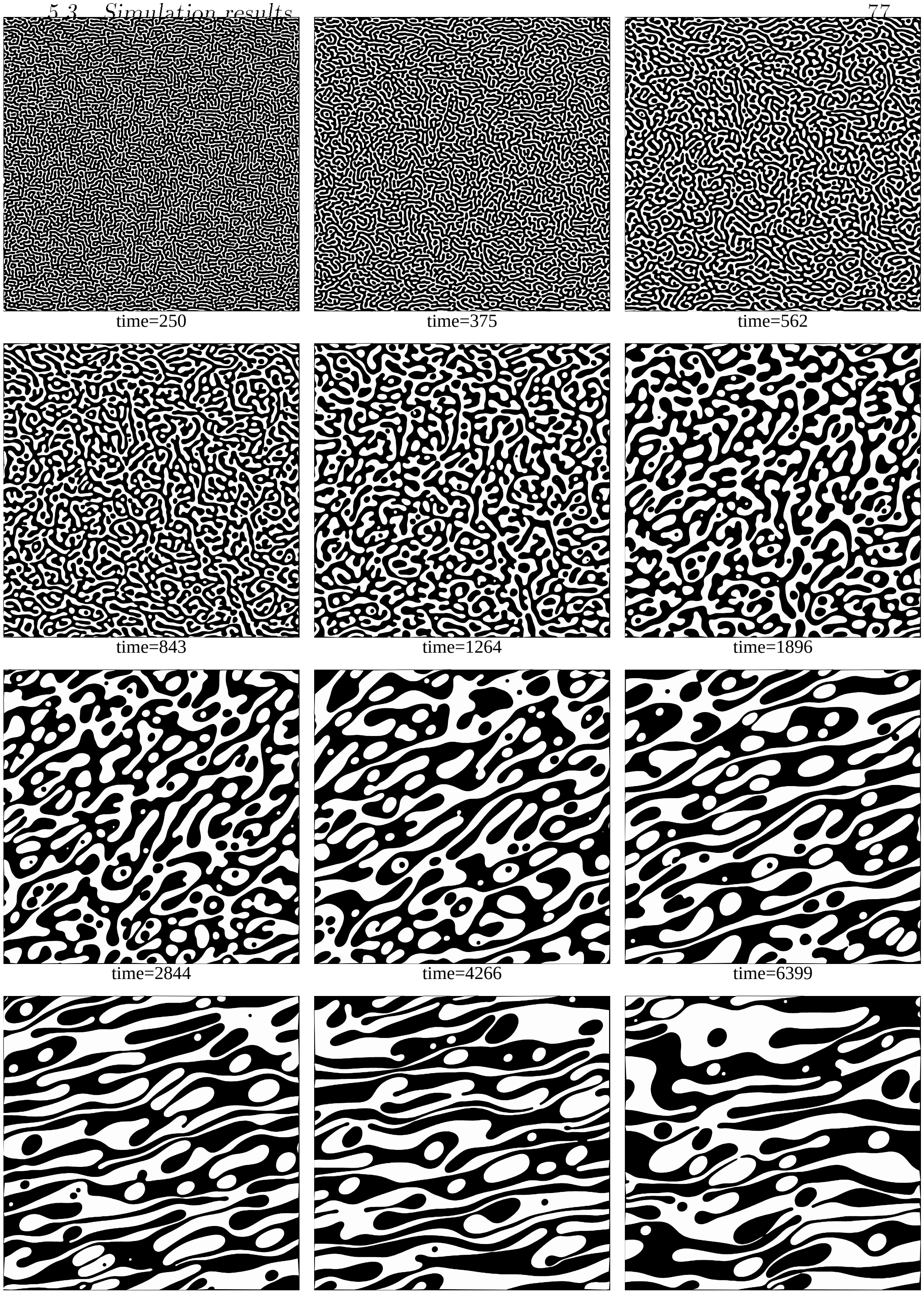

time=250 time=375 time=562

time=843 time=1264 time=1896

time=2844 time=4266 time=6399

time=9598 time=14397 time=21595

Figure 5.9: Spinodal decomposition pattern in a sheared system ($\dot{\gamma} = 0.0005, \tau_f = 1, L_x = L_y = 512$, other parameters as in Figure 3.8). The shear flow becomes relevant for time $t > 1/\dot{\gamma} = 2000$.

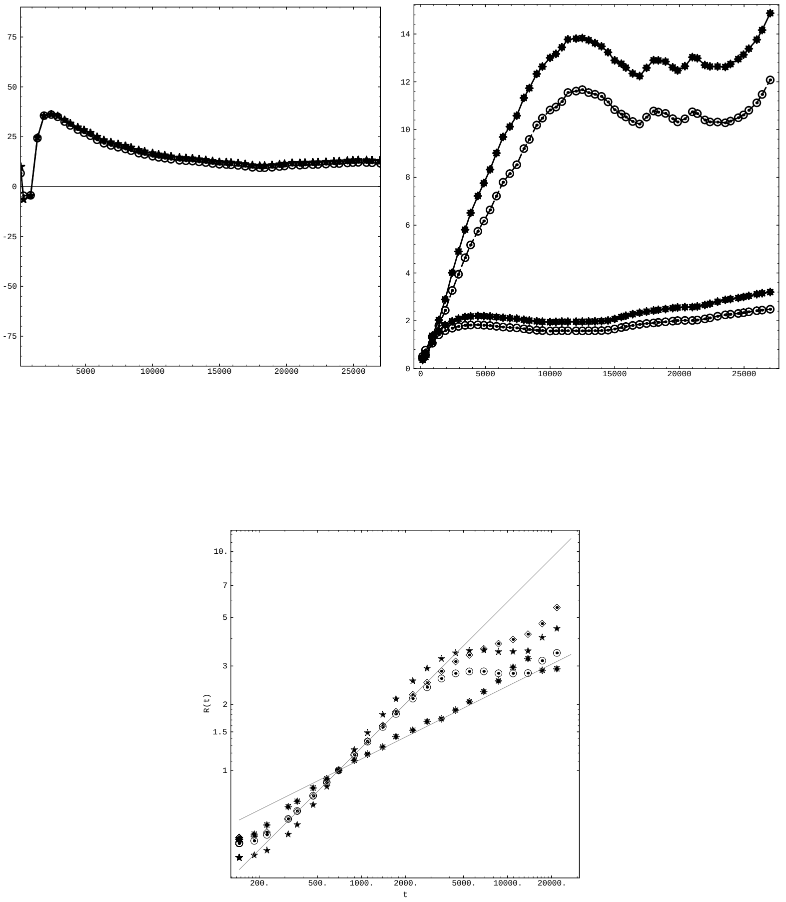

Figure 5.10: Angle, length scales $R^{\star}_{1,2}$, $R^{\circ}_{1,2}$ and the scaling graph of length $R^{\circ}, R^{1}, R^{\star}, and R^{\#}$ in a sheared system ($\dot{\gamma} = 0.0005, L_x = L_y = 512, \tau_f = 1$, other parameters as in Figure 3.8).

to the behaviour of a single drop in a shear flow that forms a finite angle to the shear flow (see Chapter 6). In the graph of the non-isotropic length scales we can again see the very clear distinction between the large and small length scales. Because of the irregular structure of the pattern and the fact that the system is so small that only a few domains are contained in the system the length-scales oscillate strongly. The data suggest strongly that a state of dynamic equilibrium is reached where the typical domain size remains constant.

The scaling graph in Figure 5.6 also shows that the growth process is stopped. Two small peaks in the R^1 measure indicate intermediate states of higher spatial order, similar to the peak in the scaling graph of Figure 5.4.

We have, so far, considered strong shear flow. Let us now consider an example where the shear flow is so small that the early time spinodal decomposition is unaffected by the flow. In accordance with equation (5.50) we define early times as $t < 1/\dot{\gamma}$. In Figure 5.7 the spinodal decomposition under a shear with shear rate $\dot{\gamma} = 0.0001$ is shown for a system with intermediate viscosity. For times $t < 1/\dot{\gamma} = 10000$ we see the typical spinodal decomposition pattern for intermediate viscosity as described in Section 3.3 (see Figure 3.8). After this time the stretching of the domains dominates over the isotropic domain growth and the pattern becomes non-isotropic. By $t \sim 10000$ the pattern comprises large-stripe like domains together with the nested pattern of drops within drops in the large domains (compare also Figure 3.8 for the result without shear flow). As the large domains are stretched the drops inside them coalesce with the walls of the domains and slowly the stripes are cleaned of the small included drops.

These results also clearly show up in the measurements given in Figure 5.8. After $t > 10000$ the orientation slowly converges towards a tilting angle $\theta \sim 7°$, the long and short length scales split and the $R^{\star} \sim R^{\circ} \sim R^{1} \sim t^{\frac{2}{3}}$ growth law breaks down. In the $R^{\#}$ measure derived from the number of domains we see a slight increase from the normal growth law corresponding to the process of shear cleaning the stripes from drops.

At a higher shear $\dot{\gamma} = 0.0005$ the shear flow becomes important at the earlier time $t = 1/\dot{\gamma} = 2000$, and because the phase separation process is not scale invariant there are less small domains in the large structures. It might be possible, however, that the shear pattern recovers a scale invariant structure where the length scale is related to the shear rate. In order to address this question, simulations on a larger lattice will be necessary. The technical problems related to this are discussed in Section 5.5.

5.4 Instability of stripes

In 1995 Hashimoto *et al.* [23] observed experimentally that phase-separating fluids under shear can form a string phase. In this phase the shear flow stabilizes the strings against their intrinsic surface tension instabilities. For the numerical simulation of spinodal decomposition under shear in two dimensions one can often observe the spontaneous formation of stripes, which are similar to the string phase in three dimensions. In this section we show that in our simulations shear flow can indeed stabilize the striped pattern, and comment on the observed dynamics

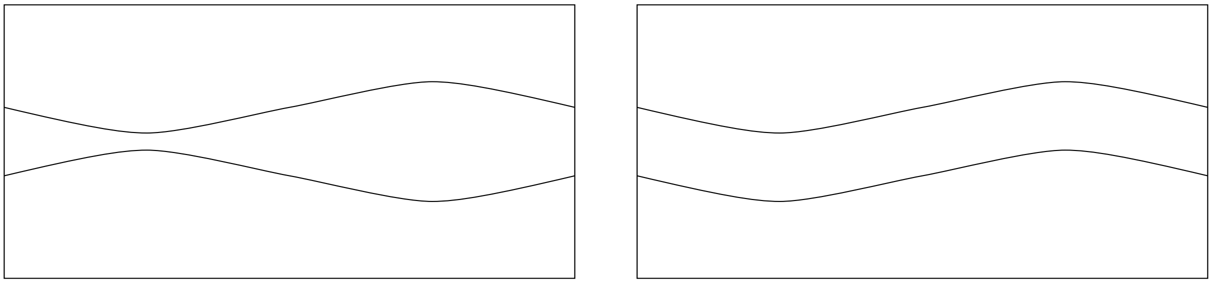

Figure 5.11: The necking instability transformed by shear flow to the stable zig-zag mode.

of striped pattern in spinodal decomposition under shear.

In the numerical simulation of spinodal decomposition under shear one often observes the spontaneous formation of stripes. These stripes can then become unstable to oscillations and coalesce. This may lead to a formation of fewer, but wider, stripes that are stable. This phenomenon has not only been seen in our lattice Boltzmann simulations, but also in lattice gas simulations of binary mixtures [9]. In order to understand this phenomenon we need to explain why a stripe can be unstable, and given that it is unstable, why it can form in the first place.

The instability of stripes in two dimensions may seem surprising since the surface tension always tends to straighten deformed interfaces and a shear flow along the stripes should not lead to an instability orthogonal to this direction. In order to explain the instability it is important to keep in mind that our interfaces are extended and attract each other. The interaction is strong only for stripes not much wider than the interface width.

The stability of one stripe in a binary mixture under shear flow has been investigated analytically by Frischknecht [15]. The result of her analysis is that shear flow tends to stabilize a single stripe. The attraction of the interfaces tends to produce necks where the stripe breaks. In the presence of shear the two sides of the neck are displaced by the flow so that the neck instability is transformed to the stable zig-zag mode. This is shown schematically in Figure 5.11. In [15] Frischknecht proved that a single domain will become stable in a large enough shear flow.

In the presence of more than one stripe the situation is much more complicated because the stripes interact via the flow field. An example of unstable stripes is shown in Figure 5.12. We initialised the system with eight stripes of the A and B rich phases. We also set up a flow field with small random disturbances to act as a seed for the instability. We observed both necking and zig-zag deformations of stripes because a necking instability in one stripe deforms the neighbouring stripes in a zig-zag mode.

We then examined the effect of shear flow on the stripes. For a shear rate of $\dot{\gamma} = 0.001$ we observed a slower growth of the perturbations of the striped pattern as shown in Figure 5.13. At a larger shear rate $\dot{\gamma} = 0.005$ the growth of perturbations is slowed down even more, so that the first breaking of domains only occurs after 10000 time steps. A pattern of multiple stripes, however, is never stable at very late times. This is because of the very slow effect that smaller stripes shrink at the cost of larger stripes (similar to the Oswald ripening of drops) and, the smaller a stripe, the stronger the necking instability becomes. This ultimately leads to the instability of the small stripes.

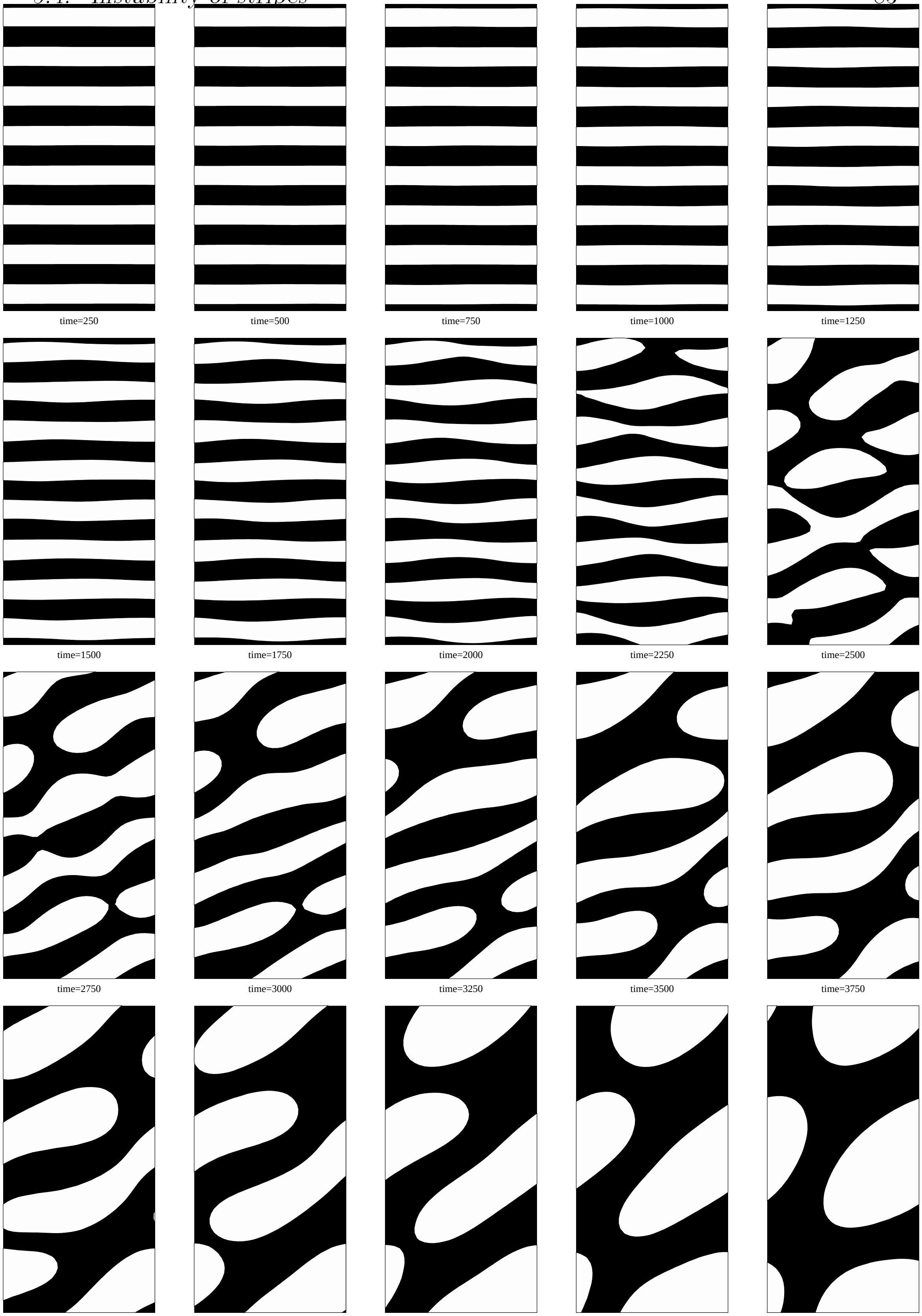

time=250 time=500 time=750 time=1000 time=1250

time=1500 time=1750 time=2000 time=2250 time=2500

time=2750 time=3000 time=3250 time=3500 time=3750

time=4000 time=4250 time=4500 time=4750 time=5000

Figure 5.12: A striped system without shear shows an instability. This simulation is for a system with $\dot{\gamma} = 0, \Gamma = 0.8, \tau_f = 1, L_x = 32, L_y = 64$.

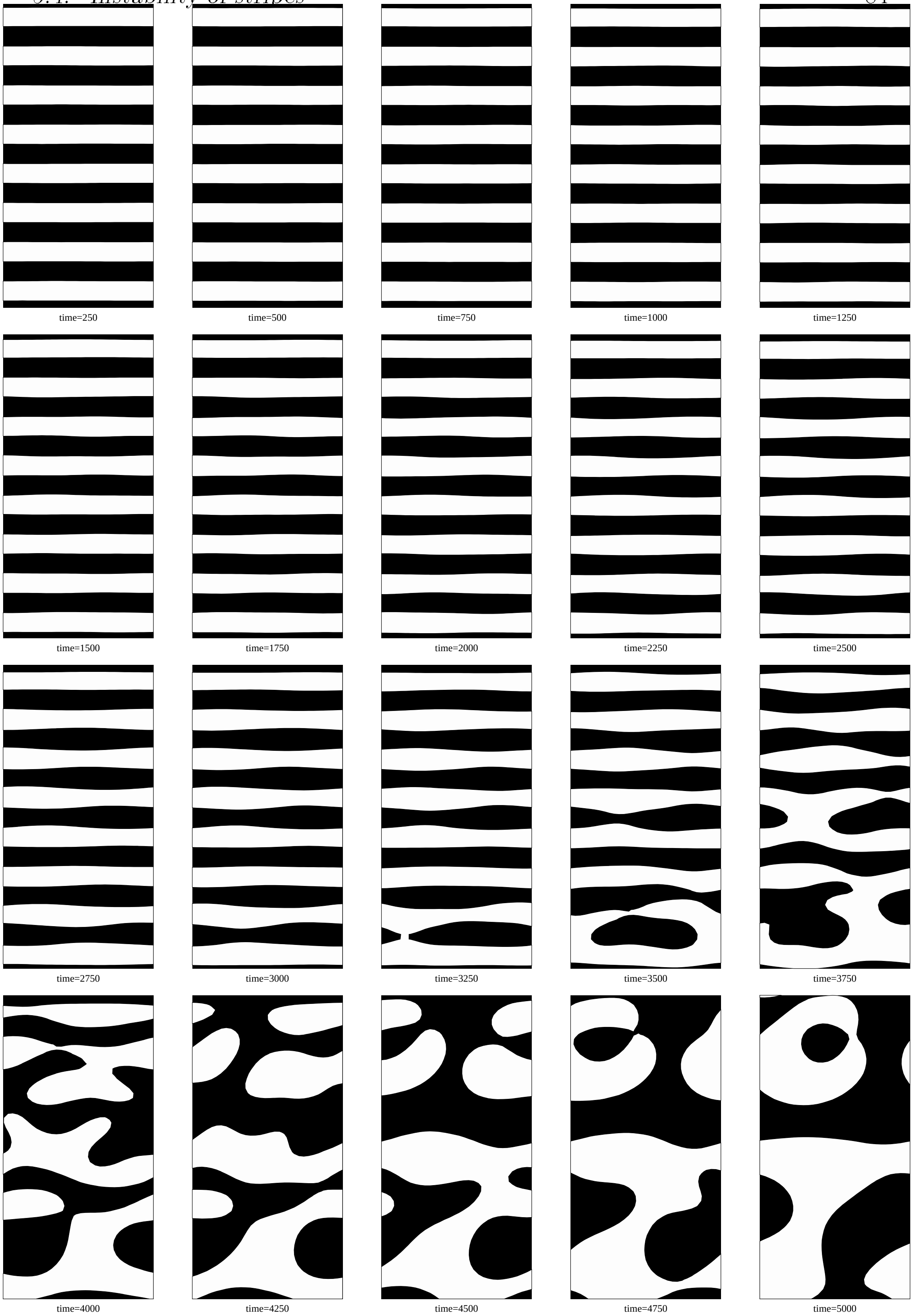

time=250 time=500 time=750 time=1000 time=1250

time=1500 time=1750 time=2000 time=2250 time=2500

time=2750 time=3000 time=3250 time=3500 time=3750

time=4000 time=4250 time=4500 time=4750 time=5000

Figure 5.13: A striped system with shear is more unstable. This simulation is done for a system with $\dot{\gamma} = 0.001, \Gamma = 0.8, \tau_f = 1, L_x = 32, L_y = 64$.

This leaves us with the question of how stripes can be formed in a shear flow if they are unstable. The formation of the stripes occurs at a time when the phase separation is not completed or when domains have been partly dissolved by the shear flow. The formation of stripes is favoured by strong shear flow. Also, the stripes are stabilised against fluctuations and break up by the shear-induced stability discussed above. This often results in the formation of a striped pattern in the early stages where the A and B rich phases are still far from the bulk equilibrium values. The phase separation process, however, increases the A and B concentrations in the A and B rich stripes, respectively, and the interface grows. This also increases the attraction of the interfaces, and the striped pattern becomes unstable.

5.5 Conclusions

In this chapter we have investigated the effects of shear flow on systems undergoing spinodal decomposition. In order to study these systems we introduced an extension to the algorithm that allows us to simulate shear flow problems with Lees Edwards boundary conditions. We find that the effect of shear flow on spinodal decomposition depends strongly on the viscosity of the fluid. Systems with a very high viscosity tend to order in the shear directions, whereas systems with an intermediate viscosity arrive at a dynamic stationary state where the domains lie at a finite angle to the shear direction. We showed that the predicted and experimentally observed stabilization of striped structures by shear flow can be observed in our numerical simulations.

There remain many unexplored problems concerning the structure of decomposition under shear. It is interesting to investigate the transition between the sheared and non-sheared patterns for different viscosities. What is the effect if shear is only applied for some initial time? Are late-time decomposition patterns statistically independent of an initial shear?

One of the problems with the simulations of spinodal decomposition under shear is that the maximum possible shear rate is limited by the system size because the lattice Boltzmann scheme imposes a maximum velocity. On the other hand the shear flow induces long range correlations much faster than is the case for un-sheared systems so that larger lattice sizes are required to examine long-time behaviour. A possible solution of the problem of seemingly exclusive high shear rates and large lattices may be to cut the lattice into slices in the x-direction so that their width in the y-direction L_y is small, so that $L_y\dot{\gamma} \ll 1$. In the most extreme case one cut could be included for all lines orthogonal to the y-direction. We note that this procedure could also be generalized for all plane flows, for example the flow profile through a pipe, so that the velocities simulated are only the deviations from some defined flow like a linear or parabolic flow. The introduction of this generalized lattice removes the usual restrictions of a maximum velocity.

Chapter 6

Break-up and dissolving of drops under shear

In this chapter we use a lattice Boltzmann simulation to examine the effects of shear flow on a single equilibrium droplet in a phase separated binary mixture. We find that large drops break up as the shear is increased but small drops dissolve. We also show how the tip-streaming, observed for deformed drops, leads to a state of dynamic equilibrium.

To understand the basic phenomena underlying this complex process we focus our attention on the behaviour of a single equilibrium droplet in a two-dimensional binary fluid under shear flow. Despite the simplicity of the model system it shows rich behavior, both droplet break-up and droplet dissolution. We also suggest a new explanation of tip streaming observed in our simulations.

Consider first an immiscible drop subjected to a shear flow. This problem has been studied extensively since the original experiments by Taylor [62]. Experimental, theoretical and numerical results are available in three dimensions [45, 56, 46] and theoretical [48, 5] and numerical [21, 22] results in two dimensions. These approaches consider drops with a singular interface and a conserved volume. The drops are deformed by the shear flow while maintaining their volume. If the shear rate exceeds a certain critical value, which depends on the volume of the drop, the drop will break up. Conversely, for a given shear rate, there exists a volume above which the drop is unstable. We shall denote this volume V_b.

For a partially miscible binary mixture a similar break-up of droplets is observed if the droplets are large. There is now, however, a second volume scale V_d which sets a *lower* limit to the drop size. V_d corresponds to the minimum size of a nucleation seed. The reason for the existence of a lower limit of the drop size lies in the free energy balance between the favourable creation of separate phases in the super-saturated mixture and the unfavourable creation of the interface separating them. Note that, because when a shear is applied a drop deforms and increases its surface length, V_d will depend on the shear rate. For shear rates with $V_b < V_d$ there are no stable drops in the system.

In the next Section of the chapter we describe the extensions to the free energy lattice Boltzmann approach, described in Chapter 2 needed to treat shear flow. Results for the break-up of a large droplet are presented in Section 6.2. In Section 6.3 we obtain an estimate for the volume V_d below which small droplets dissolve and discuss the effect of shear flow on the dissolution. Section 6.4 discusses tip streaming, the loss of material from the tips of the deformed droplet and summarizes the results of the chapter.

6.1 Method

We consider a linear shear flow with velocity

$$\begin{pmatrix} u_x \\ u_y \end{pmatrix} = \begin{pmatrix} Gy \\ 0 \end{pmatrix} \tag{6.1}$$

where G is the shear rate. If the fluid is homogeneous it is expected that equation (6.1) describes the velocity field of the whole fluid. Inserting a droplet will disturb the velocity field locally but equation (6.1) gives the far field solution.

To simulate the shear it is necessary to introduce boundary conditions[1] that force the flow. After each streaming step we replace the collision step at the boundary by a step that defines the variables of the lattice Boltzmann scheme to take values that correspond to the required value of the velocity and densities.

Two different kinds of boundary conditions have been implemented:

periodic: The top and bottom edges of the lattice at $y = \pm y_b$ are the boundaries and the velocity is constrained to be $\mathbf{u} = (\dot{\gamma} y, 0)$. The side boundaries have periodic boundary conditions. This corresponds to a shear confined by two moving walls acting on a periodic array of drops.

---

[1] It is, of course, possible to use the Lees-Edwards' boundary conditions for lattice Boltzmann developed in the last section. Since we are not interested in the effects at the wall, however, it is algorithmically simpler to impose flow at the boundaries.

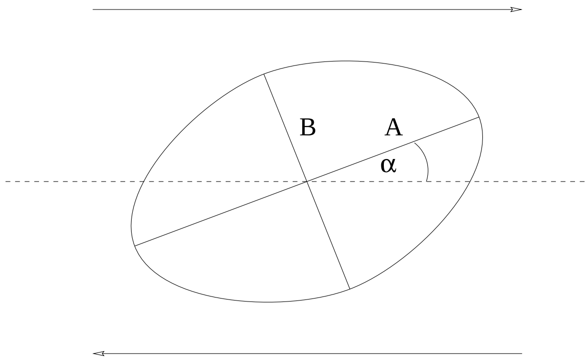

Figure 6.1: Sketch of a deformed drop in a simple shear flow. For small shear rates the drop has the form of an ellipse with axes 2A and 2B. The ellipse is inclined to the direction of the shear flow by a shear strength dependent angle α.

forced: All the edges of the lattice are forced to have $\mathbf{u} = (\dot{\gamma} y, 0)$. This eliminates the effects of periodic images of the drop. The local values of n and φ are replaced by their mean value averaged over the boundary. These boundary conditions generalize for more complicated forced flows, for example, hyperbolic shear flow.

For a homogeneous system both boundary conditions lead to the velocity profile of equation (6.1) to within machine accuracy. In the presence of a drop both boundary conditions are expected to give the same results for an infinite lattice. A comparison of the two different boundary conditions, therefore, gives a measure of the effect of the periodic images on the drop.

If a drop is placed in a shear flow it will be deformed by the forces acting on it. The drop elongates and turns to lie at an angle α to the flow until in the steady state the restoring force due to the surface tension balances the shear

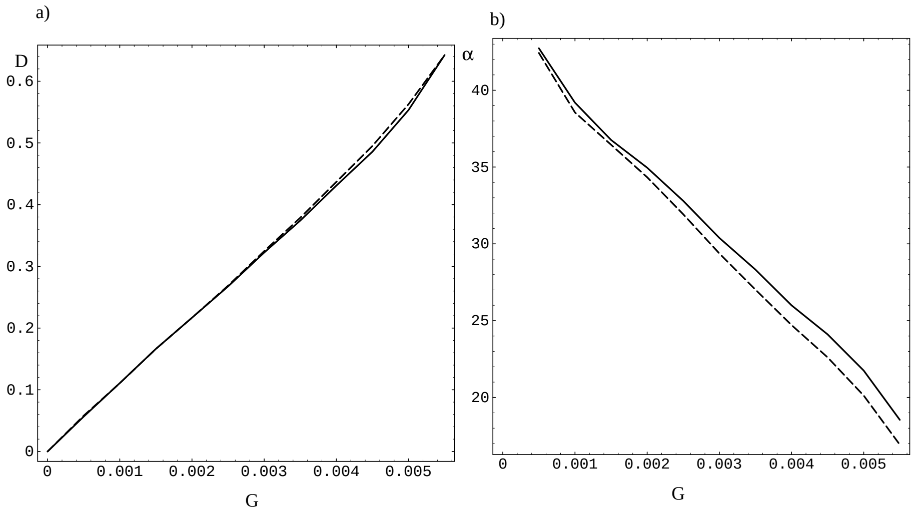

Figure 6.2: a) Deformation of a drop D and b) the tilting angle α for periodic (—) and forced (- - -) boundary conditions against the shear rate $\dot{\gamma} = G$. The undeformed drop has a radius of 8 lattice spacings and the lattice size is 60x30.

forces acting upon the drop. This situation is sketched in Figure 6.1. For small deformations the drop approximates well to an ellipse and its deformation can be defined as

$$D = \frac{A-B}{A+B} \tag{6.2}$$

where A and B are the major and minor axes, respectively. For drops of constant volume the deformation and inclination angle depend only on a dimensionless quantity, the capillary number[45]

$$\mathrm{Ca} = \frac{\nu a \dot{\gamma}}{\sigma} \tag{6.3}$$

where ν is the viscosity, a the undeformed drop radius and σ the surface tension. Throughout this chapter we take $\nu = 1/6$ and $\sigma = 0.046$ ($\kappa = 0.002$). This corresponds to an interface width ≈ 3 lattice spacings. The simulations are initialized with a circular domain with radius a of equilibrium concentration $\varphi = 1$ in a surrounding with $\varphi = -1$ with an interface width of about two lattice spacings. The other simulation parameters are $n = 2$, $T = 0.5$, $\lambda = 1.1$ and $\Gamma = 0.8$. Then the system is allowed to equilibrate for about 1000 time steps before data are recorded.

6.2 Break-up

Typical results for large drops ($V \gg V_d$) are shown in figure 6.2 where D and α are plotted as function of the shear rate. Results for forced and periodic boundary conditions are compared. The results presented are for a lattice of size 60x30 with a drop of initial radius of eight lattice spacings. They were obtained by equilibrating the fluid at each data point and then increasing the shear, re-equilibrating to give the next point and so on.

There is a linear dependence of the deformation on the shear rate for small shear rates, followed by a more rapid deformation as the shear increases, and finally break-up. The different boundary conditions lead only to small quantitative differences in the result. The results are in qualitative agreement with the results expected from comparison with three-dimensional experiments. For a drop of constant volume and given ratio of the viscosity of the drop and the surrounding fluid the deformation depends only on the capillary number [45]. The drops studied here do not have a constant volume and, therefore, deformation at break-up

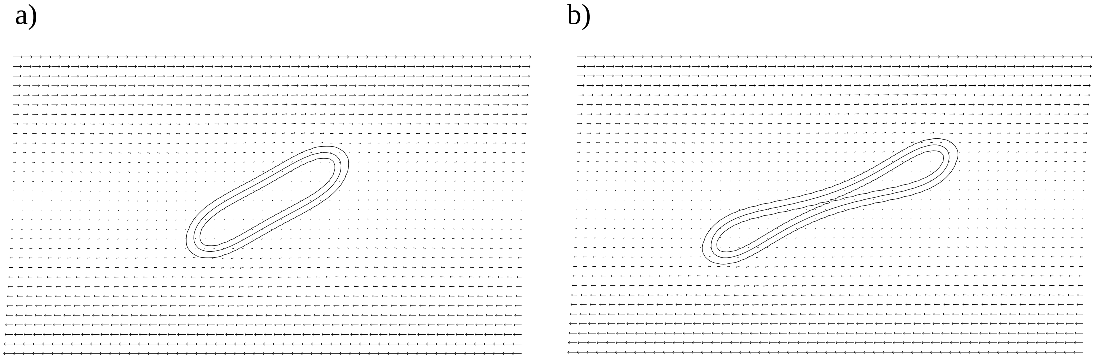

Figure 6.3: a) An equilibrium drop at $\dot{\gamma} = 0.002246$, b) the same drop at $\dot{\gamma} = 0.002251$ in the first stage of breaking up. The drop in b) breaks up into two drops of equal size at larger times. The arrows show the velocity at every third lattice point in each direction. The equilibrium values of φ are -1 and 1. The contour lines are drawn for $\varphi \in \{-0.9, 0, 0.9\}$

should depend on the parameters of the system, but it is reasonable to expect only a weak dependence. Indeed, we find $D_b \approx 0.65$ for drops with undeformed radii 8,13,20 in those cases where they break up.

It is known [56] that the second curvature is very important for the rupture of three-dimensional drops. This mechanism does not exist in two-dimensional systems. Therefore, we felt it was important to check the existence of the break-up carefully, particularly as it is well known [56] that a sudden change in shear strength can lead to rupture long before the critical shear rate. We performed careful numerical simulations where we saved a stationary solution and then increased the shear flow. If the drop ruptured instead of reaching a stationary state we loaded the old configuration and increased the shear rate by only half the previous amount. We iterated this step until the increase in shear rate was smaller than a lower bound. The shear rate never grew larger than a previously rejected

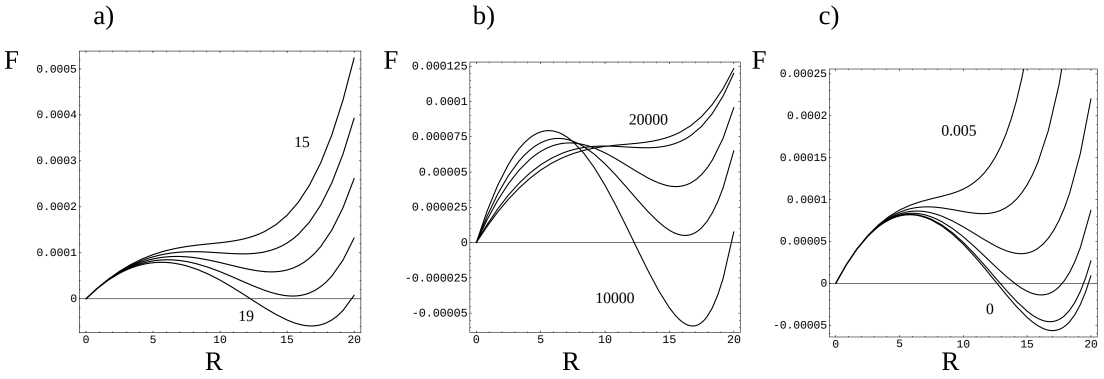

Figure 6.4: The free energy plotted as function of the drop radius for a) a lattice with 10000 points for concentrations that without surface effects would correspond to drops of radii R^0 =15,16,17,18 and 19; b) a system with $R^0 = 19$ and lattice sizes 10000, 12000, 14000, 16000, 18000 and 20000; c) a system of size 10000 and $R^0 = 19$ for shear rates $\dot{\gamma}$ =0, 0.001, 0.002, 0.003, 0.004 and 0.005.

shear rate showing that the break-up is not due to non-equilibrium effects. We then decreased the shear rate to check that the system is in equilibrium at every point. No hysteresis effects were observed, showing that this is indeed the case.

It should be pointed out, however, that the rupture mechanism is very different in two and three dimensions. Three-dimensional drops break up into two main drops and satellite drops [56]. We observe that two-dimensional drops break up into two drops of equal size as shown in Figure 6.3.

6.3 Dissolution

For given n_A, n_B, T, if a binary fluid lies in the coexistence region it will separate into two phases with, say, concentration differences φ_1 and φ_2. Each phase occupies a fraction of the total volume of the system which is determined by the densities and temperature. For a finite system the interface between the two phases results in a finite positive contribution to the free energy and, if this is too large relative to the gain in free energy due to the phase separation, the drop is unstable.

For the model simulated here it is possible to obtain an estimate of the droplet volume below which dissolution will occur. Ignoring the interface curvature the surface tension for an interface orthogonal to the z-direction is (2.44)

$$\sigma = \kappa \int_{-\infty}^{\infty} \left(\frac{\partial \varphi}{\partial z} \right)^2 . \tag{6.4}$$

Hence, using (2.33) the free energy of a drop of radius R in a volume V is

$$F = \pi R^2 \psi(\varphi_1, n, T) + (V - \pi R^2) \psi(\varphi_2, n, T) + 2\pi R \sigma. \tag{6.5}$$

This should be minimized with respect to R, φ_1 and φ_2 where one variable can be eliminated by the constraint

$$\pi R^2 \varphi_1 + (V - \pi R^2) \varphi_2 = \varphi. \tag{6.6}$$

In Figure 6.4a the free energy, relative to that of a homogeneous system, is plotted as a function of the drop radius for different concentrations of A and B particles. The concentrations are chosen such that without the surface effects drops of radii 15,16,17,18 and 19 would minimize the free energy on a lattice of size 100x100. We will denote these radii by R^0. Without the surface free energy term there is only one minimum and this will always be reached. With surface effects the homogeneous phase ($R = 0$) is always stable and a finite deviation from it is needed to reach the global minimum. This corresponds to the metastability of some regions of phase space where a finite nucleation barrier prevents immediate phase separation.

The lowest free energy curve in Figure 6.4a corresponds to $R^0 = 19$. The figure shows that the effect of the surface free energy is to shift the minimum from 19 to about 16.7. For smaller R^0 the minimum becomes a local minimum at $R^0 \approx 18$. In systems with fluctuations this will eventually lead to the drops dissolving. The lattice Boltzmann simulations reported here, however, do not include noise, and a drop in a local minimum will be stable. For concentration ratios that lead to a graph that has no local minimum ($R^0 \lesssim 15.5$) the drop will dissolve. We observe, though, that the initial dynamics are very slow.

The radius below which drops dissolve depends not only on the size of the drop but also on the total volume of the system. Results for the concentration corresponding to $R^0 = 19$ for different system sizes are shown in Figure 6.4b. Droplets are less stable in a larger system because more material from the drop is needed to change the concentration outside the drop.

When shear is applied the droplets deform. They have a larger interface so that the surface contributions are increased. For small shear rates the dependence of the deformation on the shear rate is approximately linear and we can use

$$D \approx 10\dot{\gamma}R \tag{6.7}$$

where R is the radius of the undeformed drop with the same volume. Approxi-

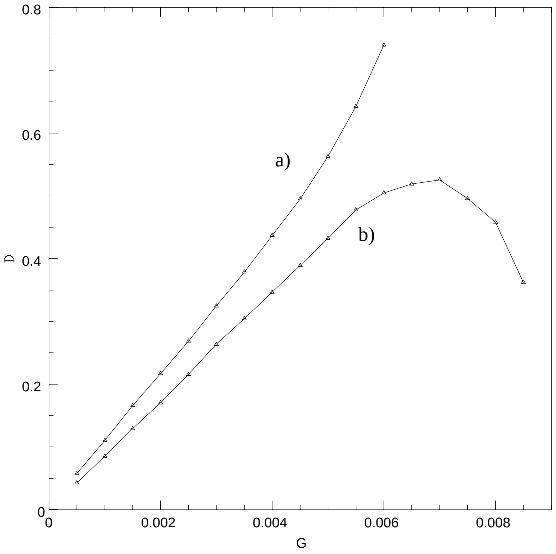

Figure 6.5: Deformation as function of shear rate for a drop of radius 8 for systems of size a) 60x30, b) 70x40. The drop in the smaller system breaks up while the drop in the larger system dissolves. Because the mass of the drop decreases strongly at high shear rates its deformation decreases under the increase of shear before it completely dissolves.

mating the shape of the deformed drop by an ellipse the length of the interface is given by

$$L = \sqrt{\frac{1-D}{1+D}} E\left(-\frac{4D}{(1-D)^2}\right) \tag{6.8}$$

where $E(k)$ denotes the complete elliptic integral of the second kind. This result can be used to estimate the effect of shear flow on the free energy. The results for $R^0 = 19$ for different shear rates are shown in Figure 6.4c. The minimum in the free energy vanishes for high shear rates and no stable drops can exist. This corresponds to the dissolution of a drop under shear.

The effects predicted by the thermodynamic theory are observed in the simulations. In Figure 6.5 results for the simulation of a drop of $R^0 = 8$ on lattices of size 60x30 and 70x40 are shown. For the smaller lattice $V_b < V_d$ and the drop breaks up. For the larger lattice the drop can exist to larger values of the shear, but loses mass. Finally, as the shear is increased further, it dissolves.

It is interesting to note that the theory predicts that every drop will dissolve under shear in a sufficiently large system. That is because the mass loss from the drop has to change the concentration outside the drop in order to reach a new equilibrium. This can, however, be very difficult to observe because there is a separation of time scales. The time t_D needed for diffusion to equilibrate the system scales as $t_D \sim L^2$ where L is the length of the system. This result is altered under shear [28] and in the limit of very large shear rates $t_D \sim L^{\frac{3}{2}}$. The time t_F for the system to reach a steady flow and a new deformation of the bubble scales as $t_F \sim L$. Therefore, in large systems the time for the deformation of the drop will be fast compared to the time for it to dissolve.

6.4 Discussion

In our previous discussion we have assumed that thermodynamic arguments for equilibrium can be carried over to the stationary states of dynamic systems. This is, however, not necessarily the case. We observe a deviation from this assumption in a phenomenon which we will call “tip-streaming”. Mass is pulled from the ends of the drop by the shear flow. The depletion of the concentration

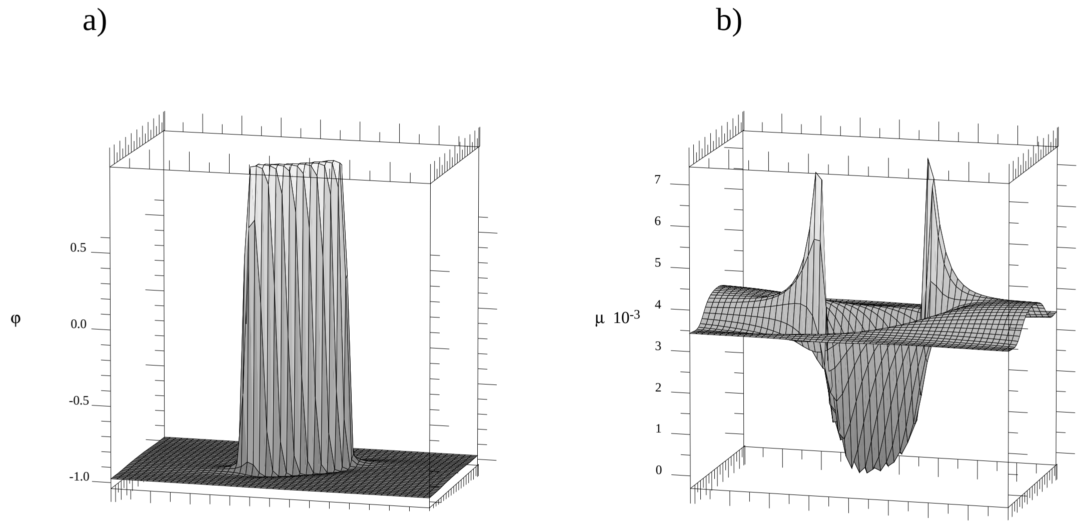

Figure 6.6: a) The density difference φ and b) the chemical potential μ for a highly deformed drop.

in the drop leads to a reduction of the chemical potential in the drop. The non-constant chemical potential leads to a diffusion current acting in the direction of the chemical potential gradient which returns material to the drop. Equilibrium is reached when the diffusion into the drop balances the tip streaming. The chemical potential in dynamic equilibrium is shown in Figure 6.6b. Note that this is a state of dynamic equilibrium, not thermodynamic equilibrium, as μ is not constant.

For a small diffusion constant a large chemical potential difference is needed for equilibrium and, hence, a large amount of mass is pulled from the drop.

This mechanism for the dissolving of a drop is distinct from the free energy driven mechanisms explained earlier in the chapter. It depends on the diffusion constant which is a dynamic quantity that does not enter the free energy. For infinite diffusion, however, material is immediately returned to the drop and no difference in the chemical potential is set up. A similar tip-streaming was observed in experiments, but was interpreted as a surfactant effect [56].

Halliday *et al.* performed simulations on a droplet in a binary fluid using a derivative of the the Gunstensen [19] algorithm. They obtain a similar break-up behavior but there are some important differences in the results. In particular in the simulations reported here all equilibrium drops are convex (see figure 6.3) whereas Halliday *et al.* [22] report stationary drops that are constricted in the middle. They also observe smaller inclination angles α at break up. The discrepancies warrant further investigation. Another feature not reported by Halliday *et al.* is the dissolution of drops under shear. This may be due the fact that they work in a region where the two components are more strongly separated. Nevertheless, small droplets should still dissolve. We caution that the time-scale for dissolution can be much larger than that for the deformation of the droplet to reach an equilibrium value.

Goldburg and Min [17] performed experiments on nucleation in a binary mixture in the presence of shear. They observed the vanishing of drops under the influence of shear as a sharp transition. This transition may be interpreted as corresponding to the point where $V_b = V_d$.

To conclude, in this chapter we have shown that drops under increasing shear flow can either break up or dissolve. We explained this behaviour with thermodynamic arguments. Tip-streaming was shown to lead to a state of dynamic equilibrium for deformed droplets.

Chapter 7

An H-Theorem for lattice Boltzmann

The only consistent microscopic derivation of an H-theorem has been given by Boltzmann for the famous Boltzmann equation (see [29]). An H-theorem states that a functional can be defined that is a strictly decreasing function in time. For the continuous Boltzmann equation this is the famous H-functional

$$H(t) = \int d\mathbf{x} \int d\mathbf{v} f(\mathbf{x}, \mathbf{v}) \ln(f(\mathbf{x}, \mathbf{v})). \tag{7.1}$$

Boltzmann was able to prove that for his equation

$$\frac{dH(t)}{dt} \leq 0. \tag{7.2}$$

This maps to the second law of thermodynamics which states that the entropy is a monotonic function in time. In an isothermal situation where energy is not conserved the H-functional no longer corresponds to the entropy but rather to the free energy, which has a monotonic time behaviour.

Because of the analogy between the continuum Boltzmann equation and the lattice Boltzmann equation it has been widely speculated that the discretized lattice Boltzmann equation might also obey an H-theorem, although no proof for such an H-theorem has been found. The only H-theorem which has been proved is a version for lattice gases which assumes semi-detailed balance [14]. In this chapter we analyse the general conditions under which a BGK lattice Boltzmann model can obey an H-theorem. We show that lattice Boltzmann schemes do not automatically obey an H-theorem. It is possible, however, to define lattice Boltzmann schemes that do obey an H-Theorem.

7.1 The lattice Boltzmann scheme

We will briefly review the BGK lattice Boltzmann scheme for a single component fluid for which we want to find an H-theorem. The evolution equation for the densities are, as before

$$f_i(\mathbf{x} + \mathbf{v}_i \Delta t, t + \Delta t) = f_i(\mathbf{x}, t) + \frac{\Delta t}{\tau} \left(f_i^0 - f_i(\mathbf{x}, t) \right). \tag{7.3}$$

The local density $n(\mathbf{x}, t)$, the local net velocity $\mathbf{u}(\mathbf{x}, t)$ and, for a thermal model, the local kinetic energy $\epsilon(\mathbf{x}, t)$ are given by:

$$n = \sum_{i=0}^{N} f_i, \quad n\mathbf{u} = \sum_{i=0}^{N} f_i \mathbf{v}_i, \quad n\epsilon = \sum_{i=0}^{N} f_i |\mathbf{v}_i|^2. \tag{7.4}$$

In order for this approach to simulate the continuity, Navier-Stokes and, for a thermal model, the heat equations the f_i^0 have to respect additional constraints, namely higher order moments have to correspond to the higher order moments of the continuum Boltzmann distribution.

7.2 The H-Theorem

Let us now consider whether or not this scheme can obey an H-Theorem. If we have a functional that always decreases in time, then locally the functional must be minimal if the distribution function is the equilibrium distribution.

A slightly more subtle point refers to the streaming step. Let us consider the collision-less limit ($\tau \to \infty$) where we have only streaming. In a periodic system it follows that the time evolution also has to be periodic for $N!$ steps if N is the number of lattice sites. Thus if this system obeys the H-theorem the streaming step cannot change the H functional.

A different way of seeing that the H-functional has to be invariant under the streaming step is to consider a system for which the H functional has the value H_1 and then perform a streaming step to a new system for which the H-functional has the value H_2. If the evolution obeys an H-Theorem, it follows that $H_1 \geq H_2$. We then invert all the velocities. It seems reasonable to assume that this operation should not change the value of the H-functional. If we now perform a streaming step on the new system we arrive at the original system with inverted velocities and we can conclude $H_2 \geq H_1$ and therefore $H_1 = H_2$.

In order for the H-functional to be invariant under the streaming operation there can be no cross-terms between the densities in the H functional. It can therefore be written as a sum of functions of the f_i separately

$$H[\{f_i\}](t) \quad = \quad \sum_{l=1}^{L}\sum_{i} h_i[\{f_i\}(\mathbf{x}_l, t)] \tag{7.5}$$

where L is the number of lattice points and l is an index that numbers all points of the lattice.

The equilibrium distribution f_i^0 is the distribution that minimizes the H-functional under the constraints that its moments have the same values for the conserved quantities of the distribution before the collision. We can eliminate these constraints by introducing Lagrange multipliers into the the H-functional. Then we minimize the functional and obtain an expression for the equilibrium function in terms of the Lagrange multipliers

$$H[\{f_i\}] \quad = \quad \sum_{i=0}^{N} h_i(f_i) + a\left(\sum_{i=0}^{N} f_i - n\right) + \mathbf{b}\left(\sum_{i=0}^{N} f_i\mathbf{v}_i - n\mathbf{u}\right) + c\left(\sum_{i=0}^{N} f_i|\mathbf{v}_i|^2 - n\epsilon\right) \tag{7.6}$$

$$\begin{aligned}
\Rightarrow 0 \quad &\overset{!}{=} \quad \delta H[\{f_i\}]\Big|_{\{f_i\}=\{f_i^0\}} \\
&= \quad \sum_{i=0}^{N} \delta f_i \underbrace{\left(h_i{}'(f_i) + a + \mathbf{b}\mathbf{v}_i + c\mathbf{v}_i^2\right)}_{=0 \text{ for } f_i = f_i^0}
\end{aligned}$$

$$\Rightarrow f_i^0 \quad = \quad h_i{}'^{-1}(-a - \mathbf{b}\mathbf{v}_i - c\mathbf{v}_i^2). \tag{7.7}$$

This gives a unique definition for f^0 if the h_i' are strictly monotonic, i.e., if h_i is convex. The Lagrangian multipliers are determined by the conservation constraints

$$n = \sum_{i=0}^{N} f_i^0, \quad n\mathbf{u} = \sum_{i=0}^{N} f_i^0\mathbf{v}_i, \quad n\epsilon = \sum_{i=0}^{N} f_i^0\mathbf{v}_i\mathbf{v}_i. \tag{7.8}$$

For systems without energy conservation we recover the same conditions with $c = 0$ in (7.6) and the energy conservation constraint does not apply.

7.2.1 Local H-Theorem

We can now show that in the collision term with the equilibrium function 7.7 the value of the H-functional decreases. We are only concerned with the collision term and, therefore, drop the $\mathbf{x}$ dependence. We then get for the time development of the H-functional

$$H[\{f_i\}](t+\Delta t) - H[\{f_i\}](t) \leq 0, \qquad \forall \frac{\tau}{\Delta t} > 1. \tag{7.9}$$

We now provide the proof for this statement in mathematical terms. It is technically difficult to prove the H-theorem for discrete time steps. We therefore introduce a continuation of the definition of the densities for continuous time. The continuation is chosen so that the densities obey the conservation constraints at all times. For these densities we can then prove an infinitesimal H-theorem over which we integrate to obtain the exact H-theorem for discrete time.

PROOF:

We define for real $s \in [0, \Delta t]$

$$f_i(t+s) = f_i(t) + \frac{s}{\tau}\left(f_i^0 - f_i(t)\right). \tag{7.10}$$

Observe that $f_i^0 = f_i^0(n, \mathbf{u}, \epsilon)$ is the equilibrium distribution for all $f_i(t+s)$ since the conserved quantities are the same for all $f_i(t+s)$. A useful relation is

$$f_i^0 - f_i(t) = \alpha(s)(f_i^0 - f_i(t+s)). \tag{7.11}$$

We see this by considering equation (7.10) from which we get

$$f_i(t) = \frac{f_i(t+s) - \frac{s}{\tau} f_i^0}{1 - \frac{s}{\tau}}. \tag{7.12}$$

Using this we see that

$$\begin{aligned}
f_i^0 - f_i(t) &= f_i^0 - \frac{f_i(t+s) - \frac{s}{\tau} f_i^0}{1 - \frac{s}{\tau}} \\
&= \frac{f_i^0 \left(1 - \frac{s}{\tau}\right) - f_i(t+s) + \frac{s}{\tau} f_i^0}{1 - \frac{s}{\tau}} \\
&= \frac{f_i^0 - f_i(t+s)}{1 - \frac{s}{\tau}}. \\
\Rightarrow \alpha(s) &= \left(1 - \frac{s}{\tau}\right)^{-1} \qquad (7.13)
\end{aligned}$$

and in particular $\alpha(s) > 0 \quad \forall s \in [0, \Delta t]$. This will turn out to be the reason why we can only prove the condition for $\tau > \Delta t$. Now we can prove the local H-theorem using the definition of H from (7.6):

$$\begin{aligned}
& H[\{f_i\}](t + \Delta t) - H[\{f_i\}](t) \\
= \quad & \int_0^{\Delta t} ds \sum_{i=0}^{N} \partial_{f_i}(h_i(f_i(t+s)) + a f_i(t+s) + \mathbf{b} f_i(t+s)\mathbf{v}_i + c f_i(t+s)\mathbf{v}_i^2 - \frac{1}{N}(an + \mathbf{b}n\mathbf{u} \\
\overset{(7.10)}{=} \quad & \int_0^{\Delta t} ds \sum_{i=0}^{N} \left(h_i{}'(f_i(t+s)) + a + \mathbf{b}\mathbf{v}_i + c\mathbf{v}_i^2\right) \times \frac{1}{\tau}\left(f_i^0 - f_i(t)\right) \\
\overset{(7.7,7.11)}{=} \quad & \int_0^{\Delta t} ds \sum_{i=0}^{N} \left(h_i{}'(f_i(t+s)) - h_i{}'(f_i^0)\right) \times \frac{\alpha(s)}{\tau}(f_i^0 - f_i(t+s)) \\
\leq \quad & 0 \quad \text{if } h \text{ is a convex function.}
\end{aligned}$$

7.2.2 Global H-Theorem

Since we required that H be invariant under the streaming step nothing remains to be done. The total entropy $H[\{f_i\}](t)$ defined as

$$H[\{f_i(\mathbf{x})\}](t) = \sum_{l=1}^{L} \sum_{i=0} h_i(f_i(\mathbf{x}_l, t)) \tag{7.15}$$

where L is the number of lattice points and l is an index that numbers all points of the lattice, only changes in the collision step. We therefore have the global H-theorem:

$$H[\{f_i(\mathbf{x})\}](t + \Delta t) - H[\{f_i(\mathbf{x})\}(t)], \leq 0 \qquad \forall \tau > 1. \tag{7.16}$$

7.3 The Global Equilibrium Distribution

In statistical mechanics the H-theorem is used to prove the existence of a unique equilibrium state of the system. It will turn out that for lattice systems this is not necessarily the case. Demanding the existence of a well-defined ground state gives us a constraint for the structure of the lattice. This is be equivalent to the constraint that there are no spuriously conserved quantities.

Since we have a global H-Theorem and the H-Functional is bounded we know that the scheme has to converge to some minimal value of the H-Functional. We will now examine what information we can extract from our H-Theorem about the final state.

Since, in the final state, the H-Functional does not change we know that it also cannot change locally in the collisions. It follows:

$$H[f_i](t+\Delta t) - H[f_i](t) = 0 \tag{7.17}$$

$$\overset{(7.14)}{\Rightarrow} \int_0^{\Delta t} ds \sum_{i=0}^{N} \left({h_i}'(f_i(t+s)) - {h_i}'(f_i^0) \right) \frac{\alpha(s)}{\tau} (f_i^0 - f_i(t+s)) = 0 \tag{7.18}$$

$$\overset{\text{All terms} \leq 0}{\Rightarrow} \left({h_i}'(f_i(t+s)) - {h_i}'(f_i^0) \right) \frac{\alpha(s)}{\tau} (f_i^0 - f_i(t+s)) = 0 \ (\forall i, \forall s) \tag{7.19}$$

$$\Rightarrow f_i(t) = f_i^0. \tag{7.20}$$

So in the final state all distributions have to be in local equilibrium. If all states are local equilibrium states then they do not change in the collision step. Therefore, we can conclude that for large t the system converges to a state that has local equilibrium distributions everywhere. The streaming step transforms one such state to another (or the same) such state.

Whether these conditions force the global equilibrium to be homogeneous depends on the lattice and the set of velocity vectors $\{\mathbf{v}_i\}$. This question is related to the problem of spurious invariants (see for instance [1] and references therein). Spurious invariants are conserved quantities that do not correspond to any physical quantities. In a four-velocity model on a square lattice for instance the total momentum of all even and odd lattice sites is separately conserved. If the global equilibrium is constrained to be homogeneous then there can be no spurious invariants. If, however, inhomogeneous final states are possible, then these state can be characterized by at least one spuriously conserved quantity.

7.4 A lattice Boltzmann scheme with H-theorem

If we use the classical choice for the H-functional

$$H(\{f_i\}) = \sum_l \sum_i f_i \ln(f_i) \tag{7.21}$$

for a thermal model, i.e., a model with mass, momentum and energy conservation, we get for the equilibrium equation a Maxwell-Boltzmann distribution

$$f_i^0 = N \exp\left(\frac{(\mathbf{v}_i - \mathbf{U})^2}{T}\right) \tag{7.22}$$

where N, $\mathbf{U}$ and T are the Lagrange multipliers. This scheme simulates the continuity, Navier Stokes and heat equation to an approximation that depends on the choice of lattice (because the higher order moments needed for the Chapman Enskog expansion do not necessarily coincide for the discrete and continuum case). Unfortunately, the Lagrange multipliers cannot be expressed analytically in terms of the conserved quantities, but have to be found by numerically solving the non-linear equation. For a regime where the Navier Stokes and heat equation are recovered the Lagrange multipliers are well approximated by $\mathbf{U} \sim \mathbf{u}$ and $T \sim \theta = 1/d(\epsilon - n\mathbf{u}^2)$ where d is the number of spatial dimensions.

The advantage of this scheme is that it is numerically stable for $\tau > \Delta t$. This is ensured by the H-Theorem, because numerical instabilities lead to inhomogeneities that would increase the H-functional.

7.5 Why our lattice Boltzmann scheme does not have an H-theorem

The usual BGK lattice Boltzmann schemes have a polynomial equilibrium distribution. For an isothermal model it takes the form

$$f_i^0 = A_\sigma + B_\sigma u_\alpha v_{i\alpha} + C_\sigma u_\alpha u_\alpha + D_\sigma u_\alpha u_\beta v_{i\alpha} v_{i\beta}, \tag{7.23}$$

where σ is an index distinguishing velocities with different magnitudes. If this equilibrium distribution is to be derived from an H-functional it has to take the form

$$\begin{aligned} f_i^0 &= {h_i'}^{-1}(a + b_\alpha v_{i\alpha}) \\ &= \alpha_\sigma + \beta_\sigma(a + b_\alpha v_{i\alpha}) + \gamma_\sigma(a + b_\alpha v_{i\alpha})^2 \\ &= (\alpha_\sigma + \beta_\sigma a + \gamma_\sigma a^2) + (\beta + 2\gamma_\sigma) b_\alpha v_{i\alpha} + \gamma_\sigma b_\alpha b_\beta v_{i\alpha} v_{i\beta} \end{aligned} \tag{7.24}$$

where the coefficients α_σ, β_σ and γ_σ are constants that cannot depend on n or $\mathbf{u}$. To calculate the Lagrange multipliers b_α we use the momentum conservation and get for a nine velocity model

$$\begin{aligned} n u_\alpha &= \sum_i f_i^0 v_{i\alpha} = (2\beta_1 + 4\beta_2 + 4\gamma_1 + 8\gamma_2) b_\alpha \\ \Rightarrow b_\alpha &= \frac{n u_\alpha}{2\beta_1 + 4\beta_2 + 4\gamma_1 + 8\gamma_2}. \end{aligned} \tag{7.25}$$

Therefore the coefficient of the $v_{i\alpha} v_{i\beta}$ term has a n^2 dependence for any scheme that obeys an H-theorem. Our scheme, however (as well as all other schemes of which we are aware), has a simple n dependence for all coefficients and, therefore can not obey an H-theorem.

7.6 Discussion

In this chapter we have been able to prove that it is possible to define a lattice Boltzmann scheme that minimizes an H-functional. Lattice Boltzmann schemes, however, do not obey an H-theorem automatically. The condition for a lattice Boltzmann scheme to obey and H-theorem is rather restrictive. We have been able to prove that for our lattice Boltzmann scheme, as well as for all other schemes of which we are aware, no functional exists that is a monotonic function of time.

We are still investigating the possibility of defining other schemes that both obey an H-theorem and fulfill the additional requirements needed to simulate the continuity and compressible Navier Stokes equations.

Appendix A

Recovery of the compressible Navier Stokes equations

It has not always been realized that lattice Boltzmann simulations can be derived in a way that recovers the full compressible Navier-Stokes equation [1, 58]. It turns out that the compressible Navier Stokes equations are recovered for the lattice Boltzmann method if a specific form of the third-velocity moment is chosen. This fact was first stated by Jörg Weimar [66]. We will derive the general set of equations for the free energy lattice Boltzmann method.

The derivation of the macroscopic equations from the lattice Boltzmann evolution equation 2.1 in Chapter 2 was completely equivalent to the derivation of hydrodynamics from the continuum Boltzmann equation (see, for instance, [29]). In kinetic theory the third moment is given by the condition that the heat flux for the equilibrium distribution vanishes. The discrete analog of this result is

$$\sum_i f_i^0 (v_{i\alpha} - u_\alpha)(v_{i\beta} - u_\beta)(v_{i\gamma} - u_\gamma) = 0. \tag{A.1}$$

For the continuum result $\sum_i$ is replaced by $\int dx$. The third moment is then given by

$$\sum_i f_i^0 v_{i\alpha} v_{i\beta} v_{i\gamma} = P_{\alpha\beta} u_\gamma + P_{\alpha\gamma} u_\beta + P_{\beta\gamma} u_\alpha + n u_\alpha u_\beta u_\gamma. \tag{A.2}$$

With this we can derive the usual viscosity terms for the Navier Stokes equation from both kinetic theory and Lattice Boltzmann alike. For the viscosity terms 2.28 we get:

$$\begin{aligned}
& \partial_t \sum_i f_i^0 v_{i\alpha} v_{i\beta} + \partial_\gamma \sum f_i^0 v_{i\alpha} v_{i\beta} v_{i\gamma} \\
= \; & \partial_t (P_{\alpha\beta} + n u_\alpha u_\beta) + \partial_\gamma (P_{\alpha\beta} u_\gamma + P_{\alpha\gamma} u_\beta + P_{\beta\gamma} u_\alpha + n u_\alpha u_\beta u_\gamma) + O(\partial^2) \\
= \; & \partial_n P_{\alpha\beta} \partial_t n + \partial_t (n u_\alpha) u_\beta + n u_\alpha \partial_t u_\beta \\
& + \partial_\gamma P_{\alpha\beta} u_\gamma + P_{\alpha\beta} \partial_\gamma u_\gamma + \partial_\gamma P_{\alpha\gamma} u_\beta + P_{\alpha\gamma} \partial_\gamma u_\beta + \partial_\gamma P_{\beta\gamma} u_\alpha + P_{\beta\gamma} \partial_\gamma u_\alpha \\
& + \partial_\gamma (n u_\alpha u_\beta u_\gamma) + O(\partial^2) \\
= \; & -\partial_n P_{\alpha\beta} \partial_\gamma (n u_\gamma) - \partial_\gamma (P_{\alpha\gamma} + n u_\alpha u_\gamma) u_\beta \underline{- n u_\alpha \frac{1}{n} \partial_\gamma P_{\beta\gamma}} - n u_\alpha u_\gamma \partial_\gamma u_\beta \\
& + \partial_n P_{\alpha\beta} (\partial_\gamma n) u_\gamma + P_{\alpha\beta} \partial_\gamma u_\gamma + \partial_\gamma P_{\alpha\gamma} u_\beta + P_{\alpha\gamma} \partial_\gamma u_\beta \underline{+ \partial_\gamma P_{\beta\gamma} u_\alpha} \\
& + P_{\beta\gamma} \partial_\gamma u_\alpha + \partial_\gamma (n u_\alpha u_\beta u_\gamma) + O(\partial^2) \\
= \; & -\partial_n P_{\alpha\beta} \partial_\gamma (n u_\gamma) \underline{- \partial_\gamma P_{\alpha\gamma} u_\beta} - \underline{\partial_\gamma (n u_\alpha u_\gamma) u_\beta} - \underline{n u_\alpha u_\gamma \partial_\gamma u_\beta} \\
& + \partial_n P_{\alpha\beta} (\partial_\gamma n) u_\gamma + P_{\alpha\beta} \partial_\gamma u_\gamma \underline{+ \partial_\gamma P_{\alpha\gamma} u_\beta} + P_{\alpha\gamma} \partial_\gamma u_\beta + \\
& P_{\beta\gamma} \partial_\gamma u_\alpha + \underline{\partial_\gamma (n u_\alpha u_\beta u_\gamma)} + O(\partial^2) \\
= \; & \underline{-\partial_n P_{\alpha\beta} (\partial_\gamma n) u_\gamma} - \partial_n P_{\alpha\beta} n \partial_\gamma u_\gamma + \underline{\partial_n P_{\alpha\beta} (\partial_\gamma n) u_\gamma}
\end{aligned}$$

$$
\begin{aligned}
&+P_{\alpha\beta}\partial_\gamma u_\gamma + P_{\alpha\gamma}\partial_\gamma u_\beta + P_{\beta\gamma}\partial_\gamma u_\alpha + O(\partial^2) \\
=\ & (P_{\alpha\beta} - n\partial_n P_{\alpha\beta})\partial_\gamma u_\gamma + P_{\alpha\gamma}\partial_\gamma u_\beta + P_{\beta\gamma}\partial_\gamma u_\alpha + O(\partial^2). \qquad \text{(A.3)}
\end{aligned}
$$

These are the viscosity terms for a general free energy lattice Boltzmann scheme with a third moment given by (A.2). In the continuum case of an ideal gas ($p_0 = nkT$) or equivalently to zero order in the derivatives (assuming that we are far from any interfaces) we have

$$P_{\alpha\beta} = p_0\delta_{\alpha\beta}. \qquad \text{(A.4)}$$

Then we find for the viscosity terms

$$(p_0 - n\partial_n p_0)\partial_\gamma u_\gamma + Dp_0\partial_\alpha u_\beta + Dp_0\partial_\beta u_\alpha, \qquad \text{(A.5)}$$

where D is the number of spatial dimensions. This is a standard compressible form of the viscosity terms in the Navier Stokes equation.

For a nine-velocity model, however, it is not possible to impose the condition A.2. This is because for a nine-velocity model

$$\sum_i f_i^0 v_{ix}v_{ix}v_{ix} = \sum_i f_i^0 v_{ix} = nu_x \neq 3P_{xx}u_x + nu_x^3 \qquad \text{(A.6)}$$

in general.

Appendix B

Derivation of the pressure tensor

In this appendix we show how the full pressure tensor (2.36) is derived. The pressure of a homogeneous system is defined as the volume derivative of the free energy. Writing the full volume dependence of the densities $n = N/V$ and $\varphi = (N_A - N_B)/V$ explicitly we see that:

$$P = -\partial_V \int_V \psi\left(\frac{N}{V}, \frac{N_A - N_B}{V}\right) = -\partial_V \left(V\psi\left(\frac{N}{V}, \frac{N_A - N_B}{V}\right)\right) = n\partial_n\psi + \varphi\partial_\varphi\psi - \psi. \tag{B.1}$$

For a non-homogeneous system the pressure is no longer a scalar but a tensor. The correct form of the pressure tensor can be derived from a Lagrangian expression for the free energy which is minimized in equilibrium:

$$L = \int_V \left(\psi(n,\varphi) + \frac{\kappa}{2}\partial_\alpha\varphi\partial_\alpha\varphi\right) + \mu_\varphi(\int_V \varphi - (N_A - N_B) + \mu_n(\int_V n - N). \tag{B.2}$$

To obtain differential equations for the equilibrium we evaluate the Euler-Lagrange equations and get

$$\begin{aligned} \mu_\varphi &= -\partial_\varphi \psi + \kappa \partial_\alpha \partial_\alpha \varphi, && \text{(B.3)} \\ \mu_n &= -\partial_n \psi. && \text{(B.4)} \end{aligned}$$

We multiply these equations with $\partial_\beta \varphi$ and $\partial_\beta n$, respectively, write it as a divergence and sum the equations. Remembering that μ_φ and μ_n are constants, this yields

$$\partial_\beta(\varphi \mu_\varphi + n\mu_n) = -\partial_\alpha(\psi \delta_{\alpha\beta} + \kappa(\partial_\alpha \varphi \partial_\beta \varphi - \frac{1}{2}\partial_\gamma \varphi \partial_\gamma \varphi \delta_{\alpha\beta})). \tag{B.5}$$

We then substitute the expressions for the chemical potential back into the equations and subtract the right-hand side from the left-hand side to derive a tensor σ that has a zero divergence:

$$\partial_\alpha \sigma_{\alpha\beta} = \partial_\alpha((\varphi \partial_\varphi \psi + n\partial_n \psi - \psi)\delta_{\alpha\beta} + \kappa(\partial_\alpha \varphi \partial_\beta \varphi - \frac{1}{2}\partial_\gamma \varphi \partial_\gamma \varphi \delta_{\alpha\beta} - \varphi \partial_\gamma \partial_\gamma \varphi \delta_{\alpha\beta})). \tag{B.6}$$

For a uniform system $\sigma_{\alpha\beta} = P\delta_{\alpha\beta}$ reduces to the homogeneous pressure. The divergence of the pressure tensor must vanish in equilibrium. We therefore identify $\sigma_{\alpha\beta}$ with the pressure tensor $P_{\alpha\beta}$.

Appendix C

Sketch of a lattice Boltzmann program

In this Appendix we present a sketch of a lattice Boltzmann program for a two dimensional nine velocity model. For numerical simplicity we decompose equations (2.1) and (2.2) into a streaming and a collision step. First the densities are initialized and then the streaming and collision step are performed. For the collision step the macroscopic variables need to be calculated so that the local equilibrium distributions can be determined.

```
#define NOVEC 9  /* Number of velocity vectors */
#define X 126   /* x-dimensions of the lattice */
#define Y 126   /* y-dimensions of the lattice */
/* definition of the velocity vectors */
int    iv[NOVEC][2]={{0,0},{1,0},{0,1},{-1,0},{0,-1},
     {1,1},{-1,1},{-1,-1},{1,-1}}
/* definition of the relaxation times */
double TAU_f=1,TAU_g=1;
/* definition of the fields for the simulation */
double f[X][Y][NOVEC],fc[X][Y][NOVEC],
```

```
       g[X][Y][NOVEC],gc[X][Y][NOVEC], /* two copies of f_i and g_i */
       n[X][Y],        /* total density */
       phi[X][Y],      /* density difference*/
       dphi[X][Y][2],  /* gradient of density difference */
       ddphi[X][Y],    /* Laplacian of density difference */
       u[X][Y][2];     /* velocity vectors */
main()
{
  int i;
  initialize();
  for (i=0;i<ITERATIONS; i++){
    streaming();
    collision();
    /* Here one should also do something with the simulation data */
  }
}
/* The streaming moves the fc_i densities along the velocity vectors v_i
   onto the f_i, and similarly the gc_i onto the g_i. Special care
   must be taken to incorporate the appropriate boundary conditions at
   the edges of the lattice. */
void streaming()
{
  int x,y,i;

  for (x=0; x<X; x++)
    for (y=0; y<Y; y++)
      for (i=0; i<NOVEC; i++)
{
  f[x][y][i]=fc[x-iv[i][0]][y-iv[i][1]][i];
  g[x][y][i]=gc[x-iv[i][0]][y-iv[i][1]][i];
}
}
/* The collision step performs the effects of the collision from the
   f_i onto the fc_i and the g_i on the gc_i.  */
void collision()
{
  double feq[NOVEC],geq[NOVEC];
  int x,y,j;

  calc_properties(f,g);
  for (x=0;x<X;x++)
  for (y=0;y<Y;y++)
    {
      calc_fg_eq(feq,geq,n[x][y],g[x][y],dg[x][y],ddg[x][y],u[x][y]);
      for (j=0;j<NOVEC;j++)
{
```

```
  fc[x][y][j] = f[x][y][j] +1.0/TAU_f*(feq[j]-f[x][y][j]);
  gc[x][y][j]=  g[x][y][j] +1.0/TAU_g*(geq[j]-g[x][y][j]);
}
    }
}

void calc_properties(double fc[X][Y][NOVEC], double gc[X][Y][NOVEC])
{
  int x,y,j;

  for (x=0;x<X;x++)
  for (y=0;y<Y;y++)
    {
      n[x][y]=g[x][y]=u[x][y][0]=u[x][y][1]=0;
      for (j=0; j<NOVEC; j++)
{
  n[x][y] += fc[x][y][j];
  g[x][y] += gc[x][y][j];
  u[x][y][0] += fc[x][y][j]*ev[j][0];
  u[x][y][1] += fc[x][y][j]*ev[j][1];
}
      u[x][y][0]/= n[i];
      u[x][y][1]/= n[i];
    }

    for (x=0; x<X; x++)
      for (y=0; y<Y; y++)
{
/* Special care must be taken here to incorporate the appropriate
   boundary conditions at the edges of the lattice*/
  dg[x][y][0]=(g[x+1][y]-g[x-1][y])/2/dx;
  dg[x][y][1]=(g[x][y+1]-g[x][y-1])/2/dx;
  ddg[x][y]=(g[x+1][y]-2*g[x][y]+g[x-1][y])/dx/dx+
            (g[x][y+1]-2*g[x][y]+g[x][y-1])/dx/dx;
}
}

void calc_fg_eq(double feq[NOVEC],double geq[NOVEC],double n, double g,
       double dg[2],double ddg, double u[2])
{
  double A0,A1,A2,B1,B2,C0,C1,C2,D1,D2,G1[2][2],G2[2][2];
  double H0,H1,H2,J0,J1,J2,K1,K2,Q1,Q2;
  int i;

\* this routine calculates the equilibrium distributions according to
   the  (2.54)-(2.65).   *\
}

void initialize()
```

```
{
  int x,y,j;
  double g,n,u[2],dg[2],ddg;
  double feq[NOVEC],geq[NOVEC];

  for (x=0;x,X;x++)
    for (y=0; y<Y; y++)
      {
/* Introduce some initial macroscopic fields as starting condition.
   Could be a random distribution, a drop, a stripe with an arbitrary
   flow field. */
        n    =....
u[0] =....
u[1] =....
g    =....
dg[0]=....
dg[1]=....
        ddg  =....
calc_fg_eq(feq,geq,n,g,dg,ddg,u);
for (j=0;j<NOVEC;j++){
          fc[x][y][j]=feq[j];
  gc[x][y][j]=geq[j];
      }
}
```

. . .

Bibliography

[1] R. Benzi, S. Succi and M. Vergassola, *The lattice Boltzmann equation: theory and application*, Physics Reports **222**, 145 (1992)

[2] P. Bhatnagar, E.P. Gross and M.K. Krook, , Phys. Rev. **94**, 511 (1954)

[3] K. Binder, *Theory of 1st-order phase transitions*, Rep. Prog. Phys. **50**, 783 (1987)

[4] A.J. Bray, *Theory of phase-ordering kinetics*, Adv. Phys. **43**, 357 (1994)

[5] J.D. Buckmaster and J.E. Flaherty, *The bursting of two-dimensional drops in slow viscous flow*, J. Fluid Mech. **60**, 625 (1973)

[6] C.K. Chan, F. Perrot and D. Beysens, *Effects of Hydrodynamics on Growth: Spinodal Decomposition under Uniform Shear Flow*, Phys. Rev. Lett. **61**, 412 (1998)

[7] S. Chen and G.D. Doolen, *Lattice Boltzmann Method for Fluid Flows*, Submitted to An. Rev. Fluid Mech. , (1997)

[8] P.V. Coveny and K.E. Novik, *Computer-simulations of domain growth and phase-separation in 2-dimensional binary immiscible fluids using dissipative particle dynamics*, Phys. Rev. E **54**, 5134 (1996)

[9] P.V. Coveny, *private communication.*

[10] M. Criado-Sancho, J. Casas-Vázquez and D. Jou, *Hydrodynamic fluctuations, nonequilibrium equations of state, and the shift of the spinodal line in polymer solutions under flow*, Phys. Rev. E **56**, 1887 (1997)

[11] J.K.J. Dhont, *Effects of Shear Flow on Long Ranged Correlations, on Spinodal Decomposition Kinetics and on the Location of the Critical Point and Cloud Point*, Physica Scripta **T55**, 127 (1994)

[12] E.G. Flekkøy, *Lattice Bhatnagar-Gross-Krook models for miscible fluids*, Phys. Rev. E **47**, 4247 (1993)

[13] U. Frisch, B. Hasslacher and Y. Pomeau, *Lattice-gas automata for the Navier-Stokes equations*, Phys. Rev. Lett. **56**, 1505 (1986)

[14] U. Frisch, D. d'Humières, B. Hasslacher, P. Lallemand, Y. Pomeau and J.P. Rivet, *Lattice Gas Hydrodynamics in Two and Three Dimensions*, Complex Systems **1**, 649 (1987)

[15] Amalie Frischknecht, cond-mat/970703 (18. Jul. 1997).

[16] H. Furukawa, *Role of inertia in the late stage of the phase separation of a fluid*, Physica A **204**, 237 (1994)

[17] W.I. Goldburg and K.Y. Min, *Nucleation in the presence of shear*, Physica A **204**, 246 (1994)

[18] J.D. Gunton, M.San Miguel and P. S. Sahni, in *1983*, Phase Transitions and Critical Phenomena **8**, 267 (Academic Press, New York)

[19] A.K. Gunstensen, D.H. Rothmann, S. Zaleski and G. Zanetti, *Lattice Boltzmann model of immiscible fluids*, Phys. Rev. A **43**, 4327 (1991)

[20] C.K. Haas and J.M. Torkelson, *Two-dimensional coarsening and phase separation in thin polymer solution films*, Phys. Rev. E **55**, 3191 (1997)

[21] I. Halliday and C.M. Care, *Steady state hydrodynamics of a lattice Boltzmann immiscible lattice gas*, Phys. Rev. E **53**, 1602 (1996)

[22] I. Halliday, C.M. Care, S. Thompson and D. White, *Induced Burst of Fluid Drops in a Two-Component Lattice BGK Fluid*, Phys. Rev. E **54**, 2573 (1996)

[23] T. Hashimoto, K. Matsuzaka, E. Moses and A. Onuki, *String Phase in Phase-Separating Fluids under Shear Flow*, Phys. Rev. Lett. **74**, 126 (1995)

[24] F.J. Higuera and S. Succi, *Simulating the flow around a circular-cylinder with a lattice Boltzmann-equation*, Euro. Phys. Lett. **8**, 517 (1989)

[25] F.J. Higuera, S. Succi and R. Benzi, *Lattice gas-dynamics with enhanced collisions*, Euro. Phys. Lett. **9**, 345 (1989)

[26] F.J. Higuera and J. Jiménez, *Boltzmann approach to lattice gas simulations*, Euro. Phys. Lett. **9**, 663 (1989)

[27] P.C. Hohenberg and B.I. Halperin, *Theory of dynamic critical phenomena*, Rev. Mod. Phys. **49**, 435 (1977)

[28] M.J. Howard and G.T. Barkama, *Shear Flows and Segregation in the reaction* $A + B \leftarrow 0$, Phys. Rev. E **53**, 5349 (1996)

[29] K. Huang, "Statistical Mechanics", second edition (1987), John Wiley & sons, New York · Chichester · Brisbane · Toronto · Singapore

[30] D. Jasnov and J. Vinals, *Coars-grained description of thermo-capillary flow*, J. Fluids **8**, 660 (1996)

[31] L.D. Landau and E.M.Lifshitz, "Fluid Mechanics",2nd edition, Pergamon Press, Oxford · New York · Seoul · Tokyo (1984)

[32] J. Läuger, C. Laubner and W. Gronski *Correlation between Shear Viscosity and Anisotropic Domain Growth during Spinodal Decomposition under Shear Flow*, Phys. Rev. Lett. **75**, 3576 (1995)

[33] A.W. Lees and S.F. Edwards, *The computer study of transport processes under extreme conditions*, J. Phys. C **5**, 1921 (1972)

[34] I.M. Lifshitz and V.V. Slyozov, J. Phys. Chem. Solids **19**, 35 (1961)

[35] T. Lookman, Y. Wu, F.J. Alexander and S. Chen, *Spinodal decomposition in fluids: Diffusive, viscous, and inertial regimes*, Phys. Rev. E **53**, 5513 (1996)

[36] G.R. McNamara and G. Zanetti, *Use of the Boltzmann-equation to simulate lattice-gas automata*, Phys. Rev. Lett. **61**, 2332 (1988)

[37] K.R. Menke and V. Sofonea, *Morphology of spinodal decomposition*, Phys. Rev. E **56**, 3761 (1997)

[38] J.F. Olson and D.H. Rothman, *Three-Dimensional Immiscible Lattice Gas: Application to Sheared Phase Separation*, J. Stat. Phys. **81**, 199 (1995)

[39] A. Onuki, *Phase transitions of fluids in shear flow*, J. Phys. C **9**, 6119 (1997)

[40] E. Orlandini, *private communication*

[41] E. Orlandini, M.R. Swift and J.M. Yeomans, *A lattice Boltzmann model of binary-fluid mixtures*, Euro. Phys. Lett. **32**, 463 (1995)

[42] W.R. Osborn, E. Orlandini, M.R. Swift, J.M. Yeomans and J.R. Banavar, *Lattice Boltzmann study of hydrodynamic spinodal decomposition*, Phys. Rev. Lett. **75**, 4031 (1995)

[43] T. Ohta, H. Nozaki and M. Doi, *Computer simulations of domain growth under shear flow*, Phys. Lett. A **145**, 304 (1990)

[44] Y.H. Qian, D. d'Humiéres and P. Lallemand, *Lattice BGK models for Navier-Stokes equation*, Euro. Phys. Lett. **17**, 479 (1992)

[45] J.M. Rallison, *The deformation of small viscous drops and bubbles in shear flows*, Ann. Rev. Fluid Mech. **16**, 45 (1984)

[46] J.M. Rallison, *A numerical study of the deformation and burst of a viscous drop in general shear flows*, J. Fluid Mech. **109**, 465 (1981)

[47] L.E. Reichel, *A modern course in statistical Physics*, Edward Arnold, London (1980)

[48] S. Richardson, *Two-dimensional bubbles in slow viscous flow*, J. Fluid Mech. **33**, 476 (1968)

[49] C. Roland and M. Granf, *Monte Carlo renormalization-group study of spinodal decomposition: Scaling and growth*, Phys. Rev. B **39**, 11971 (1989)

[50] D.H. Rothman and J.M. Keller, *Immiscible cellular-automaton fluids*, J. Stat. Phys. **52**, 1119 (1988)

[51] D.H. Rothman, *Complex Rheology in a Model of a Phase-Separating fluid*, Euro. Phys. Lett. **14**, 337 (1991)

[52] D.H. Rothman and S. Zaleski, *Lattice-gas cellular automata: Simple models of complex hydrodynamics*, to be published , (1997)

[53] J.S. Rowlinson and B. Widom, *Molecular theory of capillarity*, Clarendon Press, Oxford (1982)

[54] A. Shinozaki and Y. Oono, *Spinodal decomposition in 3-space*, Phys. Rev. E **48**, 2622 (1993)

[55] E.D. Siggia, *Late stages of spinodal decomposition under shear*, Phys. Rev. A **20**, 595 (1979)

[56] H.A. Stone, *Dynamics of drop Deformation and Breakup in Viscous Fluids*, Ann. Rev. Fluid Mech. **26**, 65 (1994)

[57] M.R. Swift, W.R. Osborn and J.M. Yeomans, *Lattice Boltzmann simulations of nonideal fluids*, Phys. Rev. Lett. **75**, 830 (1995)

[58] M.R. Swift, S.E. Orlandini, W.R. Osborn and J.M. Yeomans, *Lattice Boltzmann simulations of liquid-gas and binary-fluid systems*, Phys. Rev. E **54**, 5041 (1996)

[59] M.R. Swift, E. Orlandini, W.R. Osborn and J.M. Yeomans, *Lattice Boltzmann Simulations of Liquid-Gas and Binary-Fluid Systems*, Phys. Rev. E **54**, 5041 (1996)

[60] H. Tanaka, *Hydrodynamic interface quench effects on spinodal decomposition for symmetric binary fluid mixtures*, Phys. Rev. E **51**, 1313 (1995)

[61] H. Tanaka and T. Akira, *Spontaneous double phase separation induced by rapid hydrodynamic coarsening in two-dimensional fluid mixtures*, preprint.

[62] G.I. Taylor, *The formation of Emulsions in Definable Fields of Flow*, Proc. Roy. Soc. **26**, 501 (1934)

[63] *Effect of shear on Droplets in a Binary Mixture*, J. Mod. Phys. C **8**, 773 (1997)

[64] *Breakdown of scale-invariance in the coarsening of phase-separating binary fluids*, to be published

[65] C. Wagner, Z. Electrochem. **65**, 581 (19961)

[66] J. R. Weimar, *Cellular Automata for Reactive Systems*, Université Libre de Bruxelles, Faculté des Sciences, Service de Chimie Physique, Dissertation presented as part of the requirements for the degree of Docteur en Sciences (1995)

[67] Y. Wu, F.J. Alexander, T. Lookman and S. Chen, *Effects of Hydrodynamics on Phase Transition Kinetics in Two-Dimensional Binary Fluids*, Phys. Rev. Lett. **74**, 3852 (1995)